ABSTRACT

Title of Document:	Interfacing Microfluidic Bioanalysis with High Sensitivity Mass Spectrometry
	Chia-Wen Tsao, Ph.D, 2008
Directed By:	Professor Don L. DeVoe, Department of Mechanical Engineering

Mass spectrometry (MS) provides quantified information to identify unknown atom and molecules which has become a widely used analytical technique in bioanalysis field. Polymer-based microfluidics device provides benefits of low fabrication cost, fast analysis time and less sample consumption for biological sample process and separation prior to MS analysis. In this dissertation, a table-size, computer-controlled robotic spotting system was developed to couple polymer microfluidics with mass spectrometry as an automatic and high throughput interfacing method. To accomplish this goal, three major subjects, polymer microfabrication, high sensitivity MS target substrate and polymer microfluidics / mass spectrometry interfacing were further evaluated and developed.

First, polymer microfabrication techniques such as hot embossing and polymer bonding were discussed. Among those, a novel bonding technique of using UV/Ozone surface treatments for achieving low temperature bonds between poly(methyl methacrylte) (PMMA) and cyclic olefin copolymer (COC) microfluidic

substrates is demonstrated. Second, a novel high sensitivity silicon-based matrix-free LDI-MS target substrate, nanofilament silicon (nSi) surfaces, was demonstrated in this dissertation. With electrowetting on nSi surfaces, it is demonstrated as a novel approach for preparing nSi based LDI-MS targets for the analysis of complex peptide samples. Finally, off-line integration of multiplexed polymer microfluidic interfacing with mass spectrometry by direct and automated spotting of peptide sample from multiplexed polymer microfluidic chip is demonstrated as a simple and robust method with uniform spotting volume and MS signal. This automatic contact spotting system is further demonstrated coupling with on-chip peptide reverse phase liquid chromatography (RPLC) separation with nSi surface as a novel microfluidics/ off-line mass spectrometry analysis.

INTERFACING MICROFLUIDIC BIOANALYSIS
WITH HIGH SENSITIVITY MASS SPECTROMETRY

By

Chia-Wen Tsao

Dissertation submitted to the Faculty of the Graduate School of the
University of Maryland, College Park, in partial fulfillment
of the requirements for the degree of
Doctor of Philosophy
2008

Advisory Committee:
Associate Professor Don L. DeVoe, Chair
Professor Gary W. Rubloff
Professor Balakumar Balachandran
Assistant Professor Adam Hsieh
Assistant Professor Bao Yang

Dedication

To my beautiful wife, Yuan-Chun Chu, moved from Taiwan staying with me, supporting me and sharing all of my sorrow and happiness.

To my parents and grandparents raise me and love me in every endeavor.

To Huangs family, my brother in law, Po-Chun Huang, my sister, Chia-Ning Tsao, my lovely niece, Elaine Huang and my soon to be born nephew give me joy and all kinds of support.

Acknowledgements

First, I would like to give my deepest appreciation to my academic and research advisor, Dr. Don L. DeVoe, provides research guidelines and financial support for these years.

Many thanks to my friends as well as my coworkers at Maryland Microfluidic Lab (MML), Lou Hromada, Parshant Kumar, Likun Chu, Wei-Jen Cheng, Yi Zhou, Jikun Liu, Steve Chen, Jack Yang, Chen-Fei Kung and Chenren Shao.

Finally, I would like to thank to Tom Loughran and Jonathan Hummel at Nanocenter, Noel Whittaker and Yue Li at Mass Spectrometry Lab, Dr. Bill Vanderlinde, Russell Frizzell and Laurence Olver at Maryland LPS, Tim Maugel at Laboratory for Biological Ultrastructure, Tao Song at Calibrant Biosystem Inc. and Dr.Tim Cornish at John Hopkins APL.

Table of Contents

List of Tables

List of Figures

List of Nomenclature

2D PAGE = two-dimensional polyacrylamide gel electrophoresis
μTAS = micro total analysis systems
ACN = acetonitrile
BMA = butyl methacrylate
BOE = buffered oxide etchant
BP = benzophenone
BSA = bovine serum albumin
BuMA = butyl methacrylate
CE = capillary electrophoresis
CGE = capillary gel electrophoresis
CHCA = α-cyano-4-hydroxycinnamic acid
COC = cyclic olefin copolymer
CTE = coefficient of thermal expansion
CV = coefficient of variation
DIOS = desorption/ ionization on silicon
DIOS-MS = desorption/ ionization on silicon mass spectrometry
DMPA = 2,2'-dimethoxy-2-phenylacetophenone
DRIE = deep reactive ion etching
DTT = DL-dithiothreitol
EDA = ethylene diacrylate
EDMA = ethylene dimethacrylate
EGDMA = ethylene glycol dimethacrylate
EOF = electroosmotic flow
ESI = electrospray ionization
ESI-MS = electrospray ionization mass spectrometry
EtOH = ethyl alcohol
FITC = fluorescein isothiocyanate isomer I
FT = fourier transform
GC = gas chromatography
HF = hydrogen fluoride
HMX = octahydro-1,3,5,7-tetranitro-1,3,5,7-tetrazocine
H_2O_2 = hydrogen peroxide
HOME-HF = H_2O_2 metal-HF
HPLC = high performance liquid chromatography
IEF = isoelectric focusing
KOH = potassium hydroxide
LC = liquid chromatography
LDI = laser desorption/ionization
LDI-MS = laser desorption/ionization mass spectrometry
LOCP = lab-on-a-chip
MALDI = matrix-assist laser desorption/ionization
MALDI-MS = matrix-assist laser desorption/ionization mass spectrometry

MEMS = micro-electrical mechanical system
MS = mass spectrometry
m/z = mass-to-charge ratio
nSi = nanofilament silicon
PA = polyamide
PC = polycarbonate
PCR = polymerase chain reaction
PDMS = poly(dimethysiloxane)
PE = polyethylene
PETN = pentaerythritol tetranitrate
PFPPDMCS = (pentafluorophenyl)propyldimethylchlorosilane
PMMA = poly(methyl methacrylte)
PS = polystyrene
pSi = porous silicon
PVA = polyvinyl alcohol
QIT = quadrupole ion-trap
RDX = trinitrohexahydro-1,3,5-triazine
RhB = rhodamine B
RIE = reactive ion etching
RPLC = reverse phase liquid chromatography
SCX = strong cation exchange
SEC = size exclusion chromatography
S/N = signal-to-noise ratio
TB = tris-borate
TFA = trifluoroacetic acid
TMPTMA = trimethylolpropane trimethacrylate
TNT = 2,4,6-trinitrotoluene
TOF = time-of-flight
UV = ultraviolet
UVO = ultraviolet / ozone
XPS = X-ray photoelectron spectroscopy

Chapter 1 Introduction

In recent years, proteomics draw lots of research scientists' attention because it provides better understanding of cellular mechanisms than genomics. However, protein identification presents unique analytical challenges for its huge dynamic range. Besides, there is no protein amplification technology exists like polymerase chain reaction (PCR) for DNA analysis. So protein analysis is a more challenge task and detection sensitivity is critical. Mass spectrometry (MS) offers unique advantages of high molecular specificity, detection sensitivity and dynamic range which has become a widely used analytical technique for the characterization of proteins and biomolecules. However, the major drawback of mass spectrometry is its limitation in handling a complex mixture of compounds. Protein separation, on the other hand, can simplify complex protein mixtures by resolving them into small groups or individual proteins for consequent mass spectrometry analysis to identify the protein more accurately. Thus, combining analytical bioseparation technologies such as two-dimensional polyacrylamide gel electrophoresis (2D PAGE), high performance liquid chromatography (HPLC), capillary electrophoresis (CE), isoelectric focusing (IEF) and affinity chromatography with mass spectrometry provide benefits for protein analysis. For biological analysis application, coupling of microfluidics separation techniques with mass spectrometry is the most attractive approach to meet the challenge of increasing sample complexities and small sample volumes and it can benefit mutually with following advantages:

- The capabilities of both techniques are combined, with the result that both instruments can be operated at lower than their optimal performance

- The molecular specificity of the analysis is further optimized because the analyte is identified by chromatographic retention time as well as by the structure specific mass spectrometry data

- Mixture of varying complexities can be analyzed

- The sensitivity of analysis is improved because the sample enters the mass spectrometer in the form of a narrow focused band

- Less sample is required compared to an off-line analysis by two techniques

- The mutual signal suppression in the mass spectrometry analysis is minimized and the quality of mass spectral data is improved

Conventional protein analysis methods using fused silica capillaries or 2D PAGE are usually laborious, high cost and time consuming. As result, there is a trend to use microfluidics chip technique to address those challenges. Microfluidic chip devices commonly associated with the terms of "Lab-on-a-Chip (LOCP)" and "Micro Total Analysis Systems (µTAS)" was first proposed by Dr.Andreas Manz [1] in late 80's and it draws tremendously interest over the past decade due to its advantage of minimize the sample and reagent consumption, reduce analysis time and labor to achieve high throughput analysis. Various applications have been demonstrated including on chip sample purification, digestion, preconcentration, separation and interfacing with mass spectrometry [2-4].

Compare to fabrication of microfluidic system on silicon or glass substrate using microelectronic fabrication techniques in early stage. Advanced polymer microfluidic systems have gain more and more interests in lab-on-a-chip (LOCP) applications in recent years due to its good optical quality, good chemical resistance and low material cost. Besides, polymer-based microfabrication is relatively simpler and cheaper than silicon-based microfabrication. Polymer microfluidics chip can be replicate using mass production techniques such as injection molding and hot embossing which is cost effective and brings lots of benefits for commercial manufacturer to use polymer substrate for mass production of disposable microfluidic system.

1.1 Mass Spectrometry Interfacing

Implementation of novel mass spectrometry detection represents an attractive approach alternative to conventional optical detection. However, microfluidic chip to mass spectrometry interfacing technique is not a straightforward process and it needs to be further developed for effective sample transportation from the chip to mass spectrometer. A number of microfluidic deices have demonstrated interfacing with mass spectrometry. Generally, microfluidic device can be interfaced with mass spectrometry by two main categories: through electrospray ionization mass spectrometry (ESI-MS) and through matrix-assisted laser desorption/ionization mass spectrometry (MALDI-MS).

Electrospray ionization (ESI) can be generated directly from microfluidic chip surface, from inserted capillary or from machined tip. Among all, electrospray directly from chip surface is the most straightforward and most frequent approach for

interfacing microfluidic with mass spectrometry. Xu et al [5] and Ramsey et al [6] have demonstrated of the first mass spectrometry interfacing through electrospray ionization in 1997 by electrospray sample from the flat edge of a glass microfluidic chip as shown in Figure 1.1. However, several issues limit its application, for example: sample spreading at the hydrophilic interface causes large dead-volumes on the flat edge and flat edge is not ideal to establish strong electrical field thus doesn't create efficient and stable electrospray. In addition, the multiplexed ESI-MS is complete from channel to channel sequentially instead of simultaneously which limit the analysis throughput.
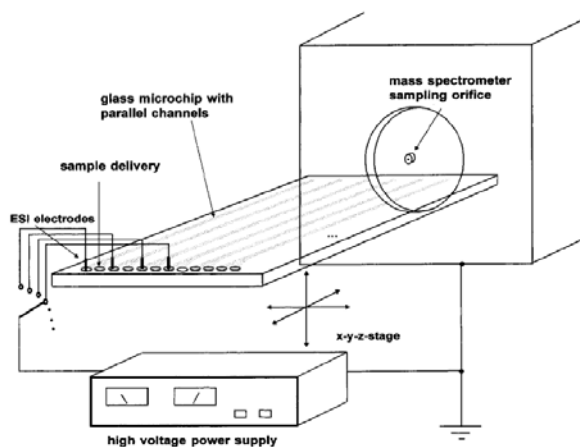
Figure 1.1: First on-line ESI-MS microfluidic chip report by Xu et al[5]

Following developments of ESI-MS interfacing involving in mating microchannels to conventional capillary tips [7-10], incorporating with hydrophobic membrane [11] and microfabricated, tapered electrospray tips [12-14] have present as potential solutions to minimized liquid spreading at channel orifice, minimized dead volumes and provide better stability and mass spectra accuracy. Matrix Assisted Laser Desorption/Ionization (MALDI) is an alternative mass spectrometry interfacing

method been widely used. MALDI-MS typically performed by direct pipetting or spotting sample and matrix solution onto the target sample followed by air-drying or vacuum drying of the deposited spot. The sensitivity of MALDI-MS can be down to fmol or even less by modify the target substrate. In addition, MALDI-MS interfacing is more capable of integrating with various approaches than on-line only ESI-MS interfacing technique. Examples of MADLI-MS interfacing including employee a rotating ball to on-line transfer sample form a polymer microfluidic chip to MALDI-MS system [15] or directly transfer from enclosed channels to target plate analysis for off-line MALDI-MS.[16] One of the off-line MALDI-MS approaches called spot-on-a-chip platform which was shown in Figure 1.2 uses of microfabricated piezoelectric actuated dispensers [17, 18] to transferring picoliter size droplet for MALDI-MS analysis. The droplets were deposited at high frequency of 500Hz maximum onto the MALDI targets with droplet size varied from 30 to 200pL.
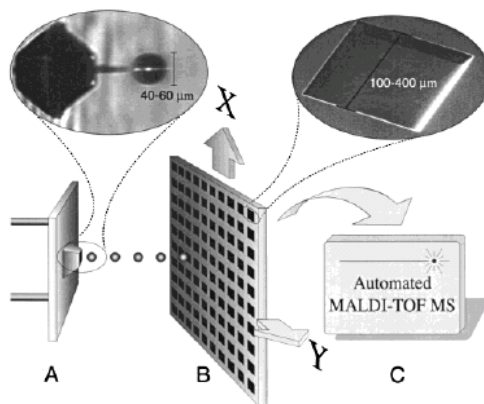
Figure 1.2: Spot-on-a-chip approach as off-line MALDI-MS analysis [17]

Electrospray deposition of matrix solution has also demonstrated [19] by Wang et al, uniform sample deposition with spots as small as 170 μm were readily produced by this approach. A novel digital microfluidic technique, called electrowetting, used electric voltage to manipulate the droplet for generating sample/matrix solutions for MALDI-MS detection.[20-22] A commercialized microfluidic device from Gyros Inc. uses centrifugal fluidic propulsion for sample preparation and MADLI-MS detection was developed.[23]

While both ESI-MS and MALDI-MS provide excellent sensitivity, wide mass range analysis, MALDI-MS provides more advantages than ESI-MS for interfacing microfluidic devices with mass spectrometry. For high throughput applications, parallel deposition samples form multi-channel onto the target plate for off-line MALDI-MS analysis is feasible while simultaneous ESI-MS analysis is not practical due to the equipment limitation. Off-line MALDI-MS interfacing provides the ability to preserve sample in a MALDI target plate so that MS experiments can be conducted without time constrains. The detection sensitivity of off-line MALDI-MS interfacing can be further enhanced by modifying MALDI target substrate. Microfabrication technologies have been widely used to modify MALDI target plate surfaces to improve the detection sensitivity. Due to the liquid sample spreading on the conventional stainless steel target plate, only small portion of deposited sample is present during the mass spectrometry scan under approximately 100~200μm diameter size. The lateral sample spreading can be physically constrained by anisotropically bulk etching on silicon based target plate [17, 24] vials or directly milling to create vials on polymer based target plate [25] to increasing local concentration. The most

common approach is done by either coating hydrophobic layer as sample support such as poly(tetrafluoroethylene) [26] and propyltrimethoxysilane [27] or by coating hydrophilic gold pad on hydrophobic Teflon background [28] to constrain the lateral spread of analyte during deposition and matrix cocrystallization.

1.2 Dissertation Objective

In many situations, biological samples are complex and contain hundreds and thousands of components. The motivation behind the current trend of microfluidics chip development is the benefits of as low reagent consumption, portability, high throughput, reducing analysis time, labor, cost and high integration levels in biological analysis application. Mass spectrometry interfacing becomes critical part for this trend which has generated lots of scientific lecture as shown in the section 1.1. Combining high-resolution bioseparation with mass spectrometry has gradually shown the great capacity in identification of proteins. The primary goal of this dissertation is development of a high throughput, low cost multiplexed polymer microfluidic device for biological analysis application. The multiplexed microfluidic chip coupled with mass spectrometry by direct robotic spotting system through Laser Desorption/Ionization Mass Spectrometry (LDI-MS). The following research objectives were performed in the dissertation:

- Investigating polymer microfluidic microfabrication technique
- Investigating a high sensitivity matrix-free laser desorption/ionization mass spectrometry target substrate

- Investigating multiplexed microfluidics - mass spectrometry interfacing technique

- Demonstrate of integrated microfluidic chip-based separation coupling with mass spectrometry

1.3 Organization

This dissertation is organized as following. Chapter 2 provides technique reviews of polymer microfluidics fabrication, bioanalytical separation and mass spectrometry techniques which are essential background knowledge. Some currently used polymer fabrication techniques may not well suited for microfabrication which may limit the polymer microfluidics device's performance. For example, the micro-scale channel may sealed or collapse by commonly used epoxy bonding, solvent bonding or thermal plastic bonding. Thus, further research and development of advanced polymer microfabrication technique is needed. Chapter 3 emphasizes on the use of UV/Ozone treatment to enhance the polymer bonding performance. Surface modification method like UV/Ozone may changes polymer surface property thus affects the polymer chip functionality. Several important properties for microfluidic device, hydrophobicity, electroosmotic flow (EOF), surface stability and UV transmissivity with UV/Ozone treatment have also characterized in this chapter. In chapter 4, a nanoscale filament-like silicon surface, called nanofilament silicon (nSi), was developed for mass spectrometry application. The matrix-free and high sensitivity (amole) performance of nSi provides unique advantages to analysis small molecules. In additional, electrowetting deposition is also developed to assist sample

deposition onto the nSi surface and the detection sensitivity can further improved through this deposition method. In Chapter 5, an automatic robotic spotting system was developed to interface microfluidic device with mass spectrometry. A single-inlet 8 channel polymer microfluidic chip has fabricated and interfaced with MADLI-MS to demonstrate multiplexed microfluidics / MALDI-MS interfacing. Spotting theory has also developed to describe and predict the droplet transport phenomena from multiplexed microfluidic chip to mass spectrometry target substrate. In the last part of this chapter, a RPLC microfluidic chip was developed and interfacing with nSi substrate to demonstrate high performance bioseparation / nSi-MS interfacing. In the last part, Chapter 6, it concludes the progress and contributions from this research and provides recommendations for the future work.

Chapter 2 Technical Background

2.1 Biological Separation Technique

Separation plays an important role to analysis complex biological samples. Most commonly used separation techniques in analytical chemistry system as well as in analytical microfluidic devices are chromatography and electrophoresis. Chromatography separation uses physicochemical difference which is suitable for both charged and uncharged molecules. Chromatography separation requires a stationary phase which the mobile phase and the mixture can be separated. On the other hand, electrophoresis can be used for charged molecules which are separated in an electric field according to their mass-to-charge (m/z) ratios. General analytical separation principle of chromatography and electrophoresis were illustrated in the following: At the beginning of separation process, a small sample plug is injected into the separation channel at the inlet and then the separation process starts by pumping liquid or apply electrical field to driving the analyte to the outlet or detector. Due to the difference in physical or chemical property of analytes, the analyte migrate at different velocity and arriving outlet or detector at different times and generate the chromatogram as shown in the Figure 2.1. The time for the analyte to reach the detector is called retention or elution time. The peak height is proportional to the analyte concentration. The peak width represents separation efficiency, the narrower the peak, the higher separation efficiency and higher number of theoretical plate.
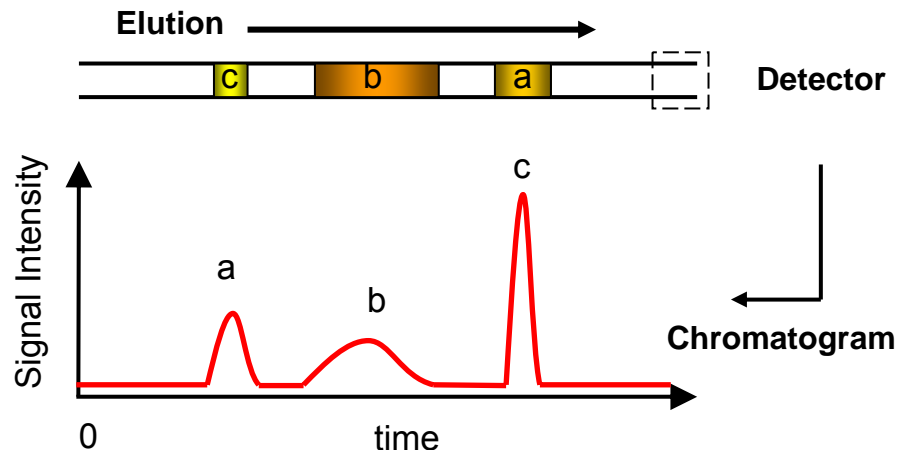
Figure 2.1: Liquid chromatography retention time

Chromatographic methods can be classified into gas chromatography (GC) and liquid chromatography (LC) depending on the nature of the mobile phase involved. Due to its high performance to separate and identify compounds that are present in any liquid phase sample, liquid chromatographic also called High Performance Liquid Chromatography (HPLC) and it is now become one of the most powerful tools in analytical chemistry. A number of different HPLC techniques are used for protein/peptide separation. They can be classified according to the physical principle involved in the separation process. Typical examples include reversed phase liquid chromatography (RPLC), ion exchange chromatography, affinity chromatography and size exclusion chromatography (SEC). Reversed phase chromatography is the most popular method of choice for the separation of smaller biomolecules such as peptides, amino acids and steroid which are soluble in water/acetonitrile mixture.

RPLC is an adsorptive process. The separation mechanism in reversed phase chromatography depends on the hydrophobic interaction between mobile phase and the stationary phase. In RPLC, the stationary phase is made of non-polar materials

and the mobile phase consists of polar-solvents. The stationary phase usually consists of porous silica particles with non-polar surface groups. The surface group is obtained from etherification of the initial hydroxyl groups on the silica particle with silanes containing non-polar hydrocarbon chains such as octyl silane (C_8) and n-octadecyl silane (C_{18}). For analytical separations, the particle size is typically 5μm or smaller and to achieve ambient flow rates in these columns, high pressure up to 300~400 bar are usually required. The mobile phase is based on a polar solvent system consisting of an aqueous buffer and acetonitrile or methanol. Graduation elution is often employed to increase resolution and shorten separation times. This is achieved by increasing the organic solvent and thus decreasing the mobile phase polarity and the retention of less polar analytes during the separation process. After elution from the column, the analytes pass through the detector for identification.   In HPLC separation, the theoretical plate number N is given by:

$N = \dfrac{L}{2\lambda D} m$, where D is diffusion coefficient of an analyte, λ is the hindrance factor

depend on the characteristic of packing, m is the overall migration velocity of the analyte in the column and L is the column length. In which, the velocity of analyte in a packed column is proportional to the pressure drop P between the column ends and

this can be represent as: $m = \dfrac{P d_P^{\,2}}{180 \eta L} \cdot \dfrac{\varepsilon^2}{(1-\varepsilon)^2} \cdot \dfrac{1}{1+k}$ where k is the capacity factor of

the analyte, η is the viscosity of the mobile phase, d_p is the packing particle diameter and ε is the porosity of the packing column. The analysis time t can be present as t=L/m, so the theoretical plate number per unit time can be present as

$$N/t = \frac{\varepsilon^4}{64800\eta^2 \lambda D(1-\varepsilon)^4(1+k)^2} \cdot \frac{P^2 d_p^4}{L^2}$$

Thus, the optimization of chromatography is aimed towards completely separating all components in shortest time with highest theoretical plate number. This can be achieved by modifying the choosing stationary phase and mobile phase or changing the flow rate which can be seem from the equation illustrate previously. To achieve high separation performance, high pressure normally required which brings technical challenges in implementation HPLC microchip to withstand high pressure without leaking.

2.2 Mass Spectrometry (MS)

Mass spectrometry is an analytical technique that measures the masses of individual molecules and atoms. Mass spectrometry has become most widely used detection method in chemistry and biochemistry field due in the results of the following reasons:

- Compare with optical detection methods, mass spectrometry provides a superior molecular specificity which can provide molecular weight and molecular structure of the analyte

- Mass spectrometry provides high detection sensitivity normally in fettomole or sub-attomole range [17, 28-30]

- Mass spectrometry provides unique capability to combine with high-resolution separation techniques to analyze real-world complex samples

13

A mass spectrometry consists of three major units, an ionization source, a mass analyzer and an ion detector. An ion source converts sample molecules into gas-phase ionic species, so the sample can be analyzed and detected. Excessive energy transfer to the molecular during ionization leads to fragmentation which provides molecular structure information. Next, an analyzer is to separate these molecular ions and charges fragments according to mass/charge (m/z) ratio. The performance of a mass analyzer is based on high mass range, high resolution, fast scan speed and high detection sensitivity criteria. Several designs of mass analyzer have been developed; magnetic sector, quadrupole, quadrupole ion-trap (QIT) and time-of-flight (TOF) instruments have becomes popular recently. Finally, the ion current is detected by a detector to measure the relative abundance of mass-resolved ions and displayed in mass spectrum form. To enable the ions to move freely in space without colliding or interfacing with other species, each of these steps is usually carrier out under high vacuum.

The first essential step in mass spectrometry analysis is to convert the analyte molecules into gas phase ionic species. The success of a mass spectrometry experiment relies to a large extent on the way of sample is transferred into ionic species. In biomolecular analysis, electrospray ionization (ESI) and matrix-assisted laser desorption/ionization (MALDI) are now the most common ionization sources for mass spectrometry which offers excellent mass detection range up to hundreds kilo-Dalton range and mass sensitivity down to femtomole (fmol) range.

2.2.1 Electrospray Ionization (ESI)

Electrospray ionization for mass spectrometry was accomplished by Dole et al in late 1960s. The gas-phase ions are generated from electrically charged liquid droplets produced by electro-spraying the analyte solution.[31] In late 1990s, Fenn et al developed the technique of electrospray ionization mass spectrometry and apply to biological molecules.[32, 33] Electrospray ionization involves three different processes: (1) Droplet formation (2) Droplet shrinkage and (3) gas-phase ion formation. An illustration of electrospray ionization process is shown in Figure 2.2. In first step of electrospray process, the electrostatic force in the liquid causes it to emerge from the tip of the capillary as jet in the shape of a "Taylor cone" A thin liquid extends from this cone which breaks into tiny droplets. The mist droplets contain analyte molecules, solvent and charge ions. Next, the solvent evaporates transferring the charged ions into analyte molecules and transport into mass analyzer. A number of factors such as applied potential, capillary diameter, solvent characteristic (composition, flow rate, conductivity and surface tension) will profoundly influence the operation of electrospray process.
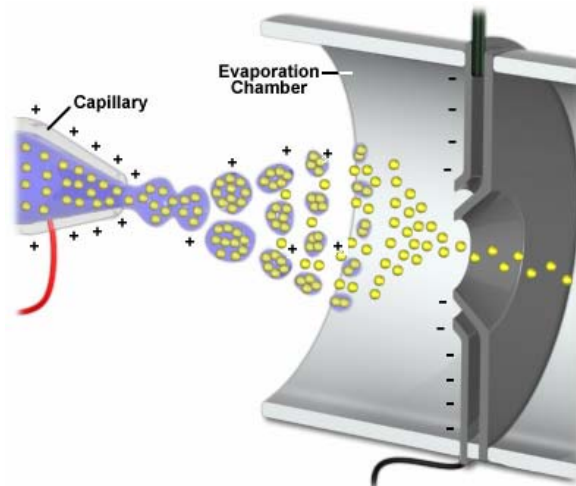
Figure 2.2 Electrospray ionization (ESI) mass spectrometry

Electrospray ionization is conductive to the formation of singly charged small molecules, but it is also well-known for producing multiply charged species of large molecules.

2.2.2 Matrix-Assisted Laser Desorption/Ionization (MALDI)

MALDI was first introduced by Michael Karas and Franz Hillenkamp[34] in 1980s and it has been more recently reviewed by Ronald Beavis and Brian Chait [35]. The efficient and directed energy transfer during a matrix-assisted desorption event provides intact ionized molecules and allows for the measurement of heterogeneous samples make it very attractive for the mass analysis of biological samples. Thus, MALDI has significantly revolutionized the approaches to the study of large biopolymers and becomes widely used analytical tool for peptides, proteins and other biomolecules like oligonucleotides, carbohydrates, natural products and lipids. Synthetic polymers with high molecular weight are also studied by MALDI.
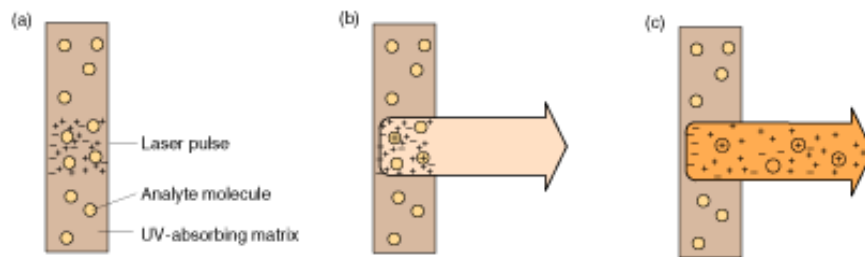
Figure 2.3: Schematic mechanism for MALDI [36]

The matrix in MALDI perform two important functions: (1) It absorbs photon energy from laser beam and transfer it into analyte (2) It serves isolated the analyte from each other and intermolecular forces are reduced. The schematic mechanism of MALDI MS is show in Figure 2.3. First, the matrix absorbs energy from the pulsed laser beam when Energy from the laser beam is absorbed by the matrix, which rapidly expands into the gas phase, entraining analyte molecules as well. Ionization occurs by proton transfer between excited matrix molecules and analyte molecules. Once the analyte are ionized as gaseous phase, the analyte ions are accelerated to towards the TOF analyser under electrical field and measure the mass/charge (m/z) ratio.

Once in the gas phase, the desorbed charged molecules are then directed electrostatically from the MALDI ionization source into the mass analyzer. Many types of mass analyzer has used with MALDI like time-of-flight (TOF), fourier transform (FT), magnetic sector and etc. Among those TOF analyzer are most commonly used in MALDI, Time-of-flight (TOF) analyzers were chosen for the mass separation of ions being produced by laser pulses due to several advantages, including: high ion throughput resulting in high sensitivity, ease of construction and operation, theoretically unlimited mass range and ideal for mass separation of ions

being produced by pulsed methods. With MALDI-TOF, molecular weights above 500 kDa can be determined with fmol sensitivity. The time-of-flight (TOF) analyzer allows for high resolution and accurate mass determination even for high molecular weight species. The ions desorbed by the laser energy of several keV, then enter a field free tube in which they drift along with different speeds according to their mass/charge ratios. At the end of the tube, the ions hit a detector and the drift time is measured electronically with high accuracy. The kinetic energy if the drifting ions can be defined as:

$$E_{kin} = \frac{1}{2}mv^2 = z \cdot e \cdot V \tag{1}$$

Where m is the mass of the ion, v is the velocity of the ion after the acceleration region, z is the ion charge, e is the elementary charge and V is the voltage of the applied electrical field. The velocity v can also defined as the length of the drift tube, L, divide by the time of flight, t. Substituting the velocity v in equation (1) leads for

$$E_{kin} = \frac{1}{2}mv^2 = z \cdot e \cdot V \Rightarrow \frac{m}{z} = \frac{2 \cdot e \cdot V}{L^2} \cdot t^2 \tag{2}$$

The m/z ratio if the ion is proportional to the square of the drift time. Hence, the mass of an ion can be determined by measuring its drift time. The utility of MALDI for biomolecules analysis lies in its ability to provide molecular weight information on intact molecules. The ability to generate accurate information can be extremely useful for protein/peptide identification and characterization. As result, a protein can be unambiguously identified by the accurate mass analysis of its constituent peptides. Summarize of ESI and MADLI advantages and disadvantages are listed in Table 2.1.

	Advantages	**Disadvantages**
ESI	- Mass range up to 70,000 Da - Good sensitivity with femtomole to low picomole - Softest ionization method, capable generating noncovalent complexes in gas phase - Easily adaptable to liquid chromatography - Multiple charging allows for analysis of high mass ions with a relatively low m/z range instrument - No matrix influence	- the presence of salts and ion-pairing agents can reduce sensitivity - complex mixture can reduce sensitivity - multiple charge can be confusing especially in mixture analysis - sample purity is very important, less tolerance to contamination
MALDI	- Practical mass range of > 300,000 Da - Typical sensitivity on the order of low femtomole (fmol). Attomole (amol) is possible - Soft ionization with little to no fragmentation observed - Tolerance of salts in millimolar concentration - Suitable for analysis of complex mixtures	- Matrix background, which can be a problem when analysis below a mass of 700 Da. - Acidic matrix used in MADLI may cause degraduation on some compound

Table 2.1: Disadvantages and advantages of MALDI and ESI

2.3.3 Desorption / Ionization on Silicon (DIOS)

In addition to the study of large biomolecules, MALDI-MS is also widely used for the analysis of small molecules such as drugs, peptides, and synthetic polymers. For the analysis of small molecules, it suffers from the disadvantage of excessive matrix background, which creates problems in the analysis of small molecules. To accomplish laser desorption ionization with good sensitivity and free of chemical background, new materials have been explored to facilitate laser desorption and ionization without the involvement of a MALDI matrix. Siuzdak et al [37], have introduced a new technique, called Desorption/ Ionization on Silicon (DIOS) is the most successful and has been commercialized by Waters Inc.[38] As shown in Figure

2.4, instead of mixing with a matrix, the samples are directly placed on a porous surface and bombarded with beam of laser. Porous silicon surface is UV absorbing semiconductors with large surface area around hundreds of m^2/cm^3. For its application to mass spectrometry, the porous silicon provides a scaffold for retaining solvent and analyte molecules. And the silicon surface UV absorbance provides a mechanism for the transfer of laser energy to analytes. The usefulness of this approach was demonstrated for a large variety of biomolecules including peptides, carbohydrates and small organic compounds. Similar to MALDI, DIOS enables desorption/ionization with little or no analyte degradation or fragmentation. And also, excessive amount of salts do not interfere in the analysis.

DIOS is compatible with MALDI instrument which only acquires minor adjustment to the tool setup. The DIOS substrates are simply affixed to a machined substrate holder and inserted into the mass spectrometer. The same wavelength of laser light (337nm) typically used in MALDI instrument is effective for DIOS. While DIOS is comparable to MALDI with respect to its sensitivity, it has several advantages due to the lack of matrix interference, low background in the low mass range, uniform deposition if aqueous samples and simplified sample preparation. In addition, the chip format is adaptable to automated sample handling. DIOS substrate is advantageous for simple, high throughput small molecular analysis like MALDI has done for macromolecules. The sensitivity of DISO substrate has demonstrated that peptide could be analyzed at the levels as low as 700amol.[37] By silylation of an oxidized porous silicon surface, an unprecedented detection limit of 800 ymol for des-Arg^9-bradykinin could be achieved on a silylated DIOS chip.[39]
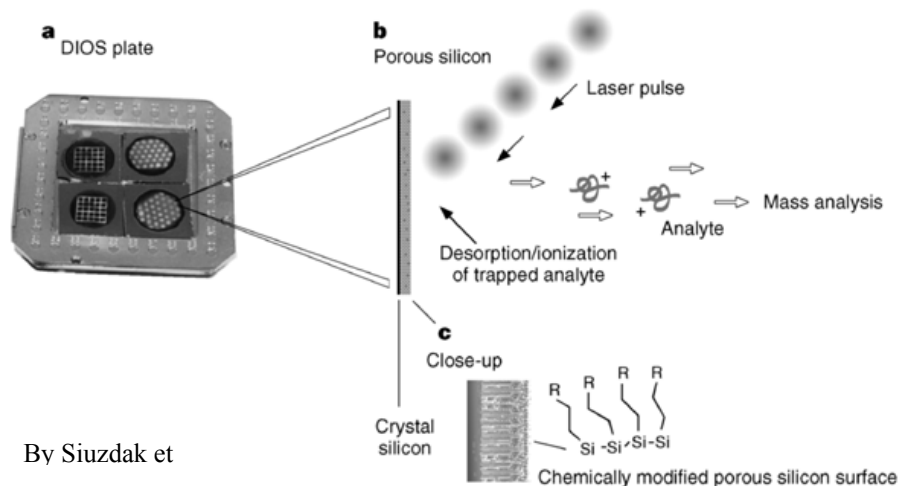
By Siuzdak et

Figure 2.4: Desorption/ Ionization on Silicon (DIOS) [37]

2.3 Polymer-based Microfabrication Technologies

In early stage, most of the microfluidic chips fabricated on glass or quartz and silicon substrate [40]. Silicon based microchip are not transparent may limit application for optical detection device. Glass substrates have superior optical transmissivity but fabricating of microscale structure on glass may be challenging. Polymer substrate, on the other hand, is attractive alternatives for its wide range of available plastic material properties which allows researchers to choose material's suitable for their specific application.

Briefly, microfluidic microstructures design are first created on a high-resolution mask. Masks are normally fabricated on quartz, glass, soda lime glass or even transparent film for good UV transmission during UV exposure step. Then, the mask transfer designed pattern onto template substrate by standard UV lithographic process. The inverse master template can be fabricated by either dry or wet etching

process. Polymer replica is generated upon the master by polymer replica technology like hot embossing or injection molding. Finally, the polymer replicas are sealed by another piece of polymer via polymer bonding to create microfluidic chip. The general fabrication process flow for microfluidic devices is shown in Figure 2.5.

| Mask Design | $\Rightarrow$ | Template Fabrication | $\Rightarrow$ | Polymer Replica | $\Rightarrow$ | Polymer Bonding |
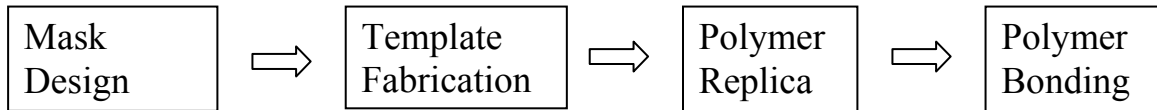
Figure 2.5: Schematic illustration of general polymer microfluidics fabrication process

In additional to the advantage of capable of replica fabrication, the cost of the polymer fabrication and polymer material is less expensive than conventional silicon or glass based microfluidic chip which brings industrial interest in choosing polymer substrate as cheap disposable microfluidics device. Figure 2.6 shows a typical polymer microfluidic chip made from polycarbonate (PC) used for bioanalytical analysis application.
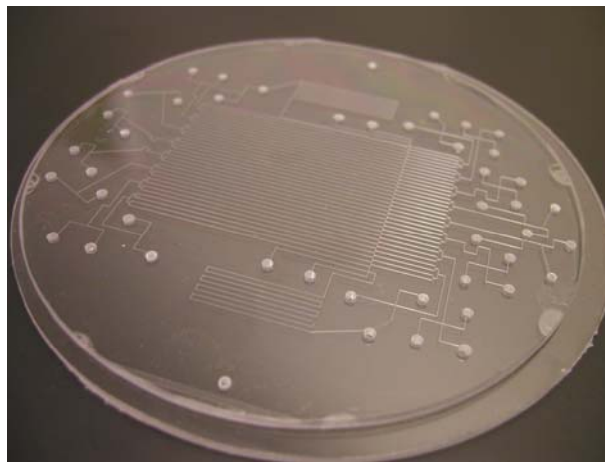
Figure 2.6: Polymer microfluidic chip for IEF-CGE separation

2.3.1 Polymer Substrate Selection

A growing number of polymer microfluidics have been investigated recently, a wide variety of polymer materials have been used for microfluidics. Polymer microfluidic device can be divided into two categories: elastomer and thermoplastic polymer. Elastomers are usually called thermosets which is amorphous polymers existing above their glass transition temperature (T_g) and it don't not melt until reaches its melting temperature. Elastomers consist of weakly cross-linked polymer chains having the elastic properties of natural rubber. If an external force is applied, the polymer chains can stretched and deformed. When releasing the stress, it returns rapidly to approximately the initial dimensions and shape. Poly(dimethysiloxane) (PDMS) is the most widely used elastomer for polymer microfluidic device. Thermoplastics have crystalline stage alternating with amorphous stage in which the polymer chains changes from orientated crystallized coil into flexible random coils. The amorphous regions contribute elasticity and the crystalline regions contribute strength and rigidity. When heats thermoplastic above its Tg, the crystallized polymer chains becomes amorphous stage which can be deformed by external force. Thermoplastic polymer can be molded into specific shapes and it will retain the shapes after cooling below Tg. Thermoplastics like polycarbonate (PC), poly(methyl methacrylte) (PMMA), polyamide (PA), cyclic olefin copolymer (COC), polyethylene (PE), and polystyrene (PS) are more widely used due to its good rigidity and mechanical property.

When choosing a polymer as substrate material, it is important to determine the polymer properties meet its fabrication process and application. Different

fabrication techniques have different specific constrains with regard to the properties of the materials. For examples, with hot embossing and injection molding, the glass transition temperature, melt temperature are some of the critical parameters for successful fabrication. When using optical detection, good optical properties are important to have good detection sensitivity. In bioanalytical applications, organic solvents and acid/base solution are usually required, so good solvent and chemical resistance polymer materials are critical. Other properties such as hydrophobicity, machinability, water absorbency, and moisture permeability are also need to consider. Among all of the polymers been used in microfluidic device, two most particular thermoplastics, poly(methyl methacrylate) (PMMA) and cyclic olefin copolymer (COC), have emerged as attractive materials for microfluidic substrate for bioanalytical applications. Both COC and PMMA have advantages of good mechanical property, good chemical resistance, high optical transparency and low autofluorescence over a wide spectral range [41] which can be an ideal substrate used in microfluidic systems. The comparison of optical property, chemical resistance and processability of PMMA and COC are listed in

Table 2.2.

While both PMMA and COC are widely used material for hot embossing and injection molding. COC appear to be more appearing substrate material as microfluidics chip used in bioanalytical applications due to its superior chemical resistance and optical property. Reviews of the polymer properties as well as fabrication methods for polymer microfluidic were reported by Becker and Locascio [42-44].

	PMMA, Optix Acrylic [45]	**COC, Zenor 1020R [46]**
Processability	Hot embossing Injection molding Direct milling	Hot embossing Injection molding Direct milling
Light Transmittance	92%	92%
Acid/Base Resistance	Diluted acids, base	Diluted and concentrated acids and base
Solvent Resistance	Methanol, isopropanol	Acetone, acetonitrile methylethylketone, methanol, isopropanol,
Water absorption	0.4%	<0.01%
UV transmittance	Good	Good
Glass transition temperature	105-110 C	105 C

Table 2.2: Comparison of properties of PMMA and COC

2.3.2 Polymer Replica Fabrication Technology

Fabrication of polymer-based microfluidic device is simple, the microstructure on polymer substrate can be made by either prototyping method like micro-milling [47] and laser ablation.[48] or mass production method like hot[49], cold [50] embossing and injection molding.[51] In additional to that, another big advantage of polymer based microfluidics device is its low raw material cost which is ideal to use as disposable polymer chips for commercial applications. So development of low-cost, high-throughput manufacturing process is also a crucial step to achieve this goal. Low-cost high-throughput polymer replication technologies like casting and injection molding are already been widely used to produce all kinds of macroscale polymer components. The principles of polymer replication technology in macroscale have been widely studied. The underlying principle of polymer replication technology is mold fabrication which represents the negative / inverse structure of desired

polymer structure. Once the mold has been fabricated, it can be replicated polymer substrate more than hundred times by polymer replication technology.

Template fabrication

Good micro scale mold fabrication is an important first step for success polymer device fabrication. Most of micro scale molds are fabricated based on standard lithography process. Various of template fabrication techniques have been developed. Silicon micromachining, photoresist lithography and electroplating are three major fabrication techniques as shown in Figure 2.7. Nickel Electroplated template is most common use in injection molding for polymer replication. The electroplating method normally starts with standard photolithography. The template base was first coated with photoresist and development into desired pattern with a conducting electroplating seed layer. Then the template base was dip into a galvanic bath. Due to the ion migration between the seed layer and the bath, the metal starts to grow on the seed layer. Finally, the photoresist was removed and leaving the resulting metal structure on the template base. The resulting nickel-based templates have good mechanical property and good surface chemistry for most polymer microfabrication process. However, electroplating is a time consuming process due to the slow growth rate of the nickel in the electroplating process. In addition to the adhesion to the substrate seed layers and deposition, uniformity is the other issue to be considered for electroplating. Another major category is using photoresist lithography, more and more research groups have use this technique for hot embossing process because it is simple and high aspect ratio microchannel arrays can be created in one spin-coat step

26

without high cost equipment. SU-8 template is the most widely used material due to its good mechanical, chemical property and simplicity. However due to the coefficient of thermal expansion (CTE) mismatch of SU-8 and silicon substrate and poor adhesion between the SU-8 and the silicon substrate, the SU-8 microstructure may delaminate after hot embossing process.
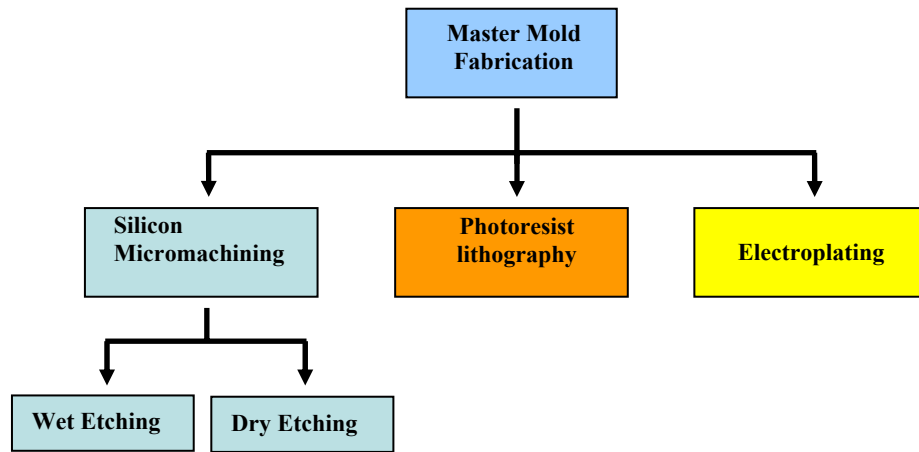
Figure 2.7 Master template fabrication technique

Silicon based microfabricated technology was been well developed and been widely used in semiconductor and MEMS field. Silicon has high level of stiffness, high heat conductivity and high heat resistance which is a suitable material for a mold tool. Silicon based micromold can be fabricated by either wet etching or dry etching. Wet etching is a chemical etching process, the silicon templates are usually fabricated by dipping the silicon substrate into etching solution such as potassium hydroxide (KOH). The wet etching on <100> silicon results in a structure with a wall angle of 54.7 degree presents the drawback of anisotropic wet etch silicon template and it also

creates trapezoid-shape microchannel which limits the high density, high aspect ratio pattern design.

Dry etching method, like reactive ion etching (RIE), is an alternative silicon microfabrication method to create silicon based template. In this method the substrate is placed inside a reactor in which several gases are introduced. Plasma is exciting the gas mixture using an RF power source, breaking the gas molecules into ions. The ions are accelerating towards and react with the silicon surface to etch the silicon material. A special subclass of RIE which continues to grow rapidly in popularity is Bosch patented deep RIE (DRIE) process. In this process, etch depths of hundreds of micron can be achieved with almost vertical sidewalls. The first gas composition creates a polymer on the surface of the substrate (passivation step), and the second gas composition etches the substrate (activation step). The polymer is immediately removed away by the physical part of the etching, but only on the horizontal surfaces and not the sidewalls. Since the polymer only dissolves very slowly in the chemical part of the etching, it builds up on the sidewalls and protects them from etching. As a result, aspect ratios up to 50 can be achieved.

The silicon based DIRE etched template was developed using STS DRIE system (Surface technology systems, Newport, UK). With 6.5 second passivation time and 10 second activation time followed by 140 cycles of etching, the resulting DRIE etching silicon template is shown in Figure 2.8 with an average depth of 44 μm.
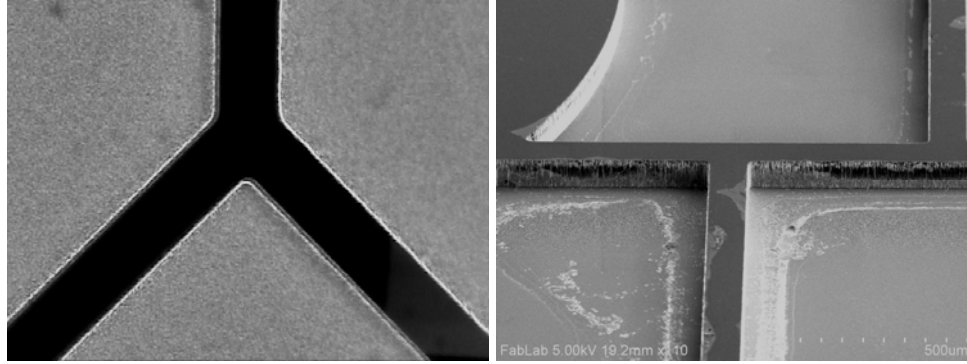
Figure 2.8: DRIE etched template

Because of the area dependent nature of DRIE process, the etching depth is different from different open areas in the same process. In other words, the etching rate is faster for the wider area than the narrower area (also called RIE lag). With care control during etching, the depth variation of resulting DRIE etched silicon template is less than 2% based on profilometer measurement result.

Hot embossing

Rigid thermoplastic polymers have been extensively investigated over the past decade as substrates for the fabrication of microfluidic systems. The most widely used and most straightforward replication process to fabricated polymer microfluidic device is hot embossing. The microfabrication process of hot embossing itself is rather simple and the feature dimension down to micrometer [52] to nanometer scale [53] have been demonstrated. Polymer replicas created by hot embossing process are usually done by a hydraulic press. Schematic illustration of hot embossing process is shown in Figure 2.9, the machine has a top stationary hot platen and a bottom movable hot platen where the imprinting template and polymer were placed.
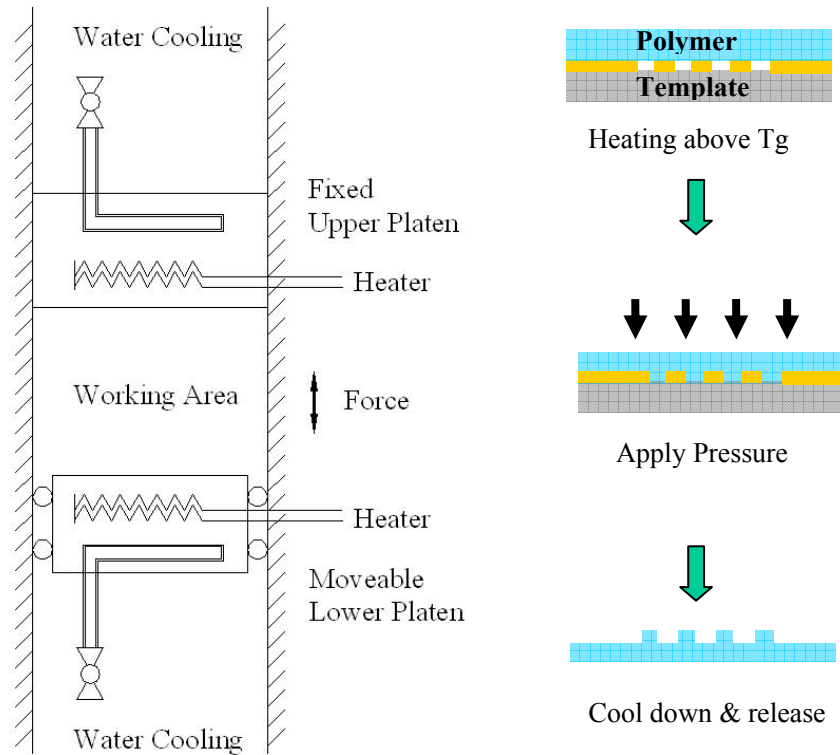
Figure 2.9: Schematic illustration of polymer hot embossing process

The thermoplastic polymer substrate was heated above its glass transition temperature. Then the movable bottom platen moves up applying a pressure between the polymer substrate against a template containing features that represent the inverted features desired in the final embossed part. After applying pressure on a certain time, the substrate is cooled down below its glass transition temperature by water cooling system while still applying the embossing pressure before removing from the master structure. A vacuum chamber can be used to provide high vacuum during the entire hot embossing cycle. Vacuum was used to prevent the formation air bubbles due to air entrapment in the cavities during embossing procedure. During imprinting process, thermally induced stress may cause replication errors due to the

30

coefficient of thermal expansion (CTE) mismatch between polymer substrate and imprinting template. During the end of hot embossing process, the temperature cools down and about to release polymer substrate, the imprinting template is mechanically driven apart from the polymer substrate. In this step, high forces may act on imprinting template as well as polymer substrate. As result, either imprinting template or polymer microstructure may damage, particularly if high aspect ratio vertical walls are desired.

Control of hot embossing process is critical to have good imprinting result and prevent damage of template hence increase life time of imprinting template. Hot embossing experiment on a Cyclic Olefin Copolymer (COC) was performed to determine the hot embossing performance. The hot embossing process includes four important control parameters to determine success fabrication. Those control parameters are embossing temperature, demolding temperature, embossing pressure and dwell time. During hot embossing process, the polymer substrates first need to heat above its glass transition temperature (T_g) before applying embossing pressure and then the polymer substrate need to cool down below its glass transition temperature (T_g) before release polymer substrate from the embossing template. This thermal cycle should be as small as possible to minimized thermally induced stress. From the glass transition temperature (T_g) of COC (Zenor 1020R) is 105℃, the design variables are choose as Embossing Temperature: 110℃, 130℃, Demolding Temperature: 85℃, 100℃, Embossing Pressure:150, 300 Psi and Embossing Time: 5,15 (min). The design of experiment is listed in the Table 2.3 and the template layout for this experiment is shown in Figure 2.10.

Set	1	2	3	4	5	6	7	8	9	10	11	12	13	14	15	16
Embossing Temp (℃)	110	130	110	130	110	130	110	130	110	130	110	130	110	130	110	130
Demolding Temp. (℃)	100	100	85	85	100	100	85	85	100	100	85	85	100	100	85	85
Pressure (Psi)	150	150	150	150	300	300	300	300	150	150	150	150	300	300	300	300
Time (Min)	5	5	5	5	5	5	5	5	15	15	15	15	15	15	15	15

Table 2.3: Design of variables for COC imprinting
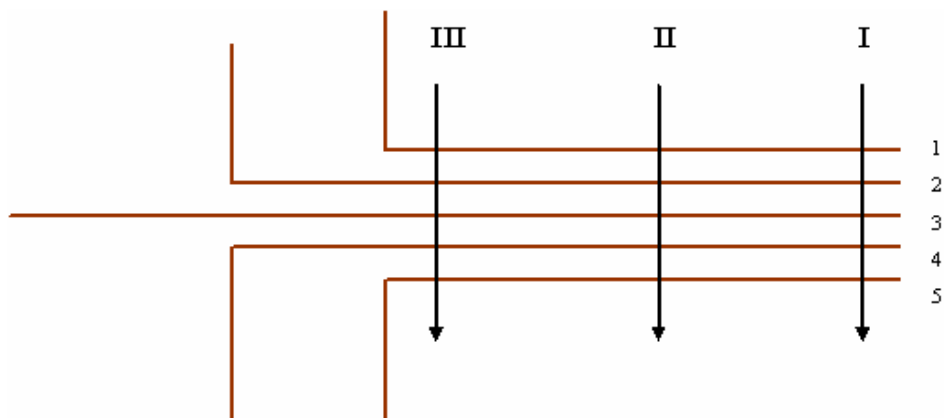
Width (Top): 105.6 um

Width (Bottom): 105.4um

Height: 53.1 um

Figure 2.10: Hot embossing experiment design layout

After hot embossing, PDMS replica was taken from each polymer imprint set to evaluate the channel dimension form PDMS cross-section. The measured PDMS replica height, top and bottom channel width on section I, II and III section shown in Figure 2.10 were measured via optical microscope.

Round Edge
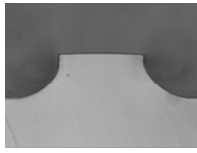
Good imprinting
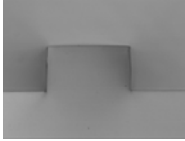
Incomplete imprinting
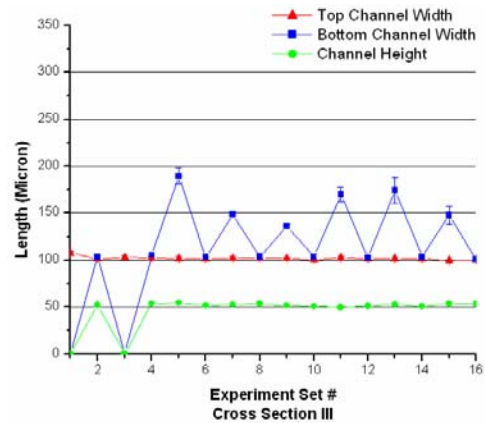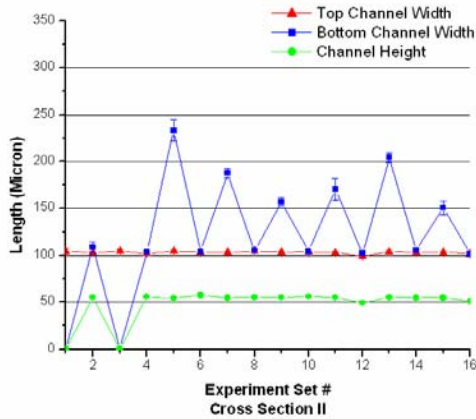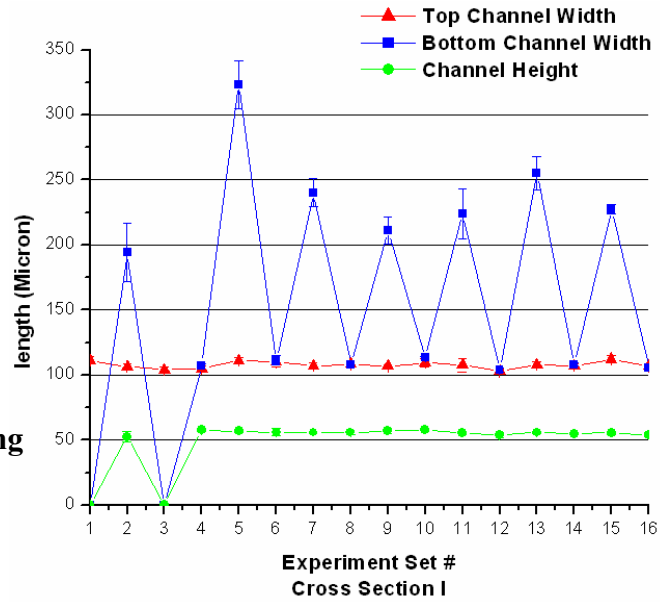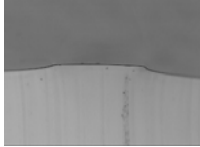
Figure 2.11: Hot embossing test with different hot embossing temperature, pressure demolding temperature and dwell time on crossection I,II and III

Five measurements have performed on each experiment set and the average of the channel width and height are shown in Figure 2.11. The cross-section I measurement shown in Figure 2.11 was observed that with the low imprinting temperature (Set 5,7,9,11,13), round edge have observe at the bottom edge due to low

hot embossing temperature (110℃). When hot embossing temperature is slightly higher than the glass transition temperature, the polymer is not fully transfer into amorphous stage. So the polymer reflow is more viscous under lower hot embossing temperature for complete pattern transfer. Thus, it is also observed that with high imprinting temperature (Set 4,6,8,10,12), the pattern is well transfer to the polymer. Under low pressure, low dwell time and low imprinting temperature condition (Set 1,2,3), the imprint is not complete. It is also note that the demolding temperate has little effect on the pattern transfer. Similar tendency have observed in the cross-section II and III shown in Figure 2.11. This experiment helps to develop and evaluate various hot embossing process conditions to get good hot embossing replica polymer substrate. The COC hot embossing process in this dissertation was using 125℃ as embossing temperature and 95℃ as demolding temperature with 100 psi embossing pressure for 10min.

Injection molding

Injection molding is a widely used polymer replication method for conventional polymer pieces with dimensions from millimeter to centermeter. Injection molding has also demonstrated as replication method for polymer microfluidic device in recent publications. [51, 54, 55] The cross diagram of microinjection-molding machine is shown in Figure 2.12. The process starts with the raw polymer material which comes in pellet form. These polymer pellets are filled to extruder screw where pellets start heated and melted. The molten polymer is then transported toward the mold cavity and injected under high pressure typically around

hundreds MPa. Typical temperature in this region ranges from 200°C for PMMA to 280°C for PC. This injection cavity was kept under vacuum to allow for a good mold fill in the case of microstructures. In macro/meso-scale injection molding, the mold cavity can be held below polymer solidification temperature to reduce cycle time of only couple seconds. When structure become smaller, less material needed injected into the cavity, the mold cavity has to be pre-heated closer to the polymer melting point to ensure good mold fill before polymer solidify. Typical cycle time of microinjection molding is around 1~3 minutes. Compare to other polymer replication methods like hot embossing, injection molding is more suitable method for mass production.
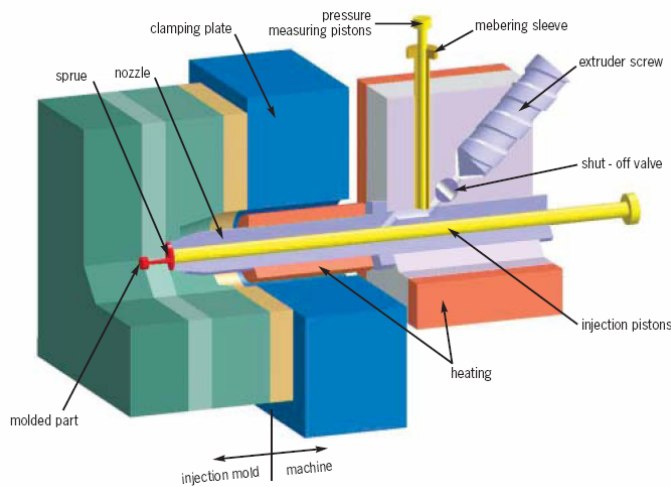
Figure 2.12 Cross-sectional diagram of a microinjection molding machine [56]

2.3.3 Polymer Bonding Technology

After polymer replica was fabricated, a second plastic layer is then bonded to the first to enclose the microchannels to enable fluids to be manipulated within microstructures. A variety of suitable bonding methods have been reported, including solvent bonding,[57-59]

thermal bonding,[60, 61] and thick film lamination employing either pressure or temperature sensitive adhesive layers.[62]

Adhesive bonding

One of the well known and the simplest bonding method is gluing. In which, a thin film of glue is applied to one or two polymer surfaces then two parts are pressed together. The glue at the bond interface was then cured and hardened to form a bond between two polymers. A large variety of adhesive material is commercially available. The activation can take place either by simple solvent evaporation, by irradiation with UV-light, by heating or applying pressure. The biggest issue of adhesive bonding is the fact that the glue may overflow into the microstructures or microchannels, therefore destroying the chip functionality. This drawback limits the use to bond polymer microstructures.

Thermal bonding

Thermal bonding is a process that the polymer parts are pressed together by heating the substrates near their glass transition temperature. Thermal bonding is process believed that due to melting of surface layers of the polymer substrate allowing polymer chains to diffuse between the mating surfaces that are pressed together. After cooling below its glass transition temperature, the two parts are permanently bonded at high bond strength. The heating procedure in thermal plastic bonding results in softening the polymer and may cause destruction of the microstructure, especially under pressure. Care must be taken to find the right

pressure and temperature to allow efficient bonding strength without damage the polymer microstructures or microchannels.

Solvent bonding

In solvent bonding process, the interface between two polymer parts are dissolve by suitable solvent and the bonded interface solidified in the subsequent solvent evaporation to combine two polymer parts. The critical aspect of solvent bonding is the prevention of gluing or melting microstructure during solvent bonding process. This can be prevented by precise control of solvent amount through gas evaporation with superior bond strength without channel collapsing for high-pressure applications.

Of these techniques, solvent and thermal bonding are of particular interest since they allow the same material to be used for both microfluidic substrate layers, ensuring homogeneity in surface properties for all microchannel walls. However, thermal bonding suffers from several disadvantages. Because the substrates must be heated at or slightly above their glass transition temperature to achieve a strong interfacial bond, microscale channels can readily become deformed or collapsed, particularly for low aspect ratio channels and thin substrates. Furthermore, the resulting bond strength is often lower than desired, particularly for applications such as liquid chromatography where high internal fluid pressures are required.

Solvent bonding can also suffer from problems with dimensional stability, since the absorbed solvent softens the plastic and can lead to polymer flow during bonding. While recipes have been developed to minimize this problem in PMMA microfluidic chips by using specific solvent conditions[59, 63] or sacrificial materials such as

paraffin wax to prevent channel collapse,[61] the former recipes must be tuned for different polymer grades and types, and neither approach can entirely prevent deformation of channel geometries. Furthermore, solvents can embrittle thermoplastics and result in microcracking, particularly for microfluidic systems which require exposure to high or cyclical pressure loads. Because of these challenges, there remains a need for effective methods for low temperature thermoplastic bonding which are amenable to a wide range of microfluidic applications. A new bonding method, called UV/Ozone bonding is developed in the dissertation and discussed more detail in next chapter.

Chapter 3 Low Temperature Bonding Technique

Rigid thermoplastic polymers have been extensively investigated over the past decade as substrates for the fabrication of microfluidic systems. Two particular thermoplastics, poly(methyl methacrylate) (PMMA) and cyclic olefin copolymer (COC), have emerged as attractive materials for microfluidic applications, primarily due to their high transparency and low autofluorescence over a wide spectral range[41]. In a typical process flow, open microchannels are formed in first a thermoplastic substrate using one of several techniques such as hot[49] or cold[50] embossing, micro-injection molding,[51] or laser ablation.[48] A second plastic layer is then bonded to the first to enclose the microchannels. A variety of suitable bonding methods have been reported, including solvent bonding,[57-59] thermal bonding,[60, 61] and thick film lamination employing either pressure or temperature sensitive adhesive layers.[62] Of these techniques, solvent and thermal bonding are of particular interest since they allow the same material to be used for both microfluidic substrate layers, ensuring homogeneity in surface properties for all microchannel walls. In thermal bonding, interlayer adhesion is achieved by heating the substrates near their glass transition temperature while applying a normal pressure, allowing polymer chains to diffuse between the mating surfaces for high bond strength. However, thermal bonding suffers from several disadvantages. Because the substrates must be heated at or slightly above their glass transition temperature to achieve a strong interfacial bond, microscale channels can readily become deformed or collapsed, particularly for low aspect ratio channels and thin substrates. Furthermore,

the resulting bond strength is often lower than desired, particularly for applications such as liquid chromatography where high internal fluid pressures are required. Solvent bonding can also suffer from problems with dimensional stability, since the absorbed solvent softens the plastic and can lead to polymer flow during bonding. While recipes have been developed to minimize this problem in PMMA microfluidic chips by using specific solvent conditions[59, 63] or sacrificial materials such as paraffin wax to prevent channel collapse,[61] the former recipes must be tuned for different polymer grades and types, and neither approach can entirely prevent deformation of channel geometries. Furthermore, solvents can embrittle thermoplastics and result in microcracking, particularly for microfluidic systems which require exposure to high or cyclical pressure loads. Because of these challenges, there remains a need for effective methods for low temperature thermoplastic bonding which are amenable to a wide range of microfluidic applications.

The difficulty in realizing high bond strengths for polymer microfluidic chips is in large part due to the low surface energies of thermoplastics. Thermoplastic polymers, including PMMA and COC, are formed from hydrocarbons with additional atomic components such as oxygen and nitrogen. These surfaces possess low specific energy and thus tend to be hydrophobic or weakly hydrophilic, limiting the strength of bonds which may be formed between mating substrates. Increased surface energy serves to improve the wettability between the mating surfaces through enhanced mechanical interlocking and interdiffusion of chains. Bonding can also be enhanced through the generation of electrostatic interactions, and surfaces possessing high

specific energy in the form of polar functional groups which can produce hydrogen or covalent bonds across the interface are capable of providing bond strengths exceeding that of the bulk polymer.[64]

A variety of approaches for increasing the surface energy of polymers have been demonstrated and are routinely used in macroscale polymer engineering, including solvent or acid treatments,[65] surface grafting,[66, 67] and vacuum[68, 69] and atmospheric[70] plasmas. It is well known that energetic ions, electrons, and UV photons in plasmas can possess sufficient energy to break chemical bonds on the target surface, producing highly reactive free radicals which can help to form the desired charged surface groups and increase the overall surface energy. Plasma activation has been widely used to prepare hydrophilic polymer microfluidic substrates based on elastomeric materials such as PDMS,[70] and rigid thermoplastics including both PMMA[71, 72] and COC.[72-74] Direct exposure of PMMA to UV without ozone generation has also been explored for photochemically patterning energetic surface groups.[75]

3.1 UV/Ozone Treatment

Low temperature bonding of microstructured PMMA and COC surfaces was recently reported using O_2 plasma activation.[76] In this dissertation, UV/O_3 surface treatment is evaluated as an alternative approach to achieving high bond strengths in polymer microfluidics at low process temperatures. UV/O_3 treatment is a technique initially developed for the removal of organic contaminants from semiconductor substrates which was explored for depolymerization of photoresists in 1972[77] and

41

further developed over the following decade as an alternative to oxygen plasma ashing.[78-80] Using a low-pressure mercury lamp to expose a substrate in an air-filled chamber at atmospheric pressure, light output at a wavelength of 184.9 nm is absorbed by oxygen in the air, resulting in the generation of ozone. At the same time, the mercury tube's output at 253.7 nm is absorbed by the ozone, leading to dissociation of the ozone molecules. As ozone is being continually generated and disassociated, a steady-state concentration of atomic oxygen develops within the chamber, where it acts as a strong oxidizing agent. Hydrocarbons on the substrate surface are rapidly oxidized, and the reactivity is enhanced by the fact that most hydrocarbons also absorb the 253.7 nm radiation from the UV source. This approach has previously been shown to be effective in removing organic contaminants from a number of substrate materials including silicon, silicon nitride, glass, quartz, metals, and various polymers.[80]

At sufficiently high energy levels, UV/O$_3$ exposure can break polymer chains and insert oxygen-containing functional groups into the surface.[81] The oxidation results a more energetic surface, thereby increasing hydrophilicity and enhancing wettability. For application to polymer microfluidics, the higher wettability can lead to improved low temperature bond strength between mating polymer surfaces. Unlike vacuum plasma treatment, UV/O$_3$ treatment is a high-throughput and low-cost process which can be performed using commercially-available systems originally designed for semiconductor substrate cleaning. UV/O$_3$ treatment provides the further benefit of removing unwanted organic contaminants from the polymer surface, thereby simplifying substrate handling requirements prior to exposure.

This dissertation evaluates the utility of UV/O$_3$ surface treatment as a method for effective low temperature polymer microfluidic substrate bonding. Relationships between UV dose and surface hydrophilicity and bond strength are reported. To evaluate the post-bonding effects of UV/O$_3$ treatment on microfluidic device performance, the oxidized surface chemistry is evaluated, and stability of surface charge following exposure to common solvent conditions is measured. The effect UV/O$_3$ treatment on electroosmotic flow is also considered.

3.2 Experimental

3.2.1 Chip Preparation and Bonding

Microfluidic substrates were prepared from 2.0 mm thick COC (Zeonor 1020 R, Zeon Chemicals L.P., Louisville, KY) and 1.6 mm thick PMMA (Optix Acrylic Sheet, Plaskolite Inc., Columbus, OH). The thickness of the COC plates was reduced from 2 mm to 1.6 mm by placing a 1.6mm gauge block between two optically smooth glass plates in a commercial hot press (AutoFour/15, Carver, Wabash, IN), with the platen heated to 120 $^{\circ}$C at a pressure of 6.9 MPa for 1 hour. Goniometer measurements performed on COC substrates before and after thickness reduction revealed no statistically meaningful change in contact angle resulting from this process.

UV/O$_3$ exposure was performed using a commercial ozone cleaning system (PSD-UV, Novascan Technologies, Ames, IA). Manufacturer specifications for the 50 W system state that approximately 50% of the total lamp output power is delivered

around the 254 nm peak, and 5% around the 185 nm peak. Assuming the total 50 W power is evenly distributed over a 15 cm diameter circle corresponding to the maximum substrate size supported by the tool, a rough estimate of output powers used in this study are 14 mW/cm^2 at 254 nm, and 1.4 mW/cm^2 at 185 nm.

Polymer test samples were cut into 2.5 cm square pieces by CNC milling. Contact angles before and after treatments were measured using an optical goniometer (Cam Plus Micro, Tantec Inc., Schaumburg, IL). Surface elemental analysis employed an x-ray photoelectron spectrometer (Axis 165, Kratos Analytical Inc, Chestnut Ridge, New York).

Bonding of the polymer chips was performed using a hot press with a 150 kN load capacity (AutoFour/15, Carver, Wabash, IN). Platen parallelity was checked prior to bonding to ensure uniform force distribution. The COC and PMMA samples were rinsed with 2-propanol (IPA) and DI water, dried with N$_2$, and dehydrated in a vacuum oven at 85 ^{o}C for 2 hr. The platen were preheated to the desired bonding temperature, followed by application of a fixed pressure of 4.8 MPa for 10 min. Bonding temperatures were monitored using a thermocouple inserted into a custom aluminum chip holder.

3.2.2 PVA Preparation and Coating

Polyvinyl alcohol (PVA) solution was prepared by mixing 2 g of 99+% hydrolyzed PVA powder (Sigma-Aldrich, St. Louis, MO) into 100 mL of >18 MΩ DI water. For contact angle measurements, substrates were dipped into the PVA solution for 10 min at room temperature, then removed from the solution and incubated for 10

min at 95 $^{\circ}$C. The dip/incubation cycle was repeated 3 times. After final incubation, the substrates were rinsed with DI water and gently dried using an N_2 gun. For measurements of electroosmotic flow (EOF), PVA solution was introduced into the microchannels using a syringe pump, flushed with N_2 after 10 min, and incubated at 95 $^{\circ}$C for 20 min. The fill/flush/incubate process was repeated twice. Control experiments were performed using an identical process but without UV/O$_3$ treatment.

3.2.3 EOF Measurements

A solution of tris-borate (TB) Buffer (100 mM Tris, 20 mM boric acid, pH 9.1) was prepared and introduced into microchannels fabricated by hot embossing from a silicon template fabricated by deep reactive-ion etching (DRIE). All channels used for EOF measurements were 100 μm wide, 69 μm height, and 4 cm long. Measurements of electroosmotic mobility were performed using a current monitoring method.[82, 83] After flushing a microchannel with DI water and filling with the initial TB buffer, a voltage of 550 V was applied to one reservoir, with the second reservoir grounded. Voltages were applied using platinum wires placed within the open on-chip reservoirs, and current was directly monitored using a current meter at the grounded reservoir. After an initial current stabilization period of 1-2 min, the voltage was turned off and buffer solution was removed from the high voltage reservoir using a pipette and replaced with a new solution of TB buffer containing 10 mM boric acid. The voltage was then re-applied, and current through the microchannel was monitored as EOF displaced with initial buffer with the lower conductivity solution.

3.3 Results and Discussion

The application of UV/O$_3$ surface treatments for low temperature bonding of PMMA and COC substrates is evaluated here. In general, it is observed that UV/O$_3$ treated surfaces enable moderate bond strengths even at room temperature, and at higher temperatures produce bond strengths which rival native polymers bonded above their respective glass transition temperatures. Despite the potential benefits of UV/O$_3$ treatment for low temperature microfluidic substrate bonding, UV/O$_3$ exposure affects surface chemistry and can potentially alter the performance of microfluidic systems. To address this issue, surface stability and electroosmotic flow performance are also considered in the following.

3.3.1 Contact Angle

The maximum bond strength which may be realized between two mating surfaces is a function of surface wettability. Surface contact angles were evaluated as a function of UV/O$_3$ exposure prior to performing direct bond strength measurements. The native PMMA substrates used in this study exhibited an average contact angle of 80.3 ± 1.0^o. This value is slightly higher than previously reported values of 75 ± 2° [84] and 76 ± 4° [59]. The native COC substrates were also weakly hydrophobic with an average contact angle of 94.7 ± 1.0^o. A series of PMMA and COC chips were treated by UV/O$_3$ in 4 min increments. Following treatment of all samples, the sessile water contact angle for each sample was measured, with the results provided in Figure 3.1 (solid lines). The contact angle for PMMA dropped nearly linearly for the first 20 min of UV/O$_3$ exposure. In contrast, the contact angle for the COC substrates

dropped rapidly during the first 4 min of treatment, but showed little change during the following 20 min treatment time. Minimum contact angles of 25.3° and 49.3° were achieved following 24 min exposure for PMMA and COC, respectively.

Two samples of treated PMMA and COC exposed for 4 min and 24 min were stored in ambient atmosphere for 15 days, after which contact angles were measured again. No measurable change in contact angle was observed for any of the samples. Furthermore, treated PMMA and COC chips heated to 90 °C for 1 hr exhibited no measurable change in average contact angle. This result provides confidence that treated chips bonded at elevated temperatures, but remaining below glass transition, can retain their hydrophilicity during the bonding process.

Contact angles were also evaluated with the addition of a polyvinyl alcohol (PVA) coating step following UV/O_3 treatment. PVA is a hydrophilic charge-neutral polymer often used for reducing protein adsorption in silica capillaries[85] by either dynamic or a static coating.[86] The motivation for considering PVA is discussed in more detail in the following section on electroosmotic flow characterization. To determine whether PVA coating could further increase the hydrophilicity of the UV/O_3 treated PMMA and COC substrates, a series of samples were treated for varying times and coated with PVA. The resulting contact angles are also shown in Figure 3.1 (dashed lines). The use of PVA coating on the PMMA surfaces was found to provide a consistent improvement in hydrophilicity, with an average decrease in contact angle of 27% over all exposure times. For the COC substrates, PVA coating reduced the contact angle by 21% for the 4 min treated sample, but no improvement was observed for exposure times beyond 12 min.
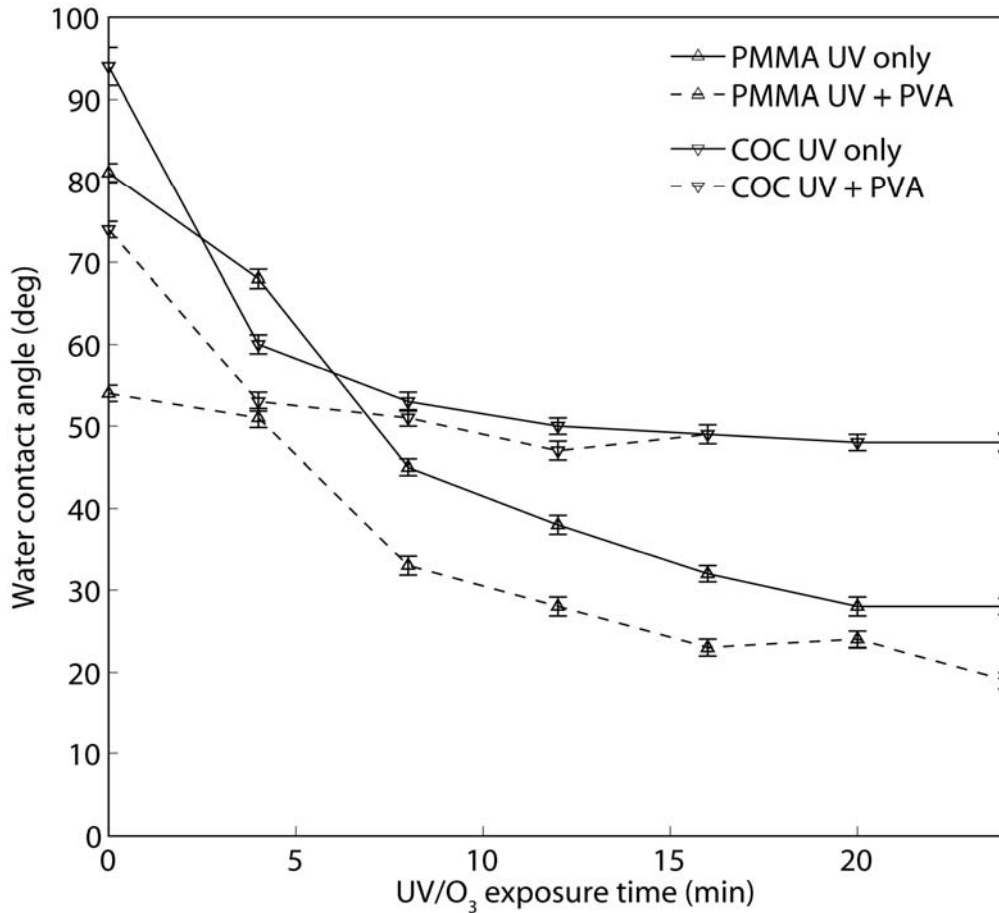
Figure 3.1: Water contact angle for PMMA and COC substrates after UV/O₃ treatment, and UV/O₃ treatment followed by PVA coating.

3.3.2 Bond Strength

To evaluate the improvement in bond strength for the treated substrates, a set of PMMA and COC chips were exposed in the UV/O₃ system for 24 min. Bonding was performed at temperatures between 25 ^{o}C and 110 ^{o}C for both UV/O₃ treated and untreated chips. Bond strength for the bonded chips was determined using a crack-opening method,[87] in which a blade of known thickness is inserted between the

bonded substrates, and the length of the interfacial fracture crack measured to evaluate the bond strength. The relationship between crack opening length, L, and interfacial surface energy (bond strength), γ, is given by, [87]

$$\gamma = \frac{3Et_s^3 t_b^2}{32L^4} \tag{1}$$

where E is the elastic modulus of the substrate, t_s and t_b are the thickness of substrate and inserted blade, respectively, and L is the measured crack length generated by the inserted blade. Using elastic moduli for PMMA and COC of 3.3 GPa[45] and 2.1 Gpa,[46] respectively, the resulting bond strengths calculated from Eqn. (1) are plotted against bond temperature in Figure 3.2. All tests were performed using a stainless steel razor blade with a thickness of 100 μm, with crack lengths measured under a microscope using a calibrated reticle. Uncertainty in crack length measurements, estimated at 200 μm, was found to dominate the measurement variance, resulting in bond strength uncertainties of 14% for PMMA and 10% for COC.

For native untreated chips, the relationship between bond temperature and bond strength follows a similar trend for both PMMA and COC. Below 90 °C, no bonding was observed for untreated chips. At 90 °C, interfacial cracks propagated across the entire length of the 2.5 cm chips upon insertion of the blade, fully debonding the substrates during measurements. Note that the trend lines for native PMMA and COC in Figure 3.2 assume a bond strength value corresponding to the 2.5 cm crack length at 90 °C which is off the plot. Maximum bond strengths of 2.10 mJ/cm² for PMMA and 1.13 mJ/cm² for COC were achieved for the untreated chips at the highest tested bonding temperature of 110 °C. Because this bond temperature is substantially above

49

the glass transition temperature of both PMMA (98 ^{o}C) and COC (105 ^{o}C), these maximum values could not be achieved in real-world devices without substantially deforming or collapsing microchannels within the substrates, and are provided only for comparison to the bond strengths achieved at lower temperatures when using UV/O$_3$ treatment.
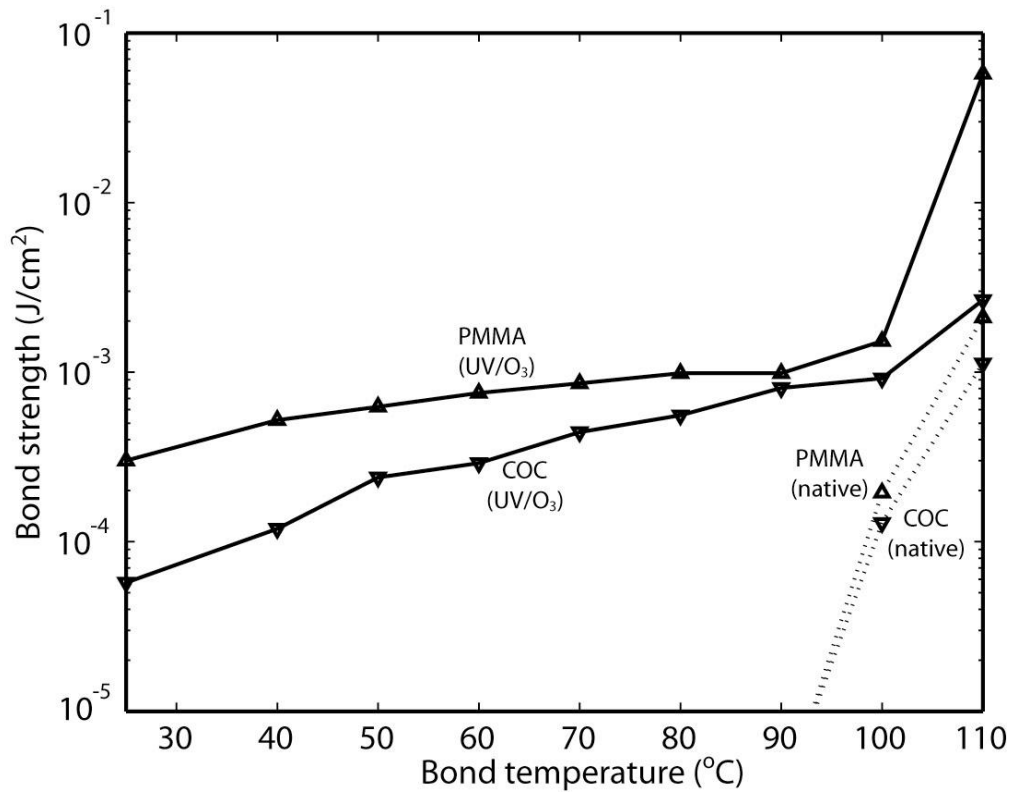
Figure 3.2: Bond strength of PMMA and COC substrates following 24 min UV treatment, compared with native polymer surfaces

Bond strength measurements performed on a set of UV/O$_3$ treated chips reveal substantial improvements in bond strength compared to the corresponding untreated cases. As shown in Figure 3.2, both polymers exhibit a logarithmic relationship

50

between bond temperature and bond strength over a wide temperature range from 25–90 ^{o}C. Large jumps in bond strength are observed as the bond temperature is elevated above the glass transition temperatures of the two materials. At 110 ^{o}C, the bond strengths of the UV/O$_3$ treated chips are significantly higher than that of the untreated chips bonded at the same temperature. A likely reason for this observation is that the higher wettability of the treated chips enables more intimate contact between the surfaces during thermal bonding, allowing improved interdiffusion of polymer chains and an attendant increase in bond strength. A summary of selected bond strength values is provided in Table 3.1. Even at room temperature, UV/O$_3$ surface activation provides sufficient bond strength for low pressure applications. At 90 ^{o}C, the UV/O$_3$ treated chips exhibit bond strengths at least 2 orders of magnitude higher than their untreated counterparts, and nearly as high as the maximum bond strengths achieved for substrates bonded above their glass transition temperatures.

			Bond Strength (mJ/cm^2)		
Material	Surface	25 ^{o}C	50 ^{o}C	90 ^{o}C	110 ^{o}C
PMMA	UV/O$_3$	0.301	0.624	0.984	57.26
	native	–	–	< 0.003	2.098
COC	UV/O$_3$	0.057	0.239	0.806	2.659
	native	–	–	< 0.003	1.128

Table 3.1: Summary of average bond strengths at selected bond temperatures.

It should be noted that bond strengths of 0.06 mJ/cm^2 at 25 ^{o}C and around 10 mJ/cm^2 at 50 ^{o}C have been reported for COC following optimized O$_2$ plasma activation, while low-temperature bonding of PMMA was found to be unaffected by plasma treatment.[76] Thus, in addition to the simplicity and cost advantages of UV/O$_3$ over plasma treatment for COC substrates, UV/O$_3$ treatment offers the

additional benefit of direct compatibility with low temperature bonding of PMMA microfluidic devices. Electron micrographs of a 500 μm wide and 180 μm deep PMMA microchannel bonded at 60 $^{\circ}$C following a 24 min UV/O$_3$ treatment is shown in Figure 3.3(a). Despite the extreme width of the channel, no deformation of the channel walls is evident. In contrast, the microchannel fabricated with the same initial dimensions and bonded at 100 $^{\circ}$C without surface treatment in Figure 3.3(b) suffers from severe wall deformation and channel collapse. Other than the surface treatment, both channels were bonded using identical parameters. As revealed from the bond strength plot (Figure 3.2), the treated chip bonded at only 60 $^{\circ}$C offers a higher bond strength than the untreated chip bonded slightly above its glass transition temperature. While even higher bond temperatures could improve bond strength for the untreated PMMA, the resulting channel deformation poses a substantial limitation on the range of channel geometries which can be successfully bonded without UV/O$_3$ surface modification.
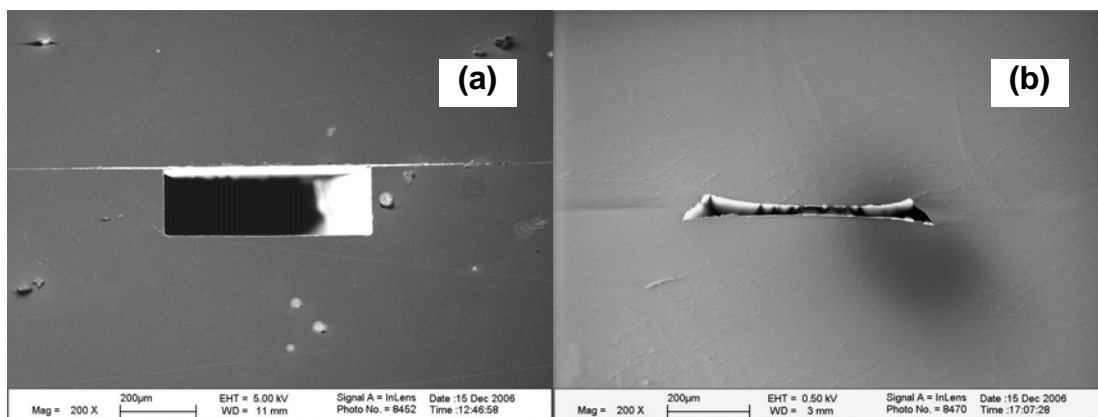
Figure 3.3: SEM images of 500 μm wide, 180 μm deep PMMA microchannels following (a) thermal bonding of 24 min UV/O$_3$ treated PMMA substrates at 60 $^{\circ}$C, and (b) thermal bonding of virgin PMMA substrates at 100 $^{\circ}$C

3.3.3 Surface Stability

While UV/O$_3$ treatment can enable low temperature bonding of thermoplastic substrates, the effects of UV/O$_3$ exposure on microchannel wall chemistry, and ultimately on device performance, must also be considered. For example, enhanced hydrophilicity can enable simple channel priming via surface tension driven wetting, while charged surface groups generated by UV/O$_3$ exposure may result in undesirable electrostatic interactions with analyte molecules and excessive or poorly controlled electroosmotic flow. Characterization of the oxidized surfaces is needed to understand whether desirable surface behavior can be retained, or undesirable behavior eliminated, after exposing the treated surfaces to various solutions.

It has been suggested that UV/O$_3$ hydrophilization of polymers may not be appropriate for applications where the surface is subjected to washing, since a substantial portion of the generated surface charge is due to low molecular weight oxidized material on the surface which can be lost by dissolution.[72] To explore this issue for PMMA and COC microfluidic substrates, chips exposed to a 24 min UV/O$_3$ dose were soaked in DI water (pH 7), acetic acid (pH 3), NaOH (pH 10), and 2-propanol (IPA). Individual sets of 3 chips for each case were submerged for 2 min in the respective solutions and dried under a gentle N$_2$ stream prior to sessile contact angle measurements. The resulting contact angles are shown in Figure 3.4. From this plot, it is interesting to note that despite the substantially lower contact angle for PMMA compared to COC following the initial UV/O$_3$ treatment, both materials reverted to around 55$^\text{o}$ after solvent exposure, with the acidic solution resulting in the lowest value, and IPA resulting in the highest value in each case. Longer soaking

times of 4 hours in all solutions did not noticeably alter the contact angles for either material. This result stands in contrast to previous work on PMMA surface modification using UV irradiation without the explicit generation of ozone, in which complete reversion of water contact angles was observed following IPA rinsing.[75] This result indicates that UV/O_3 treatment generates a more stable oxidized surface. Overall, the initial density of oxidized surface groups following UV/O_3 treatment can be reduced by solvent interactions, but with the final surfaces retaining a substantial degree of hydrophilicity even after long term exposure to a range of solvent conditions.
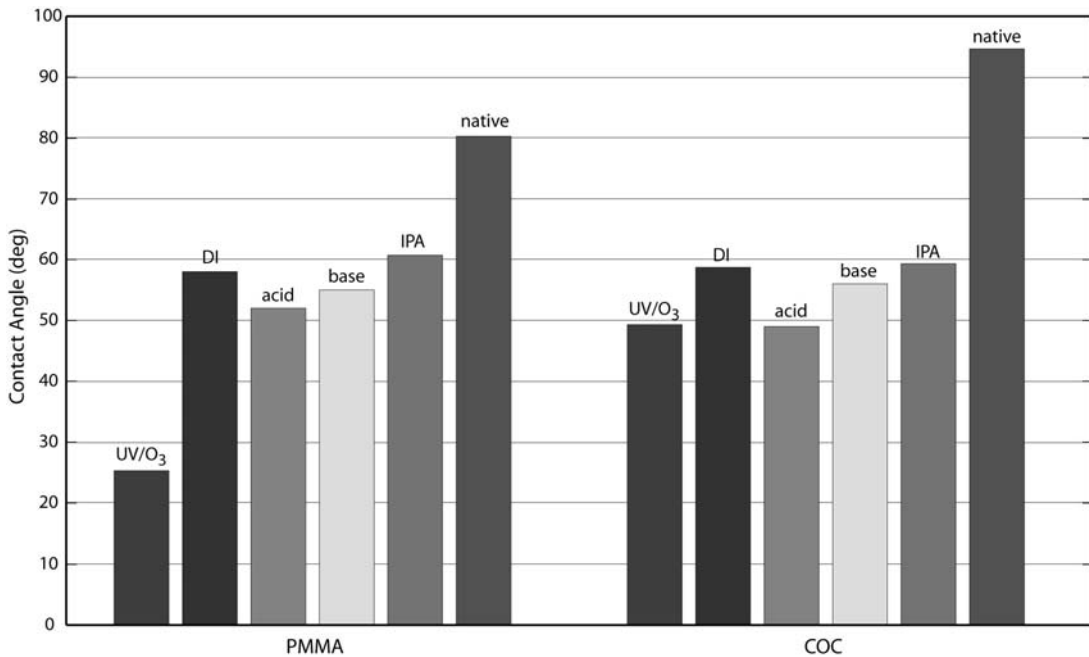
Figure 3.4 : Sessile water contact angle on PMMA and COC following UV/O_3 treatment only, and UV/O_3 treatment followed by 2 min soak in DI water (pH 7), acetic acid (pH 3), NaOH (pH 10), or IPA. Contact angles for native surfaces are shown for reference.

3.3.4 X-ray Photoelectron Spectroscopy (XPS) Analysis

During UV/O_3 exposure, the UV light at 253.7 nm generates free radicals on the polymer surface which further react with oxygen, resulting in oxygen-containing surface species such as carboxyl, hydroxyl, or peroxide groups.[75] Using X-ray photoelectron spectroscopy (XPS) to interrogate the atomic composition of the top polymer layer, the degree to which oxygen is introduced into the surfaces was evaluated following 24 min UV/O_3 treatments. Curve fitting of the raw XPS data was performed using Kratos Vision software to determine the relative atomic concentrations of surface C and O, with the results summarized in

Table 3.2. The 24 min UV/O_3 exposure was found to increase surface oxygen by 51% for PMMA and 205% for COC, indicating the generation of substantial oxygen-containing functional groups on the polymer surfaces. Treated chips rinsed in DI water for 4 hr were also measured to evaluate the degree to which charged surface groups are lost by dissolution.

Material	Surface	C 1s atom %	O 1s atom %	C / O ratio	O % Δ
PMMA	None	75.5	24.5	3.1	-
	UV/O_3	63.1	36.9	1.7	51
	UV/O_3 + DI	68.0	32.0	2.1	32
COC	None	94.5	5.5	17.3	-
	UV/O_3	83.2	16.8	5.0	205
	UV/O_3 + DI	81.7	18.3	4.5	233

Table 3.2: XPS analysis of elemental composition for PMMA and COC surfaces following different treatment conditions. Percent change in oxygen is measured relative to the untreated surfaces.

The XPS data suggest no loss of oxygen-containing species for COC, but a 37% decrease for PMMA. This trend is generally consistent with the observation

from Figure 3.4 that soaking treated COC does not significantly change the water contact angle, while 24 min treated PMMA surfaces exhibit a 36% lower contact angle than the same surfaces after a 4 hr DI soak.

3.3.5 Electroosmotic Flow Characterization

The observed reduction in hydrophilicity following solvent rinsing suggests a corresponding reduction in charged groups from the microchannel walls. Since zeta potential and electroosmotic mobility (μ_{eo}) are both functions of surface charge, UV/O_3 treatment is not suitable as a method to achieve strong and stable EOF in thermoplastic devices. However, for applications where EOF is not desirable, this is a positive result. To verify this prediction, measurements of μ_{eo} were performed at pH 9 in microchannels fabricated from native PMMA and COC, substrates treated with UV/O_3 for 10 min, and treated substrates which were then subjected to a DI water soak for 24 hours. As shown in Figure 3.5, the initial UV/O_3 treatment increases the average value of μ_{eo} by at least 50% for both materials due to the higher charge on the oxidized surface. However, after soaking the chip in DI water, the electroosmotic mobility is greatly reduced, returning to near the native value for PMMA, and below the native value for COC.
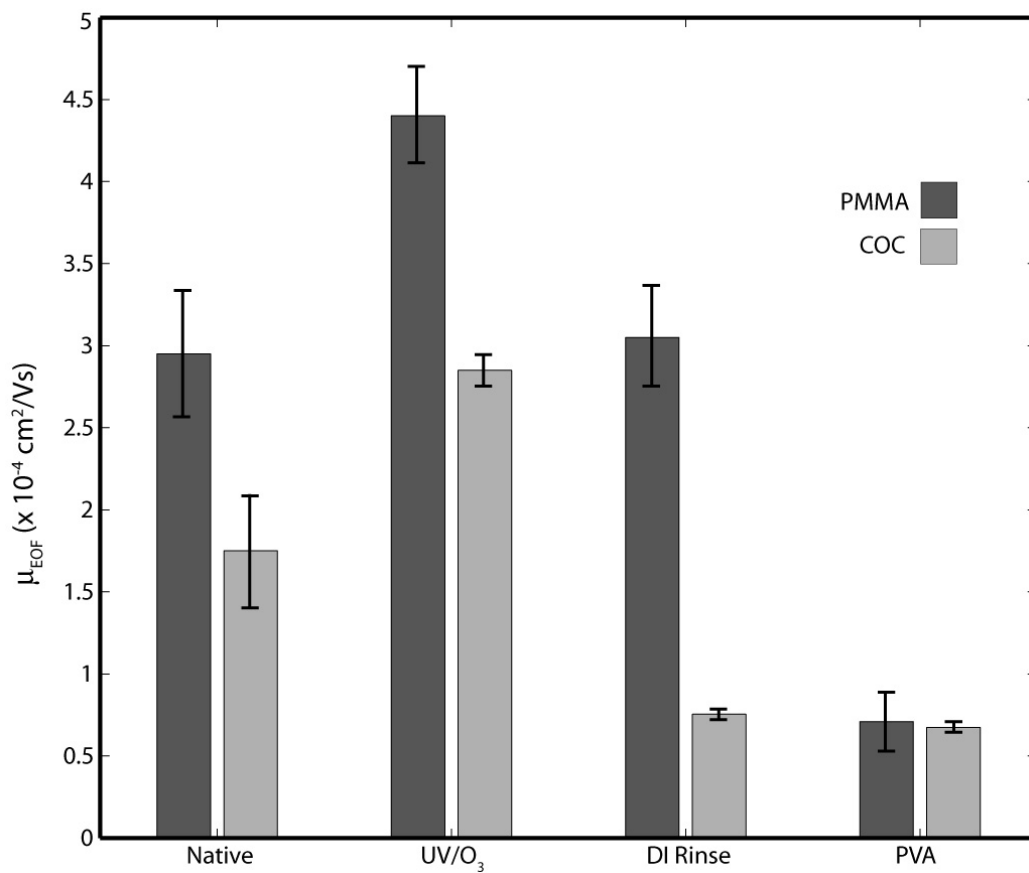
Figure 3.5: Electroosmotic mobility measurements at pH 9 for native PMMA and COC substrates, and the same substrates following a surface treatment sequence of 24 min UV/O$_3$ exposure, 2 min DI water rinsing, and PVA coating. Error bars indicate standard deviations among 3 replicate EOF measurements for each case.

While solvent rinsing can reduce the surface charge of UV/O$_3$ treated thermoplastics, it is also possible to take advantage of the unrinsed surfaces for further modifications. Unlike silica, which offers a native hydrophilic surface with well-characterized methods for its modification and derivitization, thermoplastics are generally non-polar and hydrophobic[88] and thus suffer from poor biocompatibility including nonspecific analyte adhesion due to hydrophobic interactions.[89] While UV/O$_3$ oxidation can produce hydrophilic polymer surfaces, the resulting charged groups on the microchannel walls can lead to electrostatic interactions with analyte

molecules, resulting in sample loss and peak dispersion during biomolecular separations in addition to the increased EOF demonstrated in Figure 3.5. As an additional test, μ_{EO} was measured for PMMA and COC chips treated with UV/O$_3$ for 10 min followed by bonding at 90 $^{\circ}$C and PVA coating. Shah et al. recently reported the use of PVA as a static coating for high-resolution DNA separations in PMMA microfluidics following an initial UV/O$_3$ surface treatment to improve PVA/wall interactions,[90] enabling the formation of a stable hydrophilic coating with low biomolecular adsorption, it can also substantially mask the polymer surface charge for reduced wall/analyte electrostatic interactions and electroosmotic flow. The measurements, also shown in Figure 3.5, support this observation, with electroosmotic mobilities of $\mu_{EO} < 8 \times 10^{-5}$ cm^2/Vs exhibited for both PMMA and COC following PVA coating. Control experiments using PVA-coated chips without UV/O$_3$ treatment exhibited virtually identical electroosmotic mobilities as the native polymers before PVA coating, further emphasizing the utility of UV/O$_3$ surface activation.

3.3.6 Optical Performance

Optical performance after UV/Ozone surface treatment was also evaluated on both COC and PMMA surface in this section. Polymer test samples were cut into 2.5 cm square, 1.6 mm thick pieces by CNC milling. UV/Ozone was treated in PMMA and COC exposed form 0 to 24 min with 4 min time increment. Surface spectroscopy was performed using a HP 8349 UV-visible spectrophotometer (Hewlett-Packard, Palo Alto, CA) and a fluorescence spectrophotometer (RF-5301, Shimadzu Scientific

Instruments, Columbia, MD). Changes in optical properties of the polymers are also observed, UV-visible transmission after UV/Ozone treatment of PMMA and COC substrates were shown in Figure 3.6 and Figure 3.7 respectively. Both PMMA and COC substrates exhibit high optical transmissivity around 85% 90% to in 400 nm ~700 nm visible spectrum range with or without UV/Ozone treatment. Variations in ultraviolet (UV) range (<400nm) have observed after UV/Ozone treatment. The PMMA surface optical transmissivity decreases with increasing UV/Ozone dose in <400nm spectrum range as shown in Figure 3.6 (b). Similar phenomenal have also observed in COC substrate as shown in Figure 3.7 (b), the optical transmissivity decreasing substantially from ~70% to ~10% in 290 nm~320 nm spectrum range and decreasing from 7% to 0.5% around 250nm range.
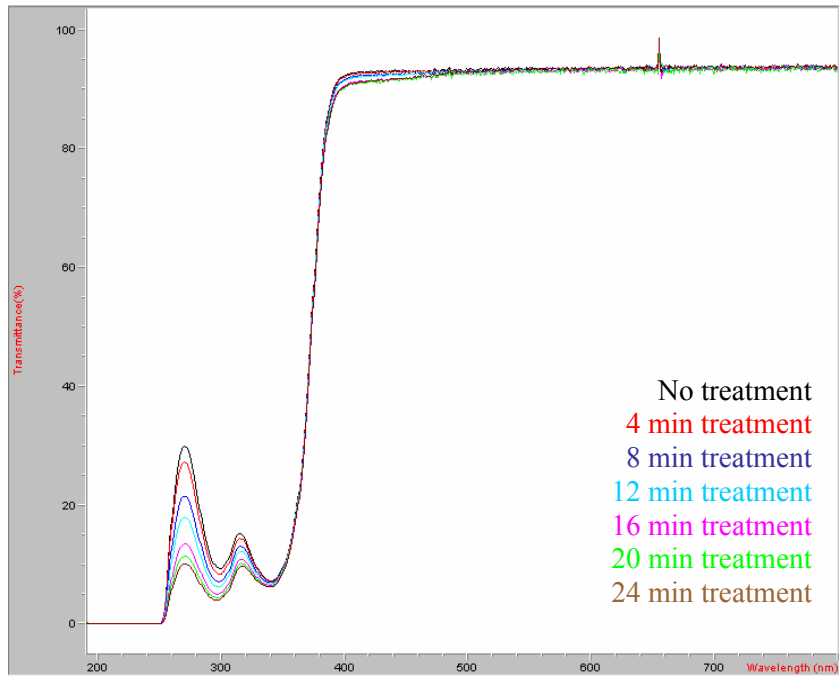
(a)
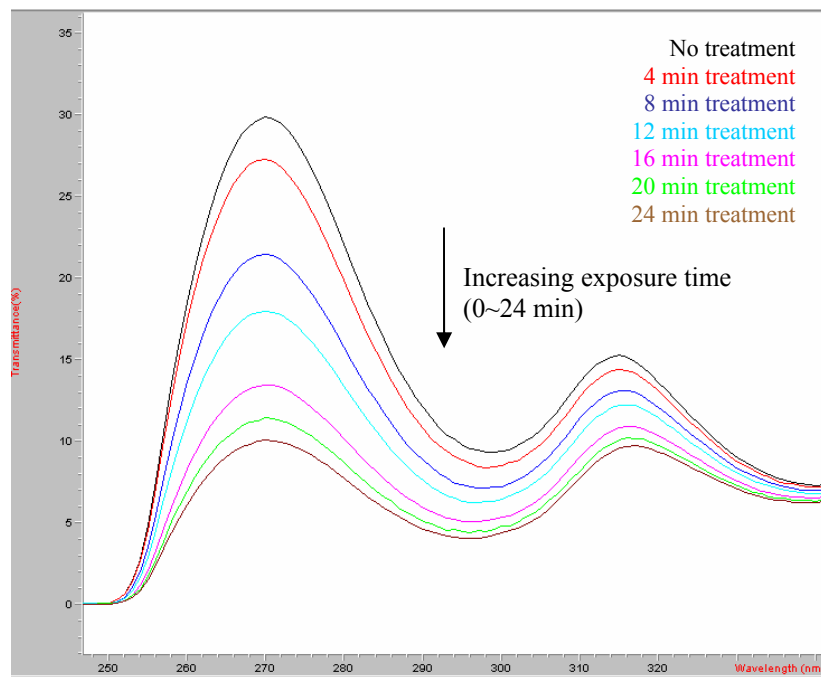
(b)

Figure 3.6: UV transmissivity effects from UV/Ozone treatment on PMMA substrate with optical wavelength in (a) 180 nm ~ 800 nm and (b) 180 nm ~ 340 nm range
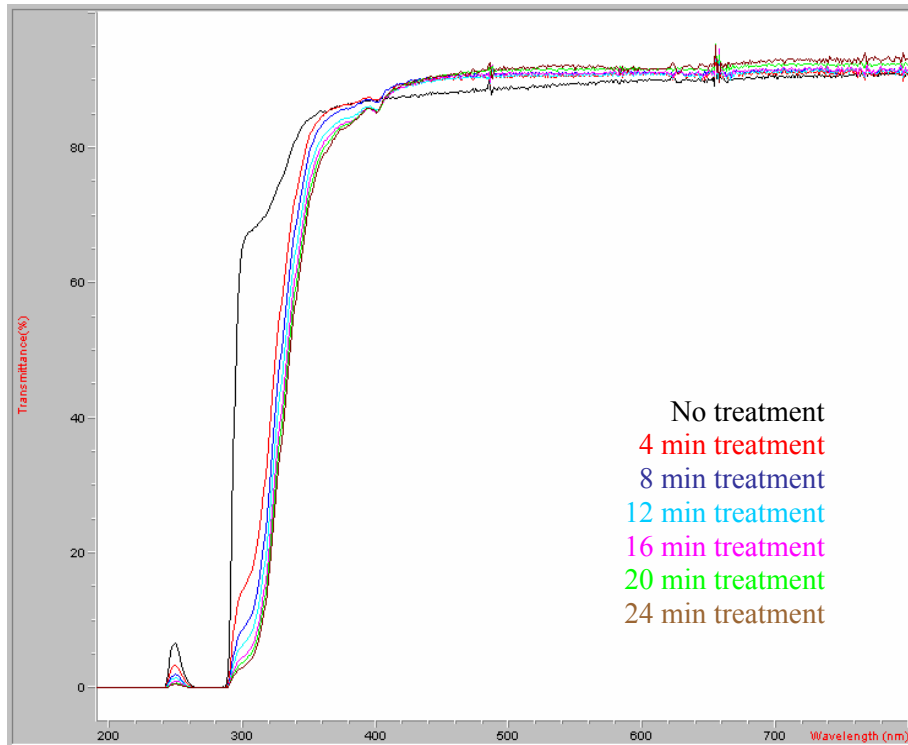
(a)
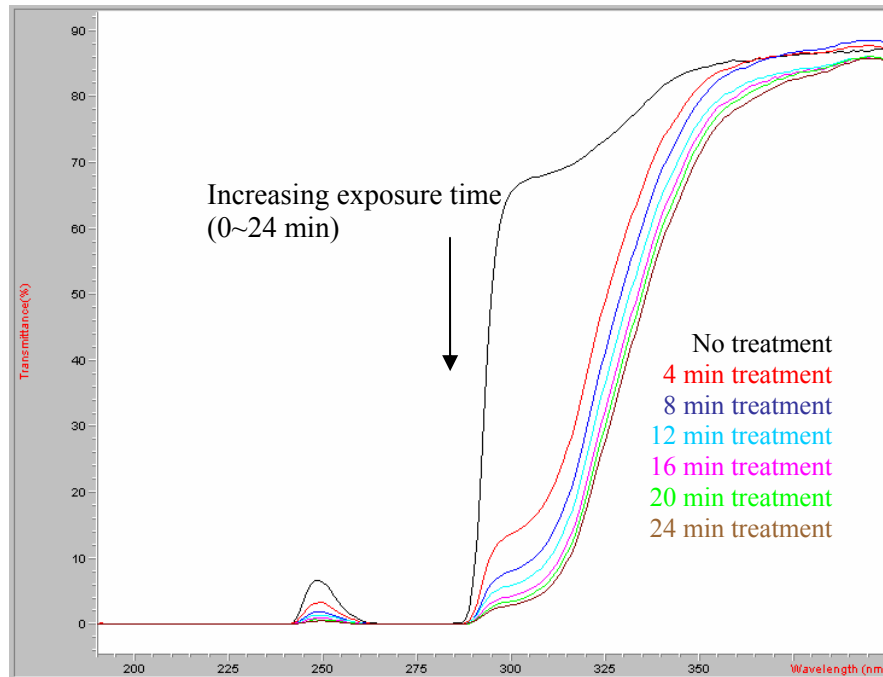
(b)

Figure 3.7: UV transmissivity effects from UV/Ozone treatment on COC substrate with optical wavelength in (a) 180 nm ~ 800 nm and (b) 180 nm ~ 400 nm
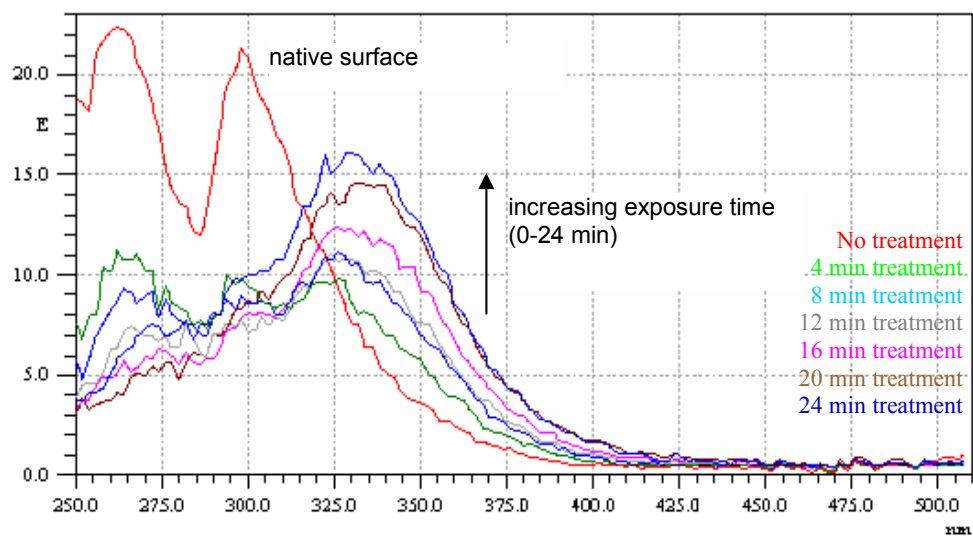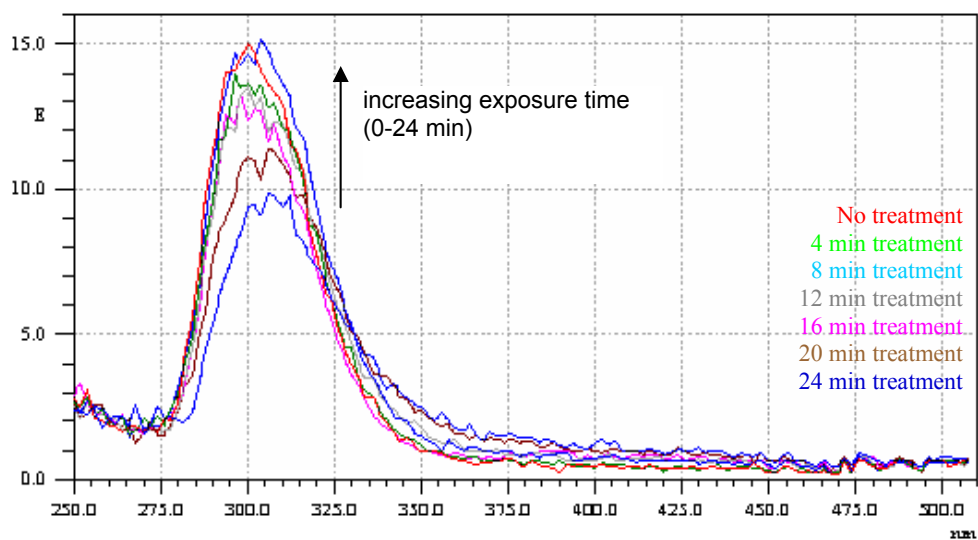
Figure 3.8: Autofluorescence spectra from 250-500 nm for (a) PMMA and (b) COC following UV-ozone exposure between 0-24 min.

3.4 Conclusion

The oxidation of PMMA and COC surfaces by UV/O_3 is a simple and effective method for low temperature bonding of thermoplastic microfluidic substrates. While surface oxidation based on O_2 plasma treatments has been previously described for enhanced low temperature bonding of microfluidic thermoplastic substrates, the UV/O_3 method reported here offers advantages including low equipment cost, low fabrication cost, and high throughput. In general, the energetic surfaces produced by UV/O_3 treatment resulted in at least 1–2 orders of magnitude improvement in bond strength for both PMMA and COC. High bond strengths were realized when sealing channels well below the materials' glass transition temperatures, while even room temperature bonding of UV/O_3 treated substrates resulted in bond strengths sufficient for typical sealing requirements in many microfluidic applications.
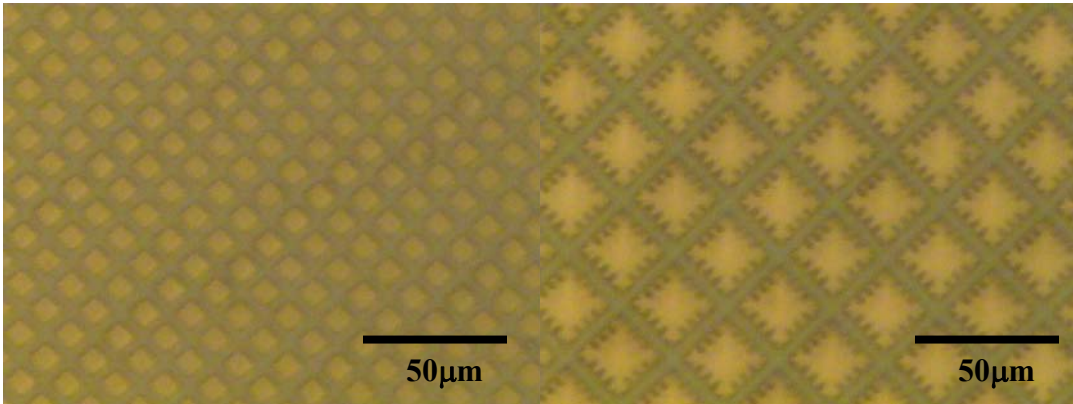
Figure 3.9: Micropillar with 5μm feature size bonded by UV/Ozone treatment

A high level of control over hydrophilicity was observed using UV/O$_3$ treatments, with resulting sessile water contact angles as low as 25° for PMMA surfaces. While the lowest contact angle observed with COC was only 49u, the resulting COC surfaces remained relatively stable compared to PMMA when exposed to solvents, with both materials exhibiting a similar range of final contact angle values in the order of 55°. Since practical microfluidic systems generally require exposure to aqueous or organic solutions, this value is of practical interest for applications in which UV/O$_3$ has been used for low temperature bonding during device fabrication. In addition to control of surface hydrophilicity for enhanced low-temperature substrate bonding, the generation of charged species by UV/O$_3$ treatment can also be used to enable the formation of stable secondary surface modifications in polymer microchannels, such as the application of static PVA coating demonstrated here. The UV/Ozone bonding technique is high repeatable, high yield bonding process. As shown in Figure 3.9, thousands of PMMA micropillars with feature size as small as 5μm can be bonded without microstructure damage by using this UV/Ozone bonding process.

Chapter 4 Nanofilament Silicon (nSi) Laser Desorption/Ionization Mass Spectrometry

4.1 Introduction

Following its introduction in the late 1980s,[34] laser desorption/ionization mass spectrometry (MALDI-MS) has emerged as a leading method for soft ionization of analyte molecules prior to mass determination, typically by time-of-flight MS. The technique has been widely used for a range of biopolymers, which are typically co-crystallized with a UV-absorbing organic matrix to enhance their ionization efficiency. However, MALDI-MS is well known to suffer from excessive matrix background signal for low molecular weight analytes, and thus its application has been limited to the study of relatively large biopolymers. Furthermore, MALDI-MS sensitivity is generally lower than electrospray ionization ESI-MS, with typical detection limits on the order of 1 femtomol,[29] although attomole range can achieved with using microstructured targets and optimized target preparation methods. [17, 28, 30]

In 1999, Siuzdak and co-workers reported the desorption/ionization on silicon (DIOS) technique,[37] in which an electrochemically-etched porous silicon (pSi) surface serves to efficiently absorb UV laser energy during LDI-MS analysis, allowing effective biomolecular measurements in the absence of organic matrix. As a result, matrix interference typically encountered below *ca*. 500 m/z in MALDI-MS is eliminated, allowing biomolecules within this range to be accessed by the DIOS-MS

technology.[34] In addition to small molecule analysis,[91] the technology has been applied to protein characterization.[92-94] Because the pSi targets can be readily functionalized, preferential binding of analytes based on affinity[95, 96] or hydrophobic[39] interactions has been demonstrated. The high sensitivity combined with good tolerance to contaminants also makes DIOS-MS an attractive platform for forensics applications.[97] Detailed reviews of the DIOS-MS technique, including background and applications, have been presented in recent review papers.[98, 99]

Nanostructured pSi surfaces developed for DIOS-MS are prepared by galvanostatic etching of silicon,[37, 100, 101] resulting in a surface consisting of nanoscale pores which exhibit a closed-cell morphology. For the analysis of biopolymers containing hydrophobic domains, such as peptides, silylation of the pSi surfaces using a reagent which presents fluorinated groups can serve to bind analyte molecules through hydrophobic interactions, allowing contaminants in the deposited sample to be removed from the pSi surface while retaining bound analyte molecules. Using this approach for peptide analysis, extremely low detection limits have been achieved by DIOS-MS.[39] Further improvements in detection limits are desirable for the analysis of limited samples or low-abundance species. In this context, a number of nanostructured surfaces have been recently explored as alternatives to pSi for matrix-free LDI-MS, including porous alumina.[102]

This dissertation investigates the use of dynamic electrowetting on nanofilament silicon (nSi) as an approach towards increasing the sensitivity of matrix-free LDI-MS. The nSi term is used as a convenient and descriptive notation to refer to surfaces which possess high aspect ratio silicon needles oriented parallel to one another and

normal to the plane of the substrate. The nSi surfaces employed in this work were produced using an metal-assisted oxidative etching process termed HOME-HF as first reported by Li and Bohn,[103] and later explored for the fabrication of LDI-MS target substrates.[104] By controlling the surface preparation and etching conditions, nSi surfaces exhibit dense fields of oriented nanofilaments, resulting in a high specific surface area and an open-cell morphology. This morphology differentiates the nSi surfaces from pSi, as their open-cell nature prevents the entrapment of air which could otherwise limit binding capacity by preventing effective interactions between deposited analyte and the full height of the nanofilaments. Another useful feature of nSi surfaces results is their superhydrophobic nature. Following the approach described by Trauger and co-workers,[39] the nSi chips are oxidized and silylated to produce a fluorinated surface suitable for peptide analysis. Due to the geometry and morphology of the nanofilaments, both as-fabricated and fluorinated nSi exhibits superhydrophobic behavior with large effective water contact angles. As a result, the contact area between the sample droplet and nanofilament surface remains small, preventing dispersion over the surface and allowing concentration of analyte as solvent within the droplet evaporates.

In addition to further evaluating nSi as a matrix-free LDI-MS substrate, the use of dynamic electrowetting on nSi is demonstrated as an effective method for improving LDI-MS detection limits. By applying a bias voltage between the sample droplet and superhydrophobic nSi surface, the nanofilament surface energy is increased, rendering the nSi surface hydrophilic and allowing sample to penetrate deep into the nanofilament matrix, resulting in increased peptide-surface interactions

and higher LDI-MS spectral intensities. Electrowetting on nSi is observed to be a dynamic process, with full wetting of the nanofilament surface occurring on the time scale of several tens of seconds. As a result, the method allows a sample droplet to wet the full depth of the nanofilaments while preventing the droplet from spreading beyond a contact area matched to the LDI-MS laser spot size of several hundred microns.

4.2 Experimental

4.2.1 Materials and Reagents

10 cm diameter p-type <100> silicon wafers with resistivity of 0.005-0.02 Ω cm (Customized Communication Inc., La Center, WA) were used as the substrates for all nSi chips. Ethyl alcohol was purchased from Pharmco-AAPER (Shelbyville, KY). 49% hydrofluoric acid (HF), 37% concentrated hydrochloric acid, 30% hydrogen peroxide, and urea were purchased from J.T.Baker (Phillipsburg NJ). Buffered oxide etchant (BOE) was purchased from Transene Company (Danvers, MA). Tris Base, HPLC grade water, methanol and acetonitrile were purchased from Fisher Scientific (Pittsburgh, PA). Lyophilized bovine serum albumin (BSA), 0.1% LC-MS grade trifluoroacetic acid (TFA) solution, DL-dithiothreitol and lyophilized des-Arg[9]-bradykinin were purchased form Sigma-Aldrich (St. Louis, MO). MassPREP DIOS target chips and lyophilized model peptides were purchased from Waters (Milford, MA). Mass spectrometry grade trypsin was purchased from Promega (Madison, WI). (Pentafluorophenyl)propyldimethylchlorosilane was purchased from Gelest

(Morrisville, PA). Conductive epoxy was purchased from Chemtronic (Kennesaw, GA).

4.2.2 Sample Preparation

Lyophilized peptide sample containing of 1 nmol of angiotensin fragment 1-7 (MW 898.7), RASG-1 (MW 1000.5), angiotensin II (MW 1045.5), bradykinin (MW 1059.6), angiotensin I (MW 1295.7), and renin substrate (MW 1758.0) were reconstituted with 0.1% aqueous TFA to an initial concentration of 1 pmol/μl. The peptide solution was diluted 10, 100 and 1,000 fold with HPLC grade water for final peptide concentrations of 100, 10, and 1 fmol/μl, respectively. Lyophilized des-Arg[9]-bradykinin (MW 904.0) sample was prepared by reconstituting in HPLC grade water at 0.11 μg/μl followed by subsequent serial dilution to aliquots of 1 pmol/μl, 10 fmol/μl, 100 amol/μl, and 1 amol/μl sample concentrations.

Trypsin is a serine protease that specifically cleaves at the carboxylic side of lysine (Lys) and arginine (Arg) residues. The distribution of Lys and Arg residues in proteins is such that trypsin digestion yields peptides of molecular weights that can be analyzed by mass spectrometry. The pattern of peptides obtained from mass spectrometry can be used for protein identification. For the preparation of tryptic digest, BSA was dissolved in a solution consisting of 8 M urea, 5 mM DL-dithiothreitol, and 50 mM Tris-HCl buffer (pH 8.2) to a concentration of 5 μg/μl. The solution was heated at 95 $^{\circ}$C for 20 min to denature the protein. After cooling to room temperature, 50 mM Tris-HCl buffer was added to decrease the concentration of urea to 0.5 M, and trypsin was added to a final enzyme:substrate ratio of 1:50 (w/w). The digestion was allowed to proceed at 37 $^{\circ}$C for 20 h. The digested BSA sample was

desalted using a C_{18} ZipTip pipette tip (Millipore, Billerica, MA) into a final acetonitrile / TFA (7:3 v/v) solution.

4.2.3 Nanofilament Substrate Preparation

Nanofilament substrates were fabricated by the HOME-HF etching process developed by Li and Bohn.[103] A 3 nm thick gold layer was deposited onto selected regions of a virgin silicon wafer by e-beam evaporation, using a shadow mask for pattern generation, followed by immersion into a solution of HF, H_2O_2, and EtOH (1:1:1 v/v/v) in a Teflon beaker for 32 s. Upon removal from the etchant, the substrate was immediately rinsed with methanol and blown dry in a gentle stream of N_2. The etched wafer was then oxidized by a 30 min UV/Ozone treatment (PSD-UV, Novascan Technologies, Ames, IA) to form a thin SiO_2 layer on the nanofilaments. The oxidized surface was fluorinated by dispensing 15 μl of (pentafluorophenyl)propyldimethylchlorosilane in a glass dish, and fixing the nSi substrate on a glass cover to seal the dish and allow the silylating reagent to coat the nanofilaments by evaporation. The vapor deposition process was performed at 65 °C for 15 min on a hot plate. The treated nanofilament substrate was rinsed with methanol and blown dry in a stream of N_2. The pSi substrates used for comparison were treated using the identical silylation procedure.

Morphological characterization of the resulting surfaces was performed using a field emission scanning electron microscope, Hitachi S-4700 FESEM (Hitachi High Technologies America Inc., Schaumburg, IL).

Safety consideration

HF is a hazardous acid which can result in serious tissue damage if burns are not properly treated. Etching of silicon should be conducted in a well ventilated fume hood with appropriate safety considerations including a chemical smock, face shield, and double layered nitrile gloves. Take care not to breath any HF fumes. Etching with HF should only be performed is calcium gluconate ointment is available for burn treatment. If contact with HF is suspected, remove contaminated clothing, flush vigorously with cold water, and massage calcium gluconate into the exposed area to neutralize the HF acid. Immediately seek physician care following any HF exposure.

Hydrogen peroxide is an exceptionally strong oxidizer which can cause severe eye, skin, and respiratory burns. As with HF, etching with hydrogen peroxide should only be performed in a well ventilated fume hood while wearing appropriate chemical safety protection.

4.2.4 Sample Deposition and Electrowetting

Sample deposition was performed using a 100 μm I.D. capillary (Upchurch Scientific, Oak Harbor, WA) connected to a syringe pump (PHD2000, Harvard apparatus, Holliston, MA) to generate a 150 nL sample droplet at the cleaved capillary tip. For deposition tests without electrowetting, the capillary tip was positioned to bring the droplet into contact with the nSi surface for 30 s, followed by removal of the capillary tip. When applying sample to the surface without electrowetting, no residual liquid was observed on the nSi chip after capillary removal.

For deposition tests employing electrowetting, the nanofilament substrate was first bonded to a stainless steel plate using conductive epoxy (Techni-Tool, Worcester, PA) and cured for 12 hr at room temperature. Prior to bonding, the native oxide layer on the backside of the silicon was removed by applying buffered oxide etchant with a cotton swab to ensure good electrical conductivity. The deposition capillary was connected with a platinum electrode through a capillary tee (Upchurch Scientific), and the electrode was connected to a DC power supply (E3612A, Agilent Technologies, Santa Clara, CA) to provide the desired electrowetting bias. A digit multimeter (34401A, Agilent) was used to monitor the electrowetting current. After bringing the 150 nL droplet into contact with the nSi target, the electrowetting bias was applied. After 30 s, the capillary was raised off the chip, depositing a sample spot approximately 0.5 mm in diameter on the nanofilament surface. The residual liquid was removed by blowing a stream of N_2 across the nSi surface.

All deposition experiments were performed under an optical goniometer instrument (Cam Plus Micro, Tantec Inc., Schaumburg, IL) for effective control of droplet delivery and to provide for real-time measurements of droplet contact angles.

4.2.5 LDI-MS Characterization

Mass spectrometry was performed using a Kratos Amixa MALDI-TOF instrument (Kratos Analytical, Manchester, UK). All LDI-MS spectra were recorded in the linear, positive ion mode and averaged over 25 to 50 laser pluses using a 337 nm nitrogen laser with a 3 ns pulse width. The effective laser spot size was estimated to be around 200 μm based on visual observation during experiments. Deposited sample

spot locations could not be readily visualized under standard illumination in the Kratos tool, and individual laser shots were used to determine sample spot locations by searching for maximum S/N. After locating a sample spot, laser energy was adjusted for maximum S/N prior to each test. Signal intensity and S/N were obtained by analyzing collected mass spectral data using Kompact software version 2.3.4 (Kratos Analytical).

4.3 Results and Discussion

4.3.1 Nanofilament Substrate Fabrication

Porous silicon produced by electrochemical etching process [37] is most widely used DIOS substrate for mass spectrometry application An alternative nanofilament Si substrate fabricated by etching a Si wafer coated with a sub-monolayer of metal layer in a $HF/H_2O_2/EtOH$ solution [103] was described in this dissertation. In this etching process, thin metal layer (<10nm) was first deposited onto bare silicon substrate Then the gold coated wafer was immersed into the in a $HF/H_2O_2/EtOH$ solution for 30 second. After immersion of the etching solution, the etched substrate was rinsed and dry. In addition, the patterning can be simply created by patterning gold during etching process, the color of metal-coated region change can observed visually from yellow to gray/brown then to black depending on the etching time. While the silicon surface without gold coating remains its native color, a clear patterning nanofilament substrate can be created.

Two types of metal, Au and Pt, to create nanofilament substrate have reported previously by Li and Bohn[103]. Figure 4.1(a) and (b) show SEM images of a Au-coated *p+* Si subjected to HOME-HF etching for 30 s. Large (~30 Nm) interconnected pores propagating anisotropically perpendicular to the surface. In contrast, in areas between the Au on the same wafer [Figure 4.1(b)], a much more compact structure with random arrays of small pores (~3 nm spaced by about 3 nm) can be seen. The etching depth is about 350 and 250 nm on and off the Au-coated areas, respectively. The area without Au-coated silicon morphology exhibits a dramatically smaller etch depth merely 10 nm deep. Figure 4.1(c) and (d) shows the SEM images on and off Pt-coated areas of a silicon subjected to HOME-HF etching for 30 s. A much rougher and deeper structure is produced on the Pt-coated sample than on Au-coated Si. In the Pt-coated area, shown in Figure 4.1(c), columnar structures are clustered together at the tip, and the etch depth exceeds 1 nm. The area without Pt coating shown in Figure 4.1(d) is very flat with small ~5 to 20 nm pores with 320 nm etch depth.
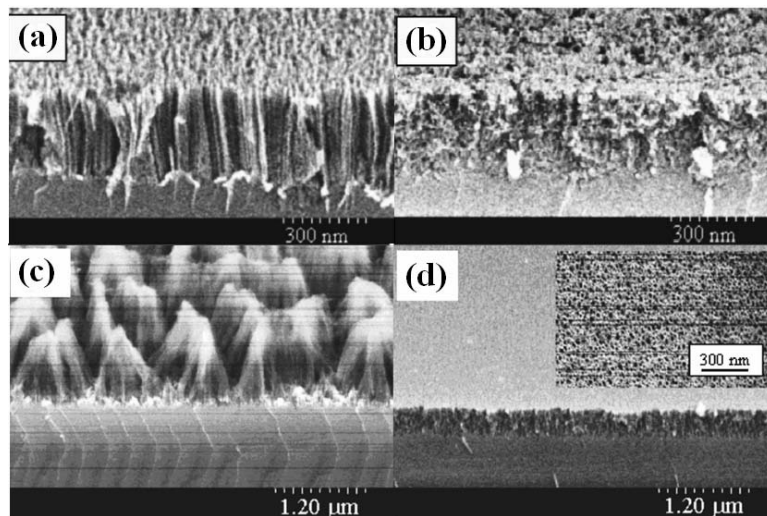
Figure 4.1: SEM images of Metal-assisted chemical etching porous silicon [103]

Silicon dissolution/pore formation mechanism

Porous silicon is formed by electrochemical etching of silicon surface in an aqueous HF solution. Partial dissolution and etching occur at the silicon surface through electrochemical reaction. The most accepted mechanism so far is proposed by Lehmann and Goesele in 1991[105] and the dissolution and etching mechanism of silicon is described as following shown in Figure 4.2. For porous formation, it is essential that electron holes are required. First, fluoride ion is attack on Si-H bonds and a Si-F bond is created. Another attack from a fluoride ion occurs due to the polarizing influence of the bonded fluoride with generation of H_2. The Si-Si back bond will attack by the HF and the remaining Si surface will bond to the H atoms with silicon tetrafluoride formation.
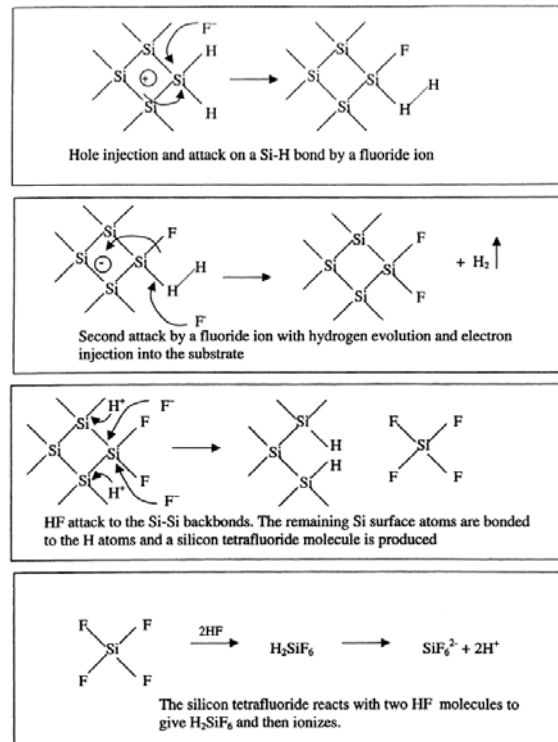
Figure 4.2: Silicon dissolution scheme [105]

Similar to electrochemical etching to create porous silicon, the metal-assisted etching acts as localized electrochemical etching process in which the nanoscale gold particle acts as cathode and silicon substrate acts as anode. The surface etching was done by local cell current effects on each gold particle site in HF/H$_2$O$_2$/EtOH solution without apply external bias throughout the etching process. The etching mechanism is illustrated below [103]:

Cathode reaction (as metal)

$$H_2O_2 + 2H^+ \rightarrow 2H_2O + 2h^+$$
$$2H^+ + 2e^- \rightarrow H_2$$
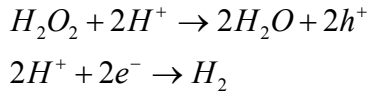
Anode reaction (as silicon surface)

$$Si + 4h^+ + 4HF \rightarrow SiF_4 + 4H^+$$
$$SiF_4 + 2HF \rightarrow H_2SiF_6$$
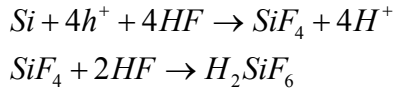
Overall reaction of HOME-HF etching process

$$Si + H_2O_2 + 6HF \rightarrow 2H_2O + H_2SiF_6 + H_2 \uparrow$$
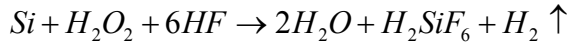
The metal-assisted HF/H$_2$O$_2$/EtOH etching process was found to provide a simple and reproducible technique for fabricating well-oriented silicon nanofilaments with excellent control over the final surface morphology. During the etching process, the color of the gold-coated silicon surface rapidly changes from yellow to brown, and finally to black after a sufficient etching time. Regions of the silicon surface without gold coating remain unaffected by the etchant. A typical nSi chip containing a 64-element array of 1 mm diameter with 2mm center-to-center spacing nanofilament pads is shown in Figure 4.3.
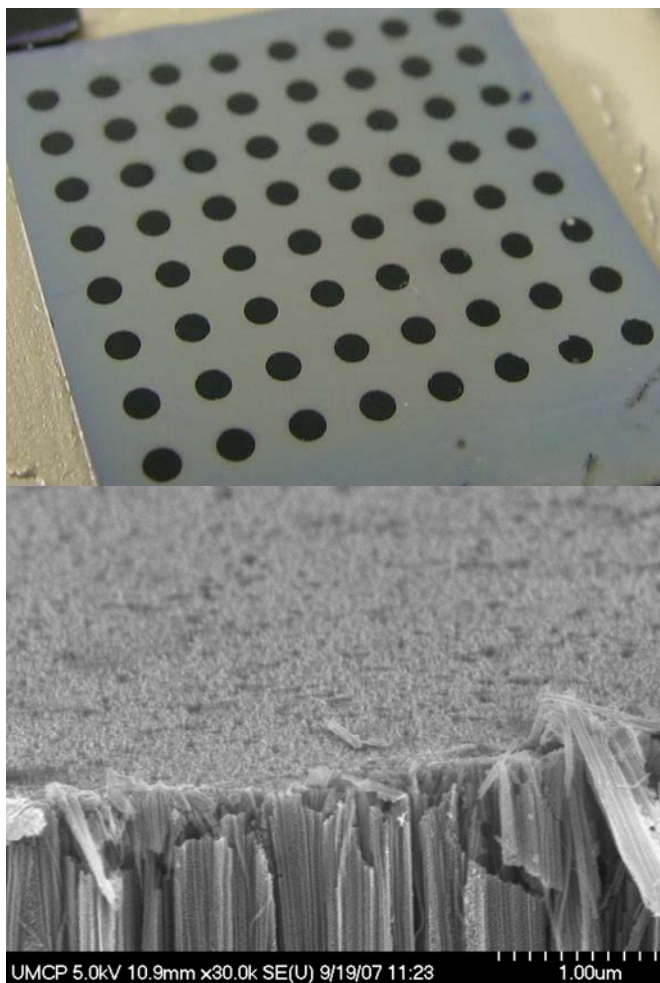
Figure 4.3: Patterned HOME-HF etched nanofilament substrate.

The morphology of the resulting nanofilaments can be seen from the electron micrographs in Figure 4.4(a). The nSi surface consists of individual nanofilaments 7-12 nm in diameter and 2.8 μm deep. Condensation of the nanofilament tips, presumably due to capillary forces during the post-etch drying process, results in the appearance of nanofilament "curtains" and a distribution of pore sizes with characteristic dimensions ranging from about 20-80 nm, with a smaller number of larger pores approaching 200 nm. Variations in nanofilament diameter, pore diameter, and pore distribution can be realized by altering the thickness of the initial gold film

prior to etching, while nanofilament height can be independently adjusted by varying the etch time. While not intended as an exhaustive evaluation, superior LDI-MS performance was observed for the particular nanofilament geometry and morphology depicted in Figure 4.4(a). In comparison, micrographs of a commercially-available pSi substrate are shown in Figure 4.4(b). It has been reported that smaller pSi pore sizes produce more intense ion signals, with optimal results realized for pore diameters between 70nm and 120 nm and pore depths around 200 nm.[37, 100] Similarly, ion signal from porous alumina has also been shown to increase as the pore dimensions are reduced to 100 nm, with 600 nm optimized thickness,[102] although smaller pores were not report due to fabrication challenges.
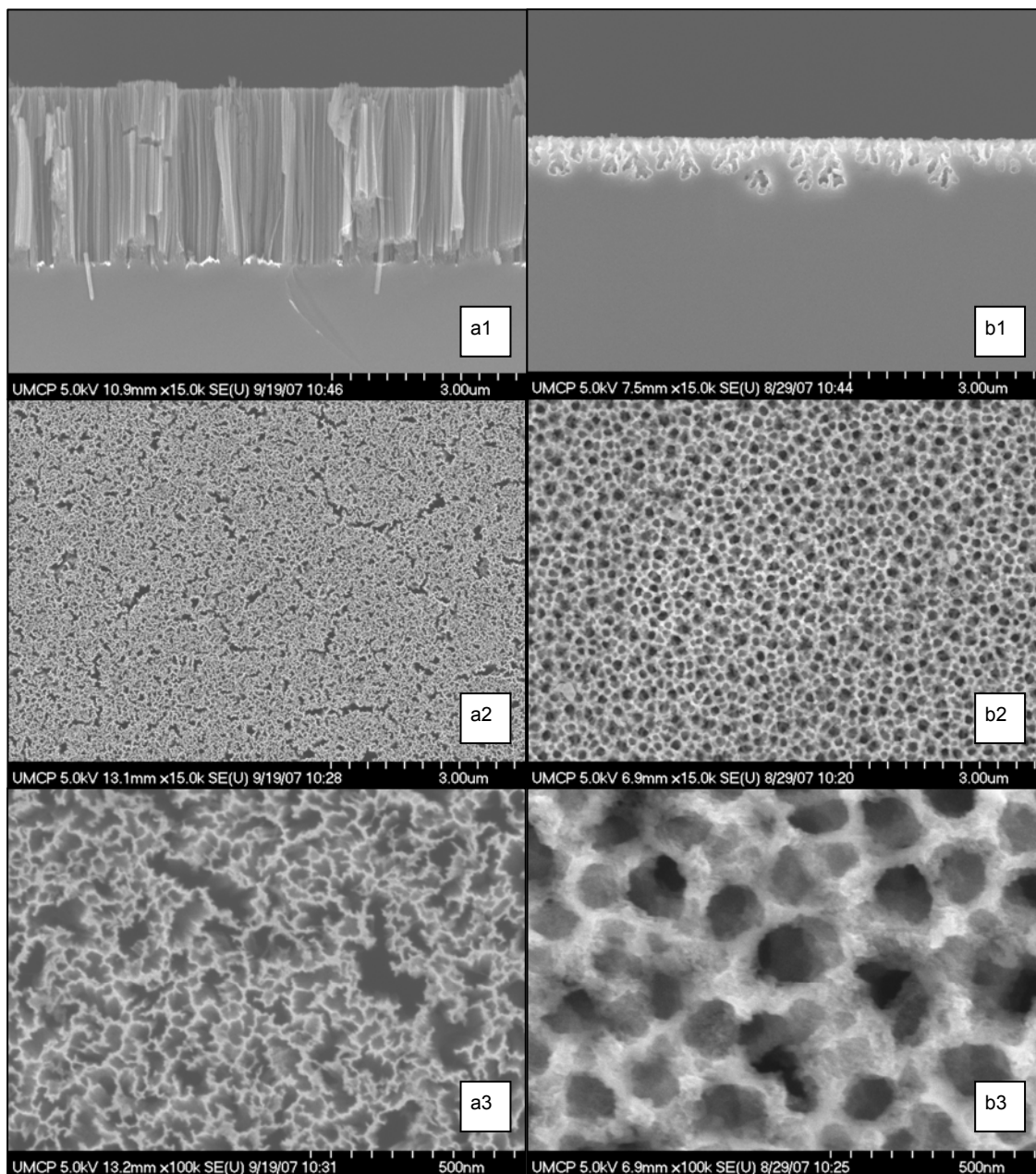
Figure 4.4: Electron micrographs of (a) fabricated nSi and (b) commercial pSi substrates

After etching, the hydrogen-terminated nSi surfaces are initially highly hydrophobic, but over time become increasingly hydrophilic as native oxide forms on the filaments. To avoid this, the chips were modified with

(pentafluorophenyl)propyldimethylchlorosilane after etching to generate fluorinated surfaces with superhydrophobic behavior. The hydrophobicity of a solid surface is related to both the chemical groups present on the surface and the micro- or nano-scale surface texture. It is well known that if a flat hydrophobic surface with a water contact angle of θ is given a suitable microtexture, an effective contact angle $\theta_o > \theta$ will be observed for water droplets placed on the textured surface. The effective contact angle can be described by the Cassie model,[106] which assumes that pockets of air remains in the pores beneath the droplet, so that the total interfacial free energy is a function of the fractional contact area ϕ between the liquid and the solid. Based on the Cassie model, the effective contact angle for a superhydrophobic surface is given by,

$$\cos\theta_o = -1 + \phi(1 + \cos\theta) \tag{1}$$

The fractional contact area of the nanofilament surface shown in Figure 4.3 was measured at $\phi = 58\%$, and goniometer measurements on the regions far from the nanofilaments present a nominal contact angle of $\theta = 82^{\circ}$, resulting in a predicted effective contact angle of $\theta_o = 109^{\circ}$. This value compares favorably with a measured effective contact angle of $\theta_o = 105^{\circ}$ for this particular chip. While nSi chips with lower values of ϕ were observed to result in substantially higher effective contact angles up to 148°, this increase occurs at the expense of surface area, potentially reducing the performance of these surfaces for matrix-free LDI-MS.

4.3.2 LDI-MS on nSi

The mechanisms of desorption and ionization on silicon surface are still under investigation. Thermal surface desorption might be one mechanism. Nanoscale structures are believed to enhance the sensitivity due to large accessible surface areas. The ionization mechanism of porous type silicon surface have been pervious reported by Vertex et al [107] for several possible approaches. During the ionization process, the porous silicon substrate absorbs the pulse laser energy and its temperature rises. The porous silicon surface temperature raises up to 600 K could lead to rapid evaporation. Electron transfer from the silicon surface and proton transfer from the excited Si-H groups to the analyte binding to the surface can result in ionization. Then, due to the electric fields applied from the time-of-light mass spectrometer, the ionized molecules are released from the silicon surface and separated in the drifting tube. At the end of the tube, the ionized molecules hit a detector and the drift time was converted into mass/charge ratio.

Comparison of laser desorption/ionization mass spectrometry analysis of peptide mixture between matrix-free nanofilament surface and conventional MALDI using CHCA matrix was shown in Figure 4.5. The m/z value on 1045.5 for angiotensin II, 1059.6 for bradykinin and 1295.7 for angiotensin I have observed on the DIOS-MS spectra using 15fmol peptide mixture shown in Figure 4.5(a). The mass spectra and mass intensity are also comparable to the conventional MALDI-MS as shown in Figure 4.5(b) using 125fmol peptide mixture. The nanofilament substrate also provides less noise level with over 4 times higher signal-to-noise (S/N) value compare to conventional MALDI-MS.
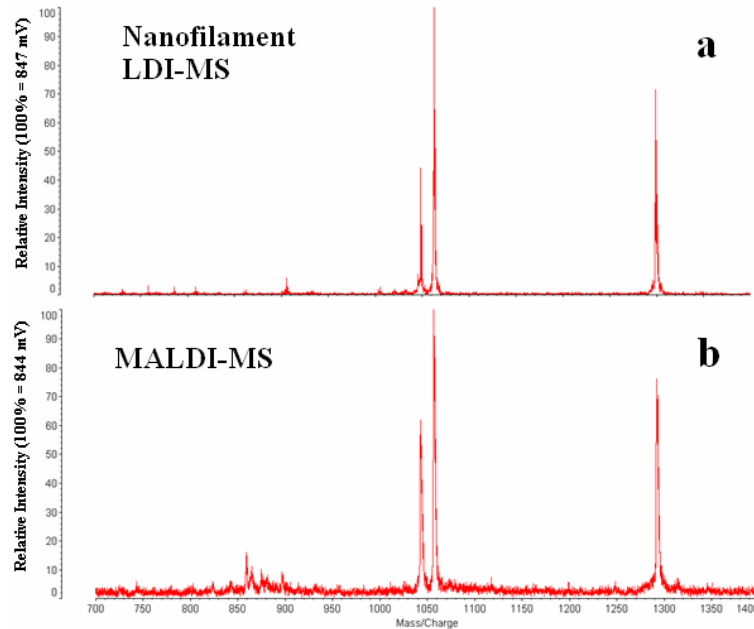
Figure 4.5: MS spectra of (a) LDI-MS and (b) CHCA MALDI-MS

Nanofilament silicon surface optimization

The performance of nanofilament substrate may vary with the filament pore size, thickness and morphology during fabrication process. This section presents a study of systematic variation of the parameters for the production of silicon nanofilament surfaces to optimize the LDI performance. Two main fabrication parameters to create nanofilament substrate, gold thickness and etching time have selected to evaluate the surface morphology, water contact angle and laser desorption/ionization mass spectrometry performance. Three different gold thickness, 10, 30 and 100 angstrom (Å) and two etching time 15 and 30 second are used to evaluate in this dissertation. Six different sets of nSi substrate are created from the factorial design as shown in Table 4.1.

Set #	I	II	III	IV	V	VI
Gold thickness	10 A	10 A	30 A	30 A	100 A	100 A
Etching time	15 sec	30 sec	15 sec	30 sec	15 sec	30 sec

Table 4.1: Factorial design of nanofilament silicon fabrication parameter

The 60 degree angle view of SEM images of filament substrate case I to VI were shown in the Figure 4.8. Three different gold thicknesses generate three different morphologies. The 10 Å gold thickness case (Set I and II) creates porous-like structure with pore size less than 10nm diameter. Each pore is isolated from each other propagating anisotropically perpendicular to the surface with ~0.5μm for 15sec etching time (Set I) and ~1.0 μm for 30sec etching time (Set II). For the 30 Å gold thickness case (Set III and IV), the HOME-HF etching creates filament-like structure with pore size around 10~50nm diameter. Each pore is interconnected to each other propagating anisotropically perpendicular to the surface with ~0.6μm for 15sec etching time (Set III) and ~1.5 μm for 30sec etching time (Set IV). The 100 Å gold thickness case (Set V and VI) creates needle-like structure. Each needle-like structure are separate to each other about 2 to 4 μm with ~1μm height for 15sec etching time (Set V) and separate to each other about 1 to 2 μm with ~3μm height for 30sec etching time (Set VI). The hydrophobicity of silicon surface of each test set was also evaluated. The water contact angle measured by optical goniometer of silylated (PFPPDMCS coating) and native silicon surface is shown in Figure 4.7 The silicon surface exhibits hydrophobic behavior around 110 degree water contact angle for Set I to V. Higher hydrophobicity around 125 degree has observed in 100 Å 30 gold thick with 30 second etching silicon surface (Set VI).
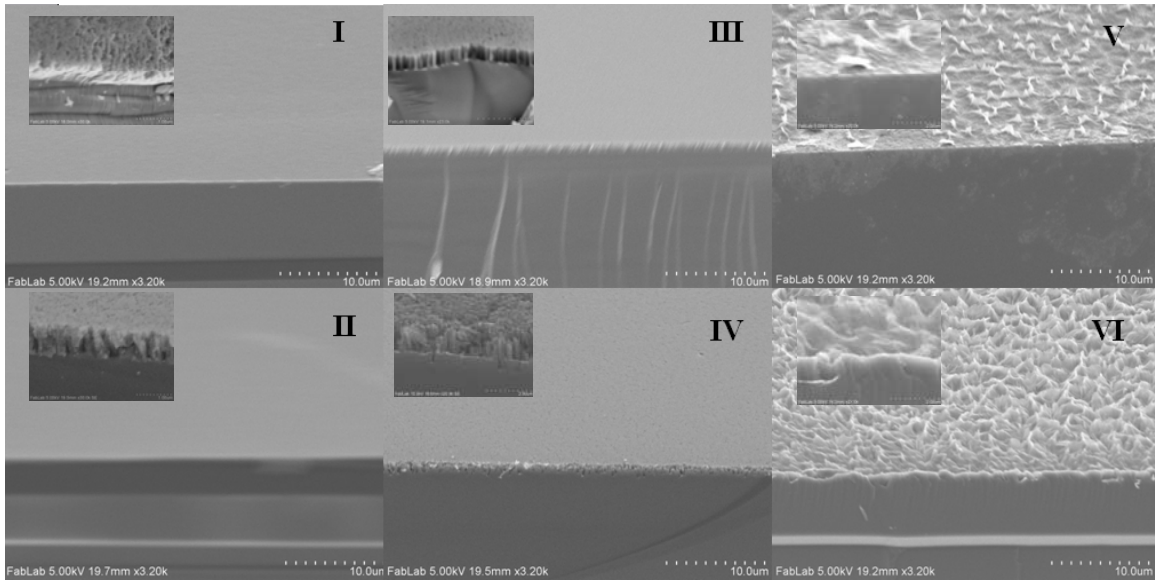
Figure 4.6: SEM images of nanofilament substrate with various etching time and gold thickness
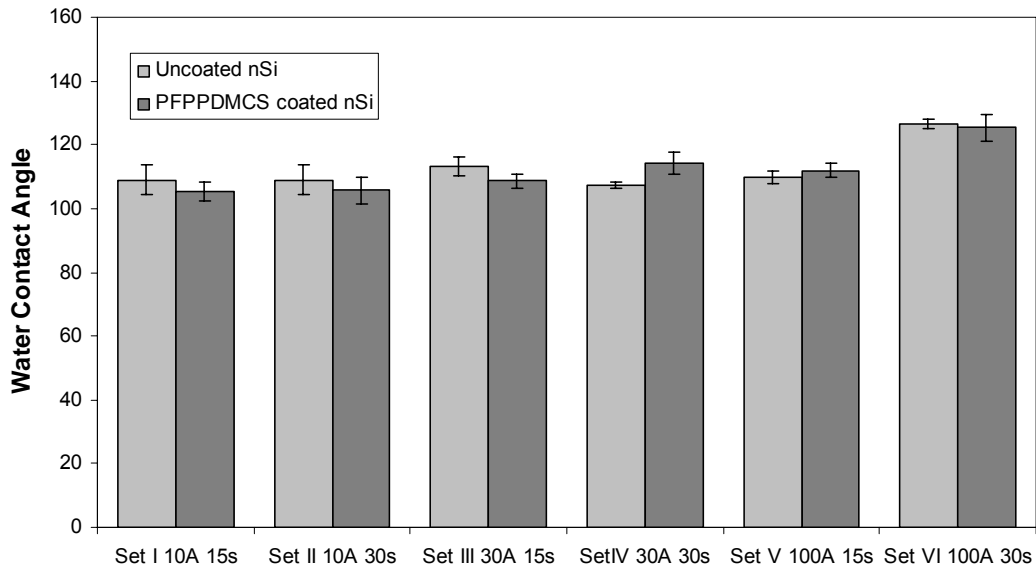
Figure 4.7: Water contact angle measurements on nanofilament substrate with various etching time and gold thickness

30-second contact spotting of 150nL 10fmol/ul Des-Arg^9-bradykinin (MW: 904.02) sample was deposited onto the Set I to VI silicon surfaces. The laser desorption/ionization mass spectrometry (LDI-MS) test mass spectra and signal intensity value of each silicon surface are shown in Figure 4.8. In the preliminary

optimization experiments, it was found that thick nanostructure height (30 second etching) exhibits better signal intensity than thinner silicon surface (15 second etching) under sample gold thickness. Among all, the 30Å gold with 30 second etching (Set IV) exhibits highest signal intensity. In addition, open cell filament-like nanostructure is more wettable for better sample penetration into the silicon pores for higher detection sensitivity. One approach using electrowetting deposition is discussed in the following section.
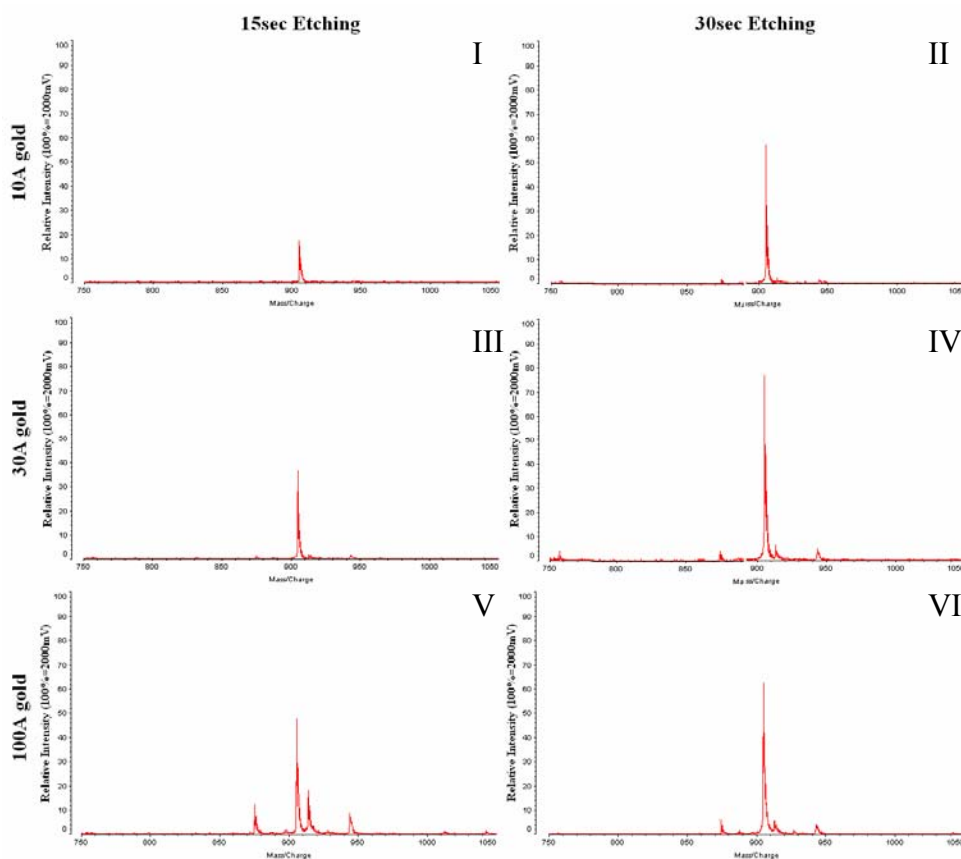
Figure 4.8: LDI-MS signal intensity on nanofilament substrate with various etching time and gold thickness

nSi LDI-MS performance evaluation

A dilution study using a single model peptide, des-Arg[9]-bradykinin, was performed following a report by Trauger and co-workers in which exceptionally high sensitivity was realized for this analyte using pSi DIOS-MS.[39] Sample deposition was performed using a 100 μm I.D. capillary to generate a 150 nL sample droplet at the cleaved capillary tip. The capillary tip was positioned to bring the droplet into contact with the nSi surface for 30 s, followed by removal of the capillary tip. Typical mass spectra using an optimized nSi chip are shown together with mass spectra acquired from the commercial pSi chip in Figure 4.9(a), and a comparison of average spectral intensities over 3 individual tests is shown in Figure 4.9(b) for nSi chips with different pore sizes in addition to commercial pSi. Noting that the MS detector was saturated for the 150 fmol nSi loading case, the nanofilament chips with 20-200 nm pore dimensions provide nearly double the ion intensity of the nSi surface with smaller pores, and 2-4 times the ion intensities of pSi. The former observation is consistent with nSi LDI-MS measurements performed by Kruse an co-workers,[108] which revealed lower ion generation efficiency for smaller pores around 3 nm. At the lowest loading level, 15 amol, S/N for the nSi target with 20-200 nm pores was larger than 100, suggesting a detection limit around 0.5 amol without electrowetting.
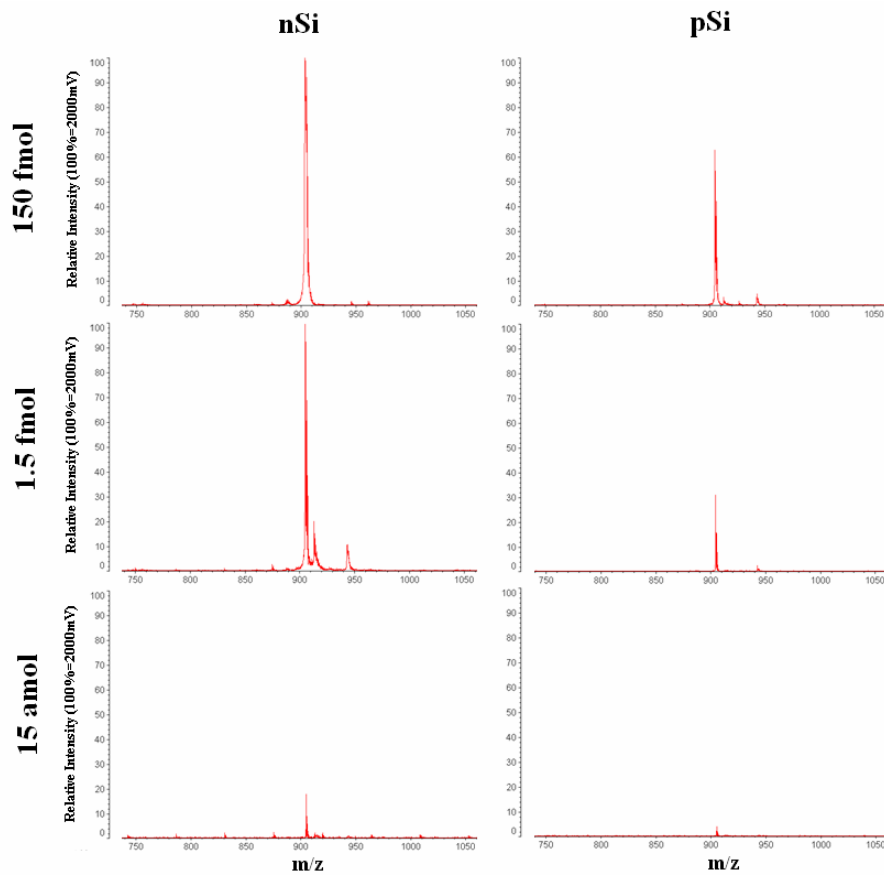
(a)
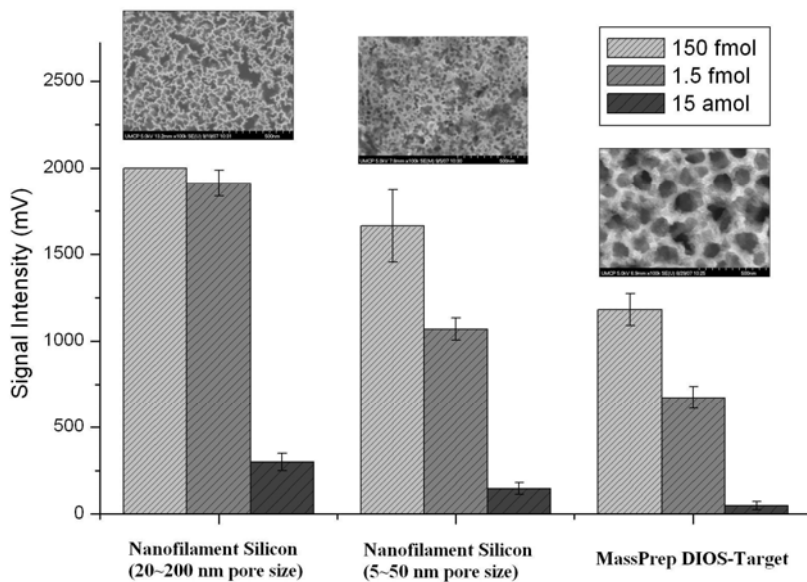
(b)

Figure 4.9: (a) LDI-MS spectra for des-arg[9]-bradykinin on nSi and pSi substrates, and (b) comparison of signal intensity for pSi and two different nSi substrates. Error bars represent one standard deviation.

The nSi targets also performed well when using a mixture of model peptides. Figure 4.10 shows LDI-MS spectra generated for different loading amounts of a peptide mixture including RASG-1, angiotensin fragment 1-7, angiotensin I, angiotensin II, bradykinin, and renin substrate. Using the nSi target, peaks from each of these analytes were generated for loadings of 1.5 fmol and 15 fmol, while all but RASG-1 (MW 1000.5) were apparent for the 150 amol loading case. Under identical sample target preparation conditions, peak intensities from the pSi target were significantly lower, with no peaks seen above noise at 150 amol loading.

(a)   (b)
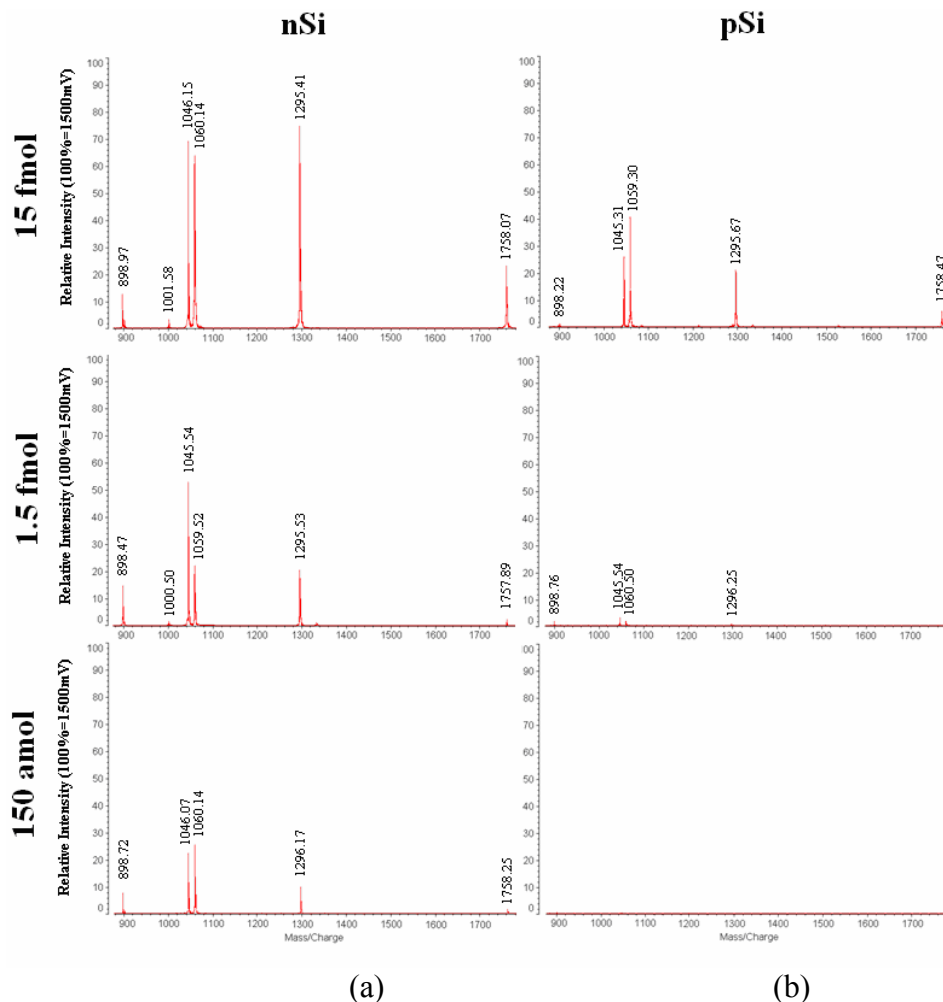
Figure 4.10: (a) LDI-MS spectra for a model peptide mixture at varying sample loadings on (a) nSi and (b) pSi substrates.

To observe the performance of nSi as a matrix-free LDI-MS substrate for the analysis of more complex peptide samples, a 700 fmol sample of BSA tryptic digest on nSi was also evaluated. As shown in Figure 4.11, the spectrum reveals many peaks between 500 and 2300 m/z corresponding to theoretical singly-charged digest fragments. Using the Mascot search engine (www.matrixscience.com, Matrix Science, Boston, MA), the matched peptides was listed underlined below. The spectrum was used to successfully identify BSA by peptide fingerprinting with 34% sequence coverage. The matched peptides shown in **Bold Underline** text below:

```
  1 MKWVTFISLL LLFSSAYSRG VFRRDTHKSE IAHRFKDLGE EHFKGLVLIA
 51 FSQYLQQCPF DEHVKLVNEL TEFAKTCVAD ESHAGCEKSL HTLFGDELCK
101 VASLRETYGD MADCCEKQEP ERNECFLSHK DDSPDLPKLK PDPNTLCDEF
151 KADEKKFWGK YLYEIARRHP YFYAPELLYY ANKYNGVFQE CCQAEDKGAC
201 LLPKIETMRE KVLASSARQR LRCASIQKFG ERALKAWSVA RLSQKFPKAE
251 FVEVTKLVTD LTKVHKECCH GDLLECADDR ADLAKYICDN QDTISSKLKE
301 CCDKPLLEKS HCIAEVEKDA IPENLPPLTA DFAEDKDVCK NYQEAKDAFL
351 GSFLYEYSRR HPEYAVSVLL RLAKEYEATL EECCAKDDPH ACYSTVFDKL
401 KHLVDEPQNL IKQNCDQFEK LGEYGFQNAL IVRYTRKVPQ VSTPTLVEVS
451 RSLGKVGTRC CTKPESERMP CTEDYLSLIL NRLCVLHEKT PVSEKVTKCC
501 TESLVNRRPC FSALTPDETY VPKAFDEKLF TFHADICTLP DTEKQIKKQT
551 ALVELLKHKP KATEEQLKTV MENFVAFVDK CCAADDKEAC FAVEGPKLVV
601 STQTALA
```
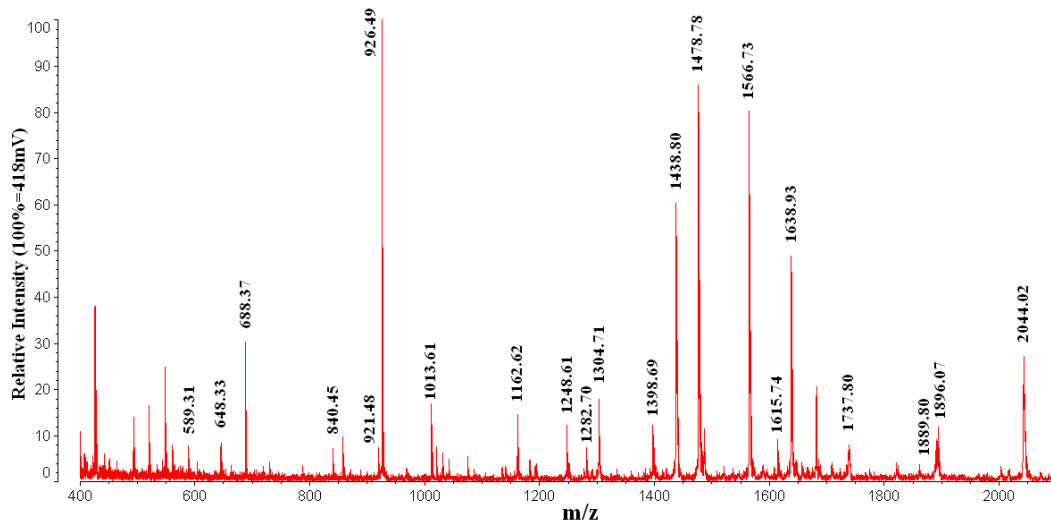

Figure 4.11: Mass spectrum of 700 fmol BSA tryptic digest sample.

4.3.3 Electrowetting Deposition

After fluorination of the oxidized silicon surface, the nanofilament regions display superhydrophobic behavior, with water droplets deposited on the nanofilaments exhibiting substantially higher effective contact angles than the surrounding un-textured surface. As a result of the low surface energy, sample droplets brought into contact with the nSi surface remain pinned to the capillary tip rather than transferring to the nanofilaments. However, application of a voltage between the nSi chip and sample droplet using the apparatus shown in Figure 4.12(a) allows the nanofilament surface energy to be increased through electrowetting. Selecting a suitable electrowetting bias enables the sample droplet to enter into the porous structure of the nanofilament network, substantially increasing the adhesion force between the droplet and chip surface and allowing complete droplet transfer from the capillary, as depicted in Figure 4.12(b).
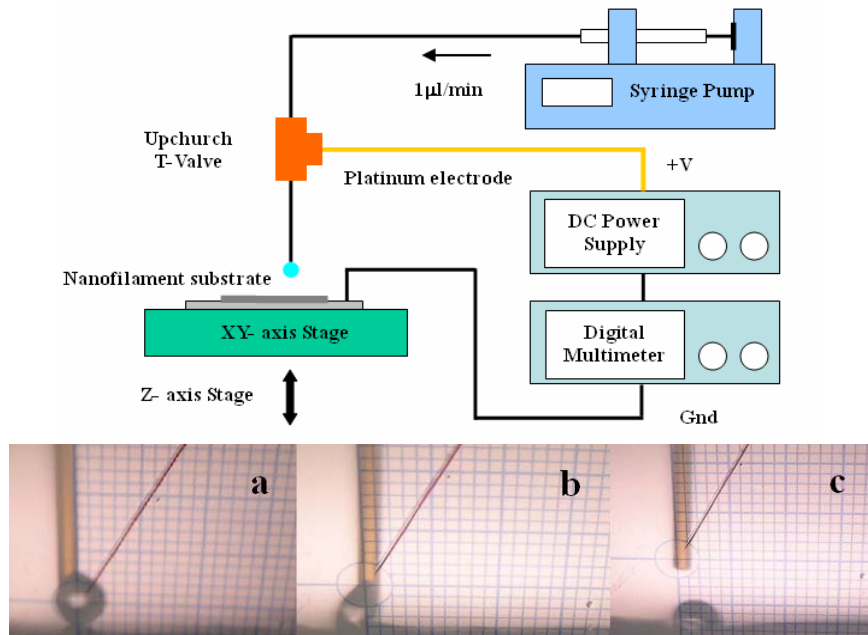
Figure 4.12: Electrowetting deposition setup and optical goniometer projection image shows electrowetting deposition to a superhydrophobic nSi surface.

As with other reports of electrowetting on nanostructured surfaces,[109-111] water contact angles on the nanofilament surfaces scale with the inverse of the electrowetting bias. As shown in Figure 4.13, effective contact angles drop from an initial value of 105° to steady-state values ranging from 46° to 70°, depending on the applied electrowetting bias, over a period of several minutes. The reduction in contact angle is due to liquid wetting the heights of nanofilaments to varying degrees. According to the Cassie model, hydrophobicity is strengthened because air pockets remain trapped below the liquid drop. This is a reasonable assumption for closed-cell porous surfaces such as pSi, since air cannot be readily displaced from within the pores. However, the analysis of electrowetting behavior on open-cell nSi requires a different treatment. According to the Wenzel model,[112] hydrophobicity of a rough surface can be geometrically modified due to the increase in effective surface area. For the Wenzel model, air may be partially or fully removed from the pores. In the latter case, the apparent contact angle of a water drop which fully wets the pores is described by,[113]

$$\cos\theta_o = 1 + \phi(\cos\theta - 1) \tag{2}$$

Based on this model, the apparent contact angle for an aqueous droplet which fully wets the pores of an nSi surface is predicted to be 60°. The somewhat lower contact angles observed at high electrowetting biases is likely due to a lower-than expected value of θ used in (2), since θ was determined for a smooth surface without electrowetting.
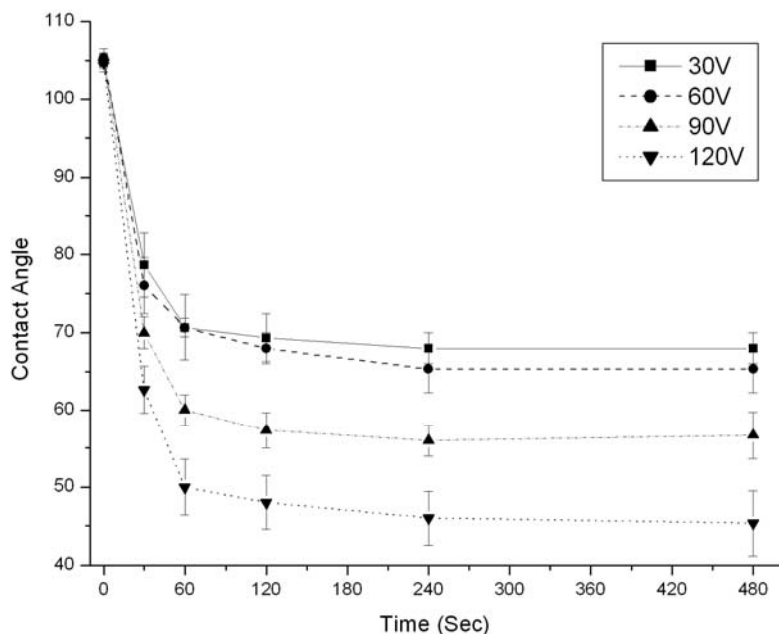
Figure 4.13: Hydrophobic to hydrophilic transition using electrowetting on nSi.

The observed time-dependence of the contact angle during electrowetting contrasts with a previous study of electrowetting on nanostructured surfaces which reported instantaneous Cassie–Wenzel transitions with correspondingly rapid decreases in water contact angle upon application of the electrowetting bias.[110] Instead, electrowetting on superhydrophobic nSi is found to be a dynamic process, with the time-dependent effective contact angle $\theta(t)$ exhibiting a smooth first-order step response upon application of a constant bias voltage, with a characteristic time constant of 22 s. This dynamic behavior allows precise control of contact angle by adjusting the voltage application time. In addition, it appears that the dynamic electrowetting also makes it possible to drive sample deep into the nanofilament matrix without wetting a large region of the chip. As a result, good analyte-surface binding may be achieved without sacrificing local sample concentration during the initial deposition step.

4.3.4 Electrowetting LDI-MS

The performance of nSi as an LDI-MS target was first evaluated in the absence of electrowetting. Spectral peak intensities for the model peptides were found to increase linearly with the applied electrowetting voltage used during sample deposition. At the same time, S/N was also found to increase, presumably due to larger amounts of contaminants entering the nanofilament pores at higher electrowetting biases. By optimizing the laser power to maximize S/N for each deposited sample spot, the average S/N value for each peptide was found to increase with the electrowetting voltage for loading amounts varying from 15 fmol to 150 amol. In Figure 4.14, measured S/N ratios for the three peptides with the highest spectral intensities, namely angiotensin I, angiotensin II, and bradykinin, are shown for each loading level. Overall, the average S/N was enhanced by a factor of 3.5 using the electrowetting approach. Electrowetting-enhanced sample deposition was also performed on the commercial pSi target substrate. Using identical deposition and LDI-MS procedures, electrowetting on the pSi targets resulted in an average S/N enhancement factor of 1.8, demonstrating that while the electrowetting technique can improve the performance of LDI-MS from pSi, the enhancement is not as pronounced as that observed from the nSi surfaces. This difference may be due to the contrasting morphologies of the two surfaces, with more favorable electrowetting of the open-cell nSi pores compared with the closed-cell pSi pores, which can trap air and prevent full wetting of the pore walls. Across all tests, optimal laser energy for the nSi surfaces was ~80% of the pSi energy levels, compared with only 2% reported by Vertes and co-workers for LDI-MS from silicon nanowire surfaces.[114]
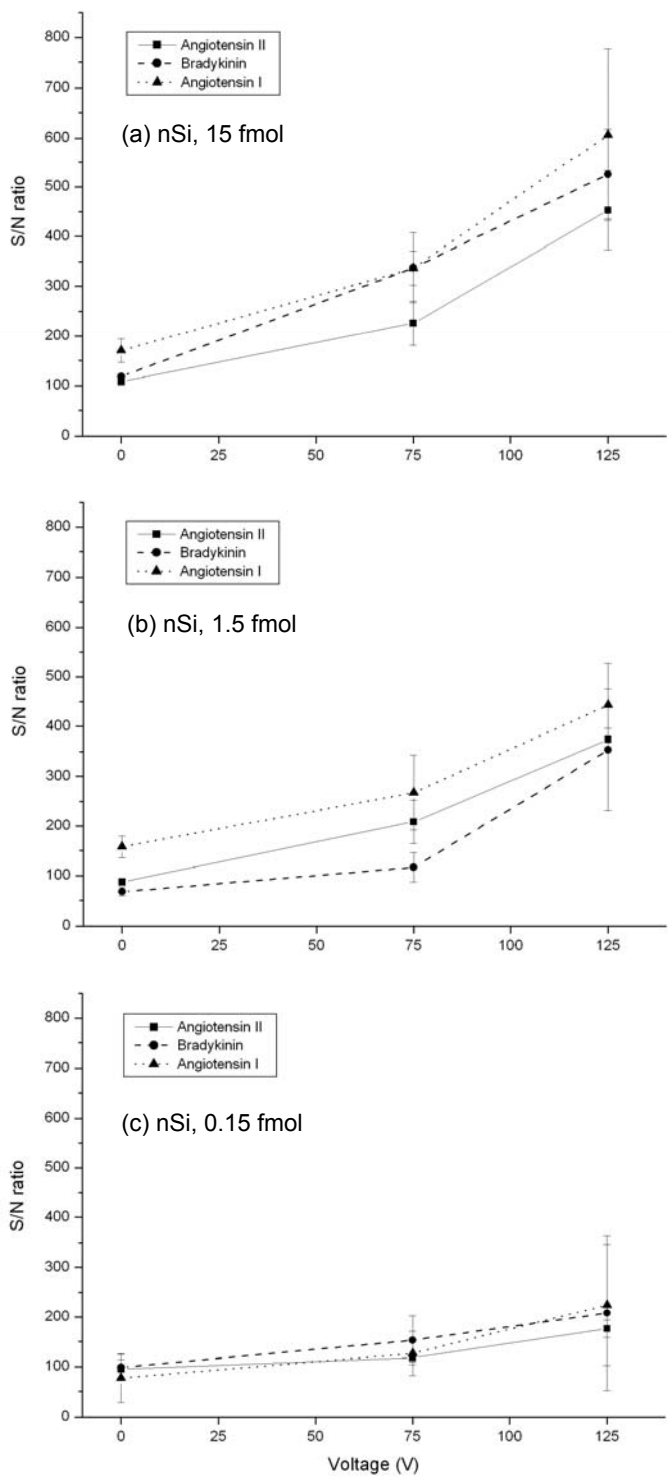
Figure 4.14: Signal-to-noise ratio of LDI-MS spectra for a peptide mixture spotted on an nSi chip using varying dynamic electrowetting voltages with (a) 15 fmol, (b) 1.5 fmol, and (c) 150 amol loadings. Error bar shows standard deviations based on three measurements across different spotting runs.

(a)	Angiotensin II		Bradykinin		Angiotensin I	
Electrowetting Voltage	Average S/N ratio	Standard deviation	Average S/N ratio	Standard deviation	Average S/N ratio	Standard deviation
0 V	107.85	6.10	118.56	4.95	170.66	23.55
75 V	225.77	44.61	337.39	70.20	336.32	34.36
125 V	452.83	79.95	524.93	93.20	606.26	170.67
(b)	Angiotensin II		Bradykinin		Angiotensin I	
Electrowetting Voltage	Average S/N ratio	Standard deviation	Average S/N ratio	Standard deviation	Average S/N ratio	Standard deviation
0 V	87.15	7.185	67.81	8.23	157.97	22.01
75 V	208.41	43.88	116.47	29.47	267.60	75.47
125 V	374.21	22.20	353.48	122.27	443.08	83.96
(c)	Angiotensin II		Bradykinin		Angiotensin I	
Electrowetting Voltage	Average S/N ratio	Standard deviation	Average S/N ratio	Standard deviation	Average S/N ratio	Standard deviation
0 V	94.91	18.55	98.69	25.95	76.98	49.22
75 V	117.44	8.80	152.88	48.97	126.73	44.28
125 V	176.30	17.63	207.92	155.43	224.29	122.19

Table 4.2: The data (with standard deviations) used to generate in **Figure 4.14** for S/N of (a) 15 fmol sample loading (b) 1.5 fmol sample loading and (c) 150 amol sample loading on nSi

4.4 Conclusions

Nanofilament silicon provides an attractive alternative to electrochemically-etched porous silicon for matrix-free LDI-MS as pioneered by Siuzdak and co-workers. The simple metal-assisted nSi fabrication process developed by Li and Bohn is easy to implement, highly repeatable, and amenable to large-scale production. The resulting nanofilament surfaces are particularly well suited for use with the dynamic electrowetting technique described here, with dynamic electrowetting on nSi LDI-MS targets substantial improvements in detection limits for a panel of model peptides. Further improvements may be possible by optimizing the nanofilament geometry and target preparation methods. Furthermore, the use of electrowetting for effective target deposition and nanofilament penetration, combined with on-target solvent

evaporation for *in situ* analyte concentration, is an attractive avenue towards higher sensitivity matrix-free LDI-MS.

The morphology of the nSi pores appears to be an important factor in providing signal enhancement by allowing analyte to penetrate deep into the nanofilament matrix. The open-cell structure of the pore network prevents the formation of air pockets, ensuring a complete Cassie–Wenzel transition upon application of a sufficiently high electrowetting voltage. While electrowetting is a particularly efficient method for controlling solvent/analyte penetration, similar results can likely be achieved using other approaches, such as pressure, vibration, heating, or a combination of these methods. Both vibration[113] and pressure[115] have been used to induce Cassie–Wenzel transitions on microtextured surfaces, although implementing these techniques for the preparation of LDI-MS targets may be more difficult than electrowetting.

Chapter 5   Mass Spectrometry Interfacing by Automatic Robotic Spotting

The ability to perform high-throughput bioanalysis in a single integrated platform is a substantial benefit offered by microfluidics technology. Spatially-multiplexed arrays of microchannels allowing large numbers of simultaneous on-chip analyses have been demonstrated for applications including immunoassays,[116] chemical reaction screening,[117] and enzymatic analyses,[118] and biomolecular separations performed by zone electrophoresis,[119, 120] gel electrophoresis,[121, 122] denaturing gradient electrophoresis,[123] and isoelectric focusing.[124]

For applications which require analyte detection with high mass accuracy, interfacing microfluidics with mass spectrometry (MS) is a necessity. There are several examples of microfluidic systems containing multiplexed microchannels interfaced to electrospray ionization (ESI) tip arrays for ESI-MS analysis.[5, 125, 126] In practice, such systems are not well suited to parallel analysis. ESI-MS is generally an on-line method, with data acquisition performed in real-time together with the on-chip analytical process. Coupling multiple electrospray tips with parallel MS analysis would thus require multiple MS tools, substantially limiting the practicality of this approach. A more compatible solution is to couple on-chip analyses with laser desorption/ionization methods such as matrix-assisted laser desorption/ionization (MALDI). In contrast to ESI-MS, MALDI-MS is an off-line soft ionization method in which sample is deposited onto a target plate and co-crystallized with a UV-absorbing organic matrix which aids in the ionization process

during UV laser irradiation.[34] The off-line nature of MALDI-MS allows parallel deposition of analyte from multiplexed microchannels onto the MALDI target plate, followed by serial analysis of the deposited analyte spots. Because the laser spot size is typically on the order of 200 μm, closely spaced sample spots may be analyzed without concern for crosstalk, allowing dense microchannel arrays to be effectively interfaced to off-line MS.

5.1 Multiplex Robotic Spotting / MS Interfacing

A variety of approaches for interfacing microfluidic systems to MALDI-MS have been demonstrated using techniques including microfabricated electrospray deposition,[19] electrowetting-based droplet manipulation,[20, 21] piezoelectric dispensers,[17] and centrifigual forces[23]. An overview of these and related approaches have been discussed in several recent review papers.[127, 128] In one particular approach explored by Knapp et al, a multichannel cyclic olefin copolymer (COC) chip developed for parallel reversed phase liquid chromatography (RPLC) analysis[129] was interfaced with a MALDI target through an electrically-mediated deposition technique[130] which was shown to be robust for the case of a 2-channel chromatography chip. In the present work, we describe a simpler approach for interfacing multichannel microfluidics with MALDI-MS based on hydrodynamic contact spotting. Compared to other methods, contact spotting provides a generic approach to MALDI interfacing which is straightforward to implement and integrate, highly robust even for large numbers of multiplexed microchannels, and compatible with a wide dynamic range of flow rates. The approach is similar in concept to a

multi-capillary platform reported by Aebersold et al,[131] in which an array of RPLC capillary columns was coupled with MALDI-MS by direct contact spotting.[131] A network of discrete capillaries interconnected by microjunction fittings was used to interface a single gradient pump to four parallel separation columns containing silica beads as a stationary phase for RPLC. Eluent from each column was deposited by contact spotting onto a stainless steel MALDI target using a commercial fraction collector. In a more recent demonstration by Liu and Zhang, a multidimensional separation system combining a single strong cation exchange (SCX) column with an array of 10 parallel RPLC capillary columns was coupled with MALDI-MS by contact spotting from the distal ends of the RPLC capillaries.[132] The system employed a machined polymer tube for interfacing the SCX column with the RPLC capillary array, and a rack of 3-way valves connecting each spotting tip to an individual pump to enable controlled droplet deposition onto the MALDI target. Unlike these capillary platforms, the microfluidic chip technology presented here combines a fully integrated flow splitter and parallel microchannels for contact spotting onto a MALDI target. The repeatability and robustness of the platform is demonstrated using a panel of model peptides deposited from the parallel spotting tips. Future integration of separations with the multichannel spotting technology is also discussed.

The concept of interfacing multiplexed capillary LC separations with MALDI-MS for high-throughput proteome analysis was first described by Aebersold's group using a system comprising 4 parallel capillary LC columns coupled with MALDI-MS/MS.[131] In their system, a network of capillaries interconnected by

microjunctions deposited by direct mechanical spotting onto a MALDI target. Electrically assisted deposition technology such as using pulse electrical field [129] [130] and electrospray [19] method have been presented. However, those methods require high driving voltage and increasing system complexity. In contrast, the direct mechanical spotting strategy described by Aebersold et al. [131] is well suited multichannel microfluidic chips employing a chromatographic separation in the second dimension

5.1.1 Multichannel Microfluidic Chip Fabrication
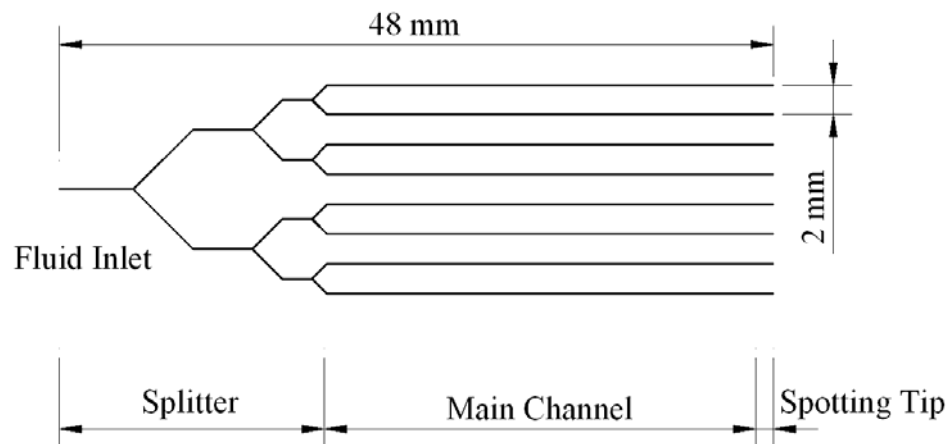
Figure 5.1: Design layout of 8 channel spotting chip

The 8-channel spotting chip design layout is show in Figure 5.1. To achieve the uniform flow distribution, The 8-channel COC spotting chip consists of a symmetric 3-stage splitter connecting a single input port to an array of 8

parallel microchannels with 2 mm spacing. Each channel was nominally 100 μm wide and 46 μm deep, with geometric variances of less than 1.5% measured across all channels prior to chip bonding. The overall microchannel network was 50 mm long from input port to spotting tips.

The general fabrication process flow of spotting chip is show in Figure 5.2. First, the mulitchannel COC spotting chip was fabricated by hot embossing from a deep reactive-ion etching (DRIE) silicon template. The patterns on DRIE template were defined by spun a 4.5 μm thcik positive type photoresist onto a 10cm diameter silicon wafer follow by UV exposure and photoresist development. The patterned wafer was transfer to deep reactive ion etcher (Surface Technology Systems, Newport, UK) to create a 45 μm deep channel feature shown in Figure 5.2.

DIRE Template
1. DRIE Template fabrication

COC substrate
2. Hot embossing

3. Solvent Bonding

4. Tip milling

5. Dicing

6. Hydrophobic Coating
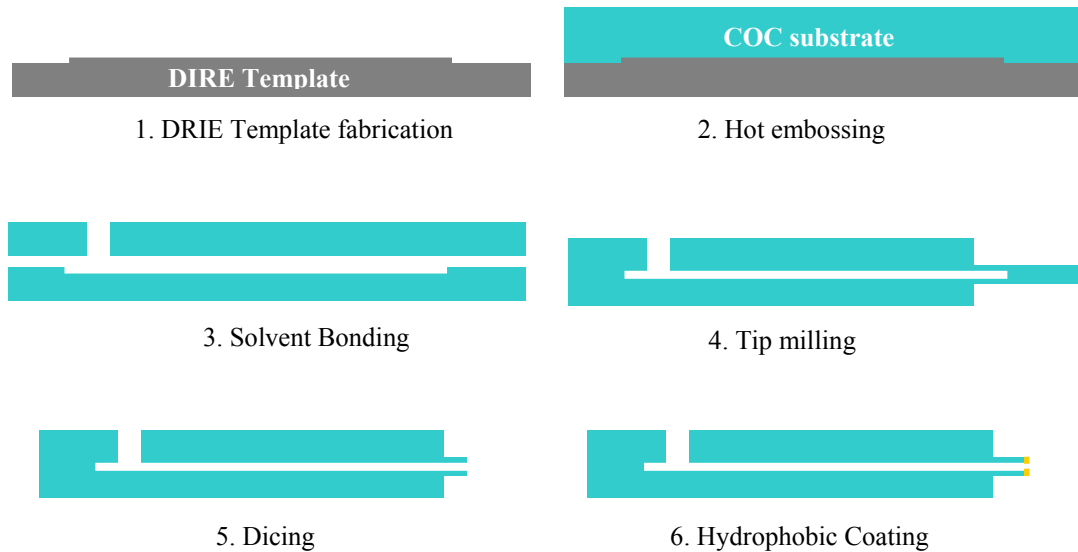
Figure 5.2: Fabrication process of spotting chip

2.0 mm thick COC sheet (Zeonor 1020 R, Zeon Chemicals L.P., Louisville, KY) was cut into 3x8 cm pieces using tabletop dicing saw (Micro-Mark, Berekely Heights,NJ) followed by deburring the polymer residues after dicing. The COC substrate rinsed with 2-propanol (IPA) and DI water, dried with N_2, and dehydrated in a vacuum oven at 85 ^{o}C for 2 hr. COC replica is generated upon the DRIE template by hot embossing using commercial hydraulic hot press (AutoFour/15, Carver, Wabash, IN). The press platens were preheated to 125 ^{o}C, followed by application of a fixed pressure of 2.0 MPa. After 10 min, pressure was released, the platens were cooled to 95 ^{o}C, and the imprinted COC plate was removed from template. The imprinted substrate was solvent bonded to a second COC plate pre-drilled with a 1.5 mm diameter reservoir hole using a precision CNC milling machine (MDX-650, Roland ASD, Lake Forest, CA). A small volume of cyclohexane (J.T.Baker, Phillipsburg NJ) was placed in a glass beaker and the pre-drilled COC plate was fixed on a glass cover which sealed the beaker. After 5.5 min of cyclohexane vapor deposition at room temperature, the COC substrates were aliged and bonding at 3.5 MPa for 10 min in the hot press.

After solvent bonding, the chip was shaped using a high precision CNC milling machine (MDX-650, Roland ASD, Lake Forest, CA) to produce regions with cross-sections 1 mm wide and 500 μm thick surrounding each of the spotting tips, followed by a final cut to expose the fluid exit points using a semiconductor wafer dicing saw (DAD321, Disco Hi-Tec America, Santa Clara, CA) using a Disco SDC320R11B dicing blade. Finally, Teflon AF (DuPont Fluoroproducts, Wilmington, DE) was coated on tip surfaces as hydrophobic layer by incubating in

oven at 85 °C for 2 hr. Figure 5.3 shows (a) An 8 channel COC chip with on-chip spotting tips, and (b) electron micrograph showing a single spotting tip following chip dicing.
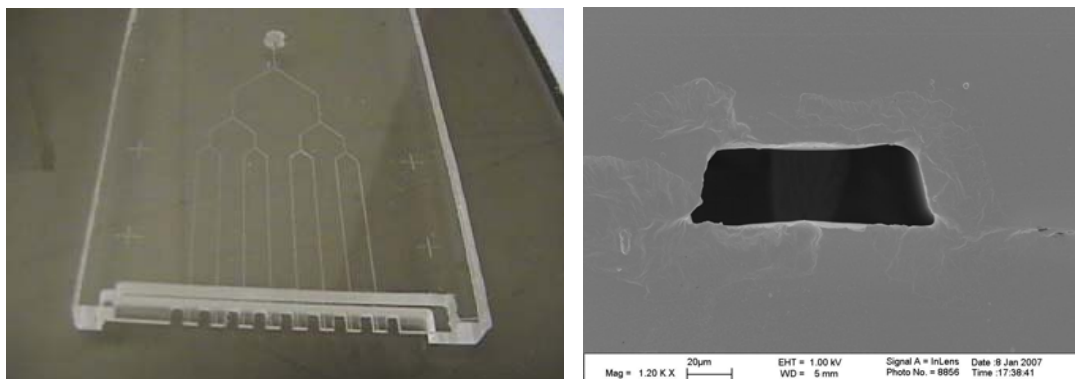
Figure 5.3:(a) An 9 channel COC chip with spotting tips (b) SEM image of spotting tip after dicing

After tip dicing, the chip exit surfaces exhibit weakly hydrophilic behavior, with a sessile water contact angle around 65° which is lower than the native COC surface of 95° reported before. The contact angle drop is caused from the scratches on the exit COC surface after dicing as shown in Figure 5.4 (a). Higher contact angles are desirable to prevent droplets from wetting the chip outlet during spotting. Strongly hydrophobic exit surfaces can also encourage easier droplet transfer to the MALDI target, particularly for smaller droplets, by reducing the contact forces between droplets and spotting tips. Teflon AF has been widely used as a simple approach to produce hydrophobic layer with good mechanical property and chemical resistance and Teflon AF can be dissolved in a range of perfluorinated solvents into various viscosity. Perfluoro-(2-perfluoro-n-butyl)tetrahydrofuran (FC-75, 3M Corporation, St. Paul, MN) was used as perfluorinated solvent in this research. The deposition of partially-densified

Teflon AF on the exit surface resulted in a water contact angle of 105° as shwon in Figure 5.4(b), rendering the surface substantially more hydrophobic than native COC.
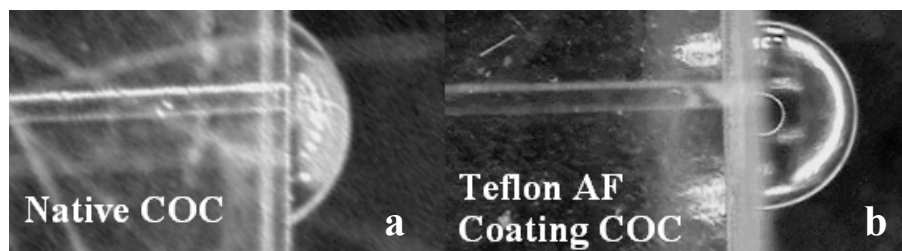
Figure 5.4 : Hydrophobicity of COC exit surface

5.1.2 MALDI Target Plate

For off-line MS interfacing approach, detection sensitivity can be further improved by target plate modification. In conventional approach, the liquid sample spreading on the stainless steel target plate resulting the sample spots size typically measure around 5~10 mm^2. For approximately 200μm diameter laser spot size, only small portion of deposited sample was analyzed during the mass spectrometry test which limits the performance. Schuerenbeg et al [28] have been reported that the detection sensitivity can be greatly enhanced by simply spotting a gold anchor on a Teflon film. The Teflon layer used as hydrophobic background to constrain lateral sample spreading while the sample was condensed into laser-spot size hydrophilic anchor. This approach can effectively increase the local sample concentration hence increasing the mass spectrometry sensitivity and also service self-align deposition method.

In this research, the prestructured MALDI target plate is fabricated by coating a thin Teflon AF layer as hydrophobic background and evaporating gold layer as hydrophilic anchor on a mirror-polished stainless plate (McMaster-Carr, Chicago, IL). The MALDI target plate design is show in Figure 5.5, each gold anchor is 2mm away from the other which corresponds to the 8 channel spotting chip. 64 sample spots are deposited onto the target substrate in a single spot run with maximum 32 spot runs/256 sample spots in one MALDI target substrate. The fabrication process is show in Figure 5.5. First, Teflon AF was spin coated onto a 5x5 cm mirror polished stainless steel plate follow by incubated in oven at 250 ^{o}C for 2hr. Then 250um diameter and 3000A thick gold anchor array was deposited onto Teflon AF coated stainless steel substrate by E-beam deposition system (CHA Industries, Fermont,CA).
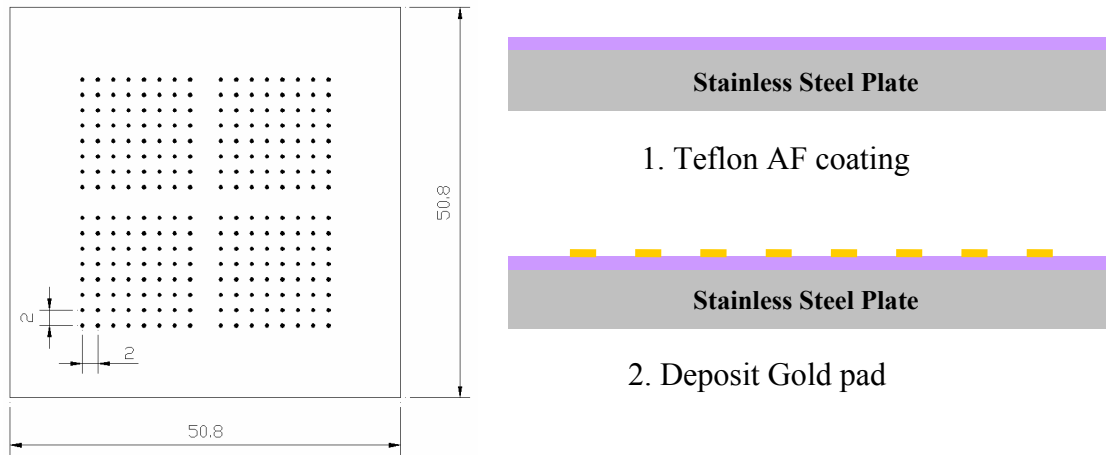
Figure 5.5: MALDI target plate fabrication process and design layout

A custom made mass spectrometry target holder for Kratos Amixa time-of-flight (TOF) mass spectrometer (Kratos Analytical, Manchester, UK) was machined by CNC. The detail design and drawing was shown in Figure 5.6 below:
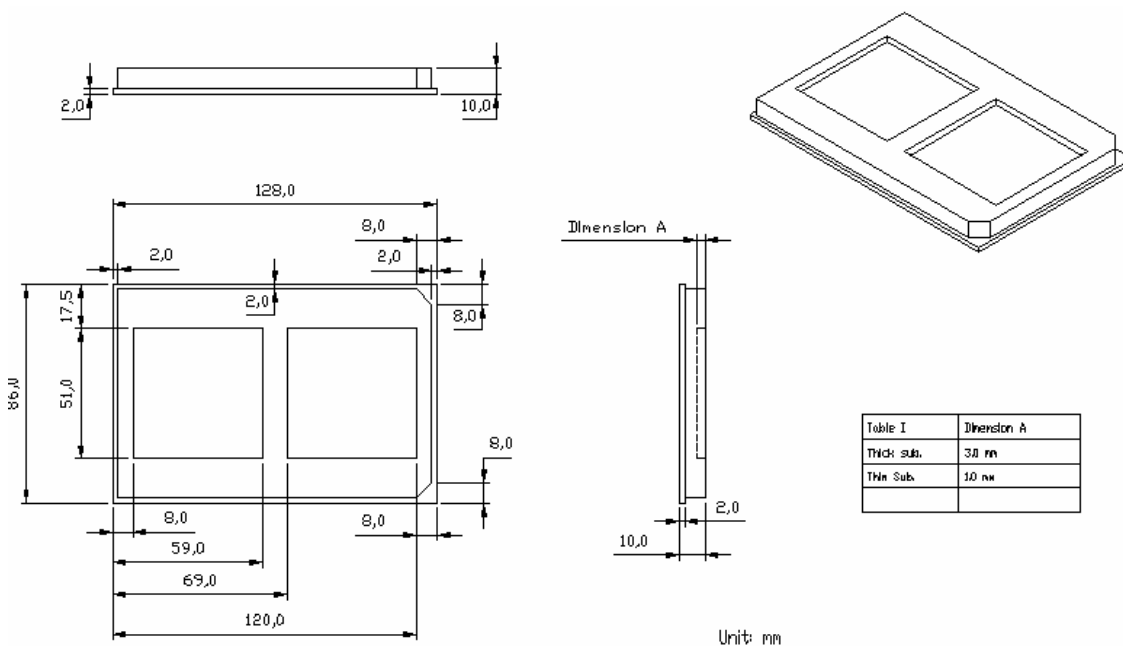
Figure 5.6: Custom made MALDI Target holder for Amixa time-of-flight (TOF) mass spectrometer

5.1.3 Monolith Fabrication

In order to have good monolith-channel interface, chips tested with methacrylate monoliths integrated into the channels, the COC microchannel walls were modified by first filling the channels with a solution of 50 wt% Ethylene glycol dimethacrylate (EGDMA) and 50 wt% MMA mixture. After 6 hours the EGDMA/MMA mixture was N_2 purge away from microchannel and filled with nitrogen purged monomer mixture consisting of 24 wt% butyl methacrylate (BuMA), 16 wt% EGDMA, 50 wt% 1-dodecanol, 10 wt% Cyclohexanol and

106

1wt% 2,2'-dimethoxy-2-phenylacetophenone (DMPAP) with respect to monomer. The monomer mixture filled COC chip was covered by photomask leaving 6mm long section near the microchannel end for 10 min UV irradiation with 35cm distance from Tamarack PRX-1000 UV Source (PRX-1000; Tamarack, Corona, CA). After UV polymerization, the unreact monomer mixture was washed with methanol at 0.1μL/min flow rate for 12 hours. This process, first described by Frechet et al [133], results in a monolith with a morphology well suited for application to liquid chromatography.

Instead of bonding with Nanoport capillary interface, a low-dead volume, high-pressure resistance needle interfacing approach is used for monolith filled microchannel. COC cover plate pre-drilled with a 0.65 mm diameter reservior hole to mate with stainless steel needle. The chip fabrication employed thermal embossing from a silicon master template and previously-reported solvent bonding process. After chip was solvent bonded, a 25.4 mm long section of #22 gauge blunt-end stainless steel needle stock (Hamilton, Reno, UT) was inserted into the pre-drilled reservior on the COC chip and connected with a capillary fitting (Upchurch Scientific, Oak Harbor, WA) to produce a low dead-volume interconnection. Figure 5.7(a) shows an 8-channel chip fabricated using this process. The micrograph of a typical monolith-coupled microchannel exit shown in Figure 5.7(b) reveals porous monolith structure with 1~2μm pore size.
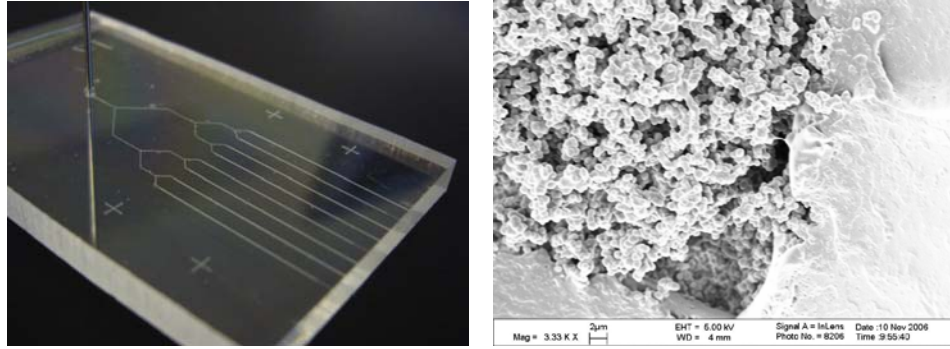
Figure 5.7: 8 channel spotting chip with 6mm monolith

5.1.4 Automatic Robotic Spotting System

In this research, a robotic spotting system was developed to automate the spotting process. Resolution, accuracy and repeatability were the three major factors investigated in this motion control system. The high-resolution positioning is achieved using lead screw and micro-stepping stepper motor (Parker Hannifin,Rohnert Park,CA) with 5 μm position resolution. Optical encoder was used to detect missing steps in this stepper motor driven system. The weight of spotting system is minimized (<1lb) and the acceleration is optimized below the threshold of the stepper motor to avoid the overloading effect. Together with friction-free linear ball slides, missing step can be avoided which simplify the control algorithm design. The accuracy of the system is achieved by using high grade ground lead screw. The repeatability of the system is determined by the movement of the stage and the home position. Although zero backlash couplings and anti-backlash nut were used to get high repeatability of the movement homing error can be accumulated after large number of runs. Therefore home sensor with high repeatability (<5 μm) and quick response time (< 100μs) were used to achieve the accuracy and repeatability of homing position.

108

The performance of the spotting system is also affected by the alignment between the XYZ stage, the device and the MALDI target. A fixture is designed to maintain high repeatability and accuracy for changing device and target. The parallelness between the XYZ stage and the MALDI target spot position and verticalness between the target surface and the device channels are critical for accurate alignment. Therefore a manual XYZ stage and rotation table is used for fine tuning of initial setup. A control program and graphic user interface was developed by LabVIEW (National Instrument, Austin, TX) As shown in Figure 5.8, the control interface allows user to control robotic arm position, spotting speed, spotting time with automatic and manual mode.
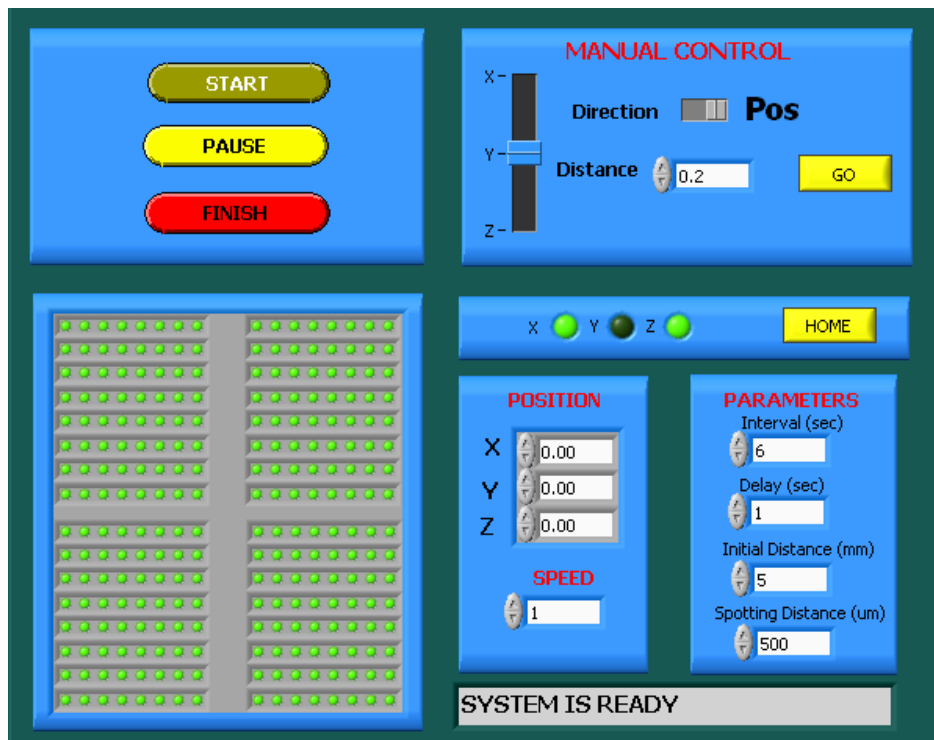
Figure 5.8: Robotic spotting system user interface

5.1.5 Interfacing Multiplexed Microfluidics to MALDI-MS

The experiment set up was show in Figure 5.9. The spotting chip inlet was connect to the computer flow rate control syringe pump (Harvard apparatus, Holliston, MA) through 100μm inner diameter capillary interfacing with Nanoport (Upchurch Scientific, Oak Harbor, WA) .The spotting chip was fix on the LabView controlled X-axis position stage and the channel exit surface was aligned with the MALDI target substrate which was fixed on the LabView controlled Y-Z axis position stage. The spotting chip tip was aligned and placed 2mm away from the gold anchor in MALDI target plate as initial position.

Automatic spotting was performed by moving the chip 200 μm from the target surface to transfer droplets to the gold pads, then returning to the initial 2 mm gap and indexing the stage for the next row. Sequential images of the robotic spotting process are shown in Figure 5.10. Each of the 8 channels deposited droplets in parallel onto the MALDI target plate, with a total of 8 spotting events to fill the array. For each experiment, peptide sample premix with matrix solution was deposited onto 64 target spots in an 8 x 8 array.
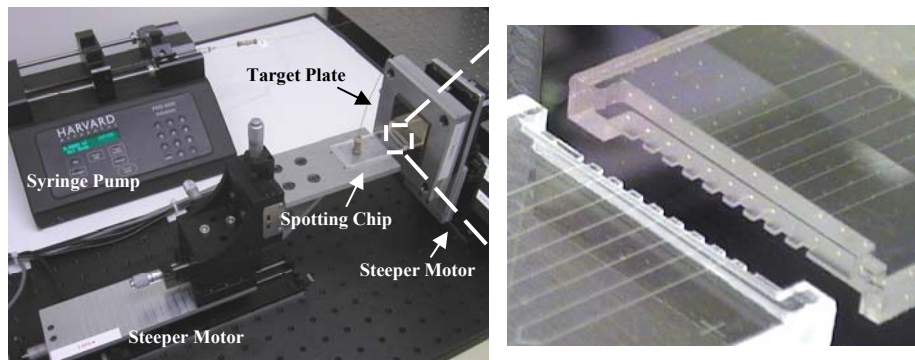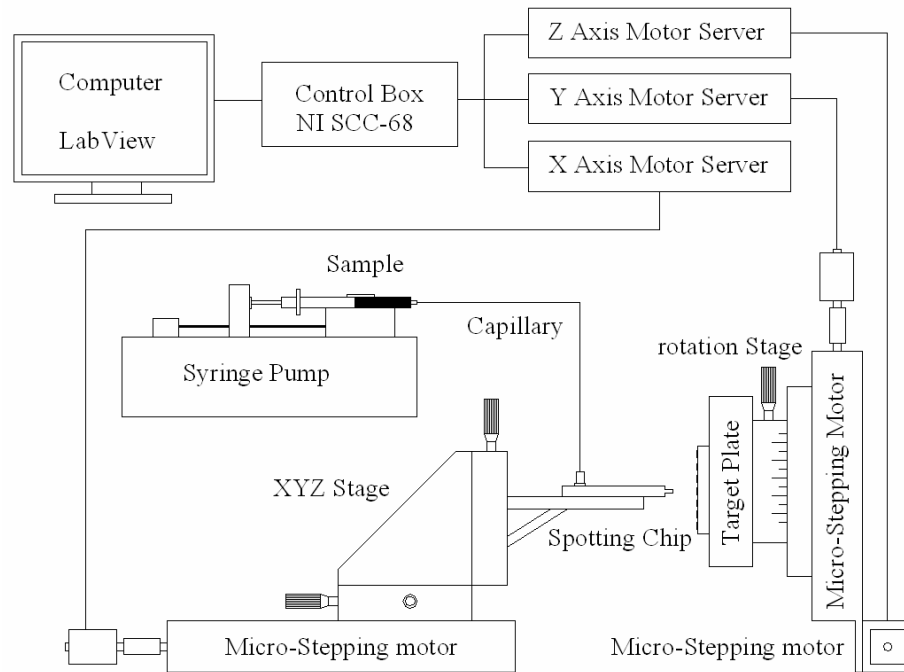
Figure 5.9: Experiment setup of robotic spotting system
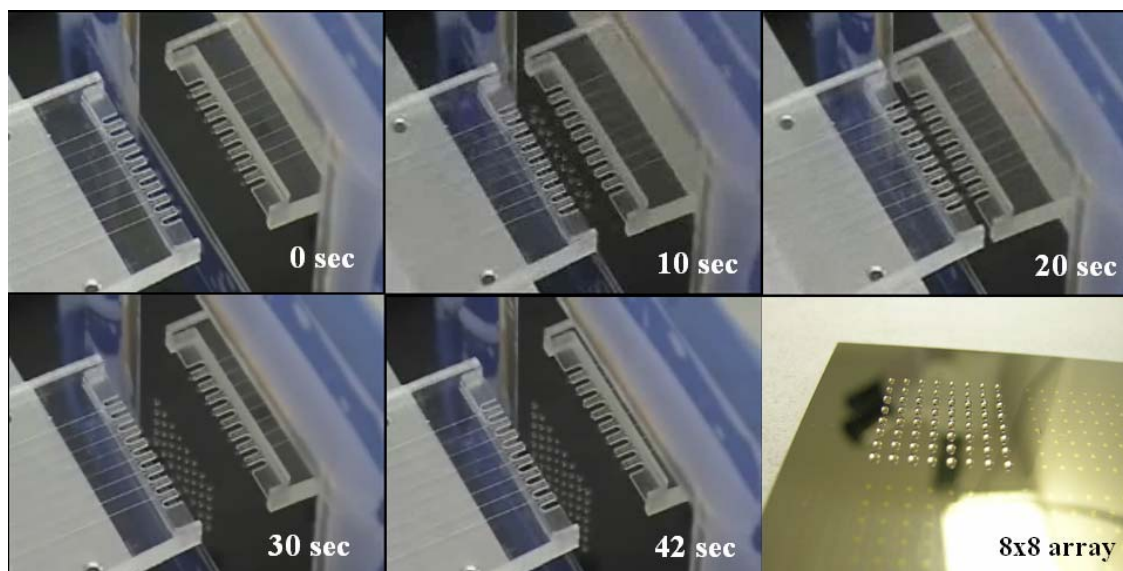
Figure 5.10: Consecutive images of the automated contact spotting process using a 12 µL/min total flow rate and 6 sec interval between spotting events, resulting in an 8x8 array of 150 nL droplets deposited on the microsctructured MALDI target surface.

Following spotting, the array of droplets was air dried, leaving co-crystallized sample and matrix on the gold anchors. The hydrophilic anchor pads were found to be effective in encouraging the efficient transfer of droplets from the hydrophobic chip spotting tips. The anchor pads also served to maintain the positions of the deposited droplets once transferred to the MALDI target. Figure 5.11(a) shows sequential images of the solvent evaporation and sample/matrix co-crystallization process on a single gold anchor pad. The 8x8 co-crystallized sample/matrix spots using automatic robotic spotting system is shown in Figure 5.11(b). A nominal deposition volume of 150 nL was achieved for each spot, corresponding to 75 fmol of each model peptide. Despite the use of the gold anchor pads, the final spots exhibited significant inhomogeneity in sample distribution following evaporation, with a portion of the sample displaced outside of the anchor region, suggesting that the Teflon AF layer

beneath the gold anchors is not sufficiently hydrophobic to fully prevent wetting of this film from occurring.
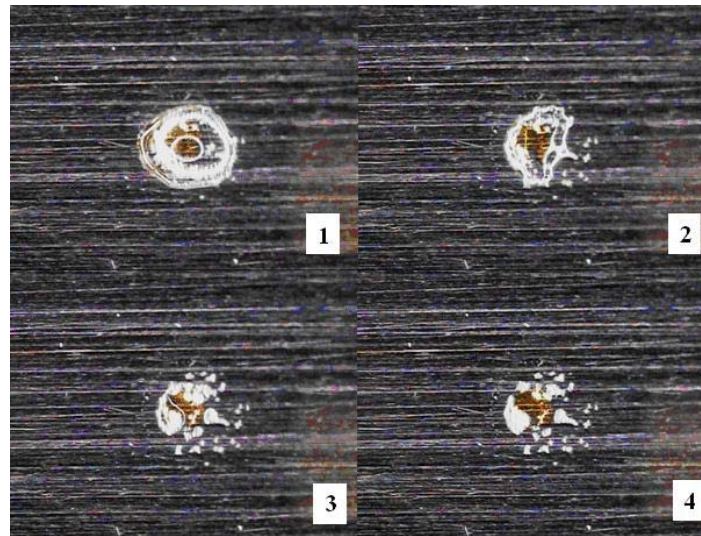
(a)
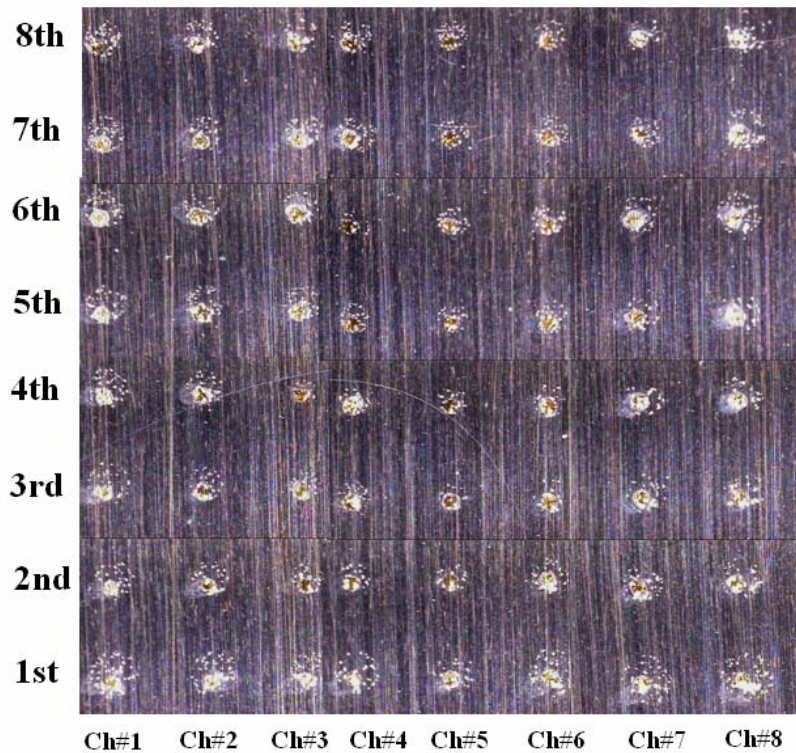
(b)

Figure 5.11: (a) Solvent evaporation and sample/matrix co-crystalization on gold target anchor (b) 64 sample spots in 8 consequent spot run

5.2 Multiplex Spotting Theory

To better understand the parameters which affect droplet formation in microchannel spotting arrays, a model describing the formation process was developed and used to evaluate the critical parameters which affect spotting performance. Assuming laminar flow of an incompressible fluid, the Hagen-Poiseuille equation dictates the flow rate, Q, in any given channel as:

$$Q = \frac{1}{Z_f}(P_h - P_c)$$ (1)

where Z_f is the hydraulic flow resistance, P_h is the pressure applied at the channel inlet to generate hydrodynamic flow, and P_c is the capillary pressure resulting from surface tension of the liquid/air interface at the capillary outlet. The capillary presure is defined as:

$$P_c = \frac{2\sigma}{R}$$ (2)

In this expression, σ is the surface tension of the liquid and R is the radius of curvature of the droplet surface, which in turn is a function of boundary constraints including local geometry and contact angle of the liquid with the microchannel walls. For flow with the free liquid surface entirely within a given microchannel, R possesses a nominal value R_o which can be defined in terms of the effective hydraulic radius of the channel, r_h, as

$$R_o = \frac{r_h}{\cos(\theta)}$$ (3)

where θ is the complementary angle to the contact angle for liquid on the microchannel wall.

The flow resistance in Equation (1) can be expressed in terms of the viscosity, η, channel length, L, and hydraulic radius as,

$$Z_f = \frac{8\eta L}{\pi r_h^{4}} \tag{4}$$

To simplify the analysis, the rectangular microchannels used in this study were approximated as circular cross-sections channels with hydraulic radii given by[134]

$$r_h = \frac{wh}{(w+h)} \tag{5}$$

where w and h represent the channel width and height, respectively.

As liquid is pumped out of the channel exit, R undergoes a significant change, due to the varying boundary conditions, which can strongly affect the ability to generate uniform spotting droplets. Refering to Figure 5.12, consider a single microchannel with a circular cross-section. As liquid is pumped along the microchannel (a), R remains constant until the free liquid interface reaches the end of the channel (b). Assuming the exit surface is sufficiently hydrophobic to prevent immediate wetting, the radius of curvature of the liquid/air interface rapidly drops as the volume of liquid outside the channel increases, until R

reaches a minimum value of R_x (c). At this point, R is coincident with the hydraulic radius of the channel, i.e. $R_x = r_h$.

As the liquid volume outside the channel continues to grow, there is an associated increase in the radius of curvature for the emerging droplet. The edges of the droplet remain pinned at the circumference of the channel exit, until the tangent angle between the droplet and the chip surface equals the native contact angle of the exit surface itself (d). Once this occurs, it becomes energetically favorable for the droplet to begin wetting the surface, rather than remaining pinned at the channel exit. The contact angle remains constant for the remainder of the droplet formation process, while the radius of curvature continues to grow. If a sufficient fluid volume exits the channel, the increased R can result in lower capillary pressures than those initially found in the partially-filled channel (e). The sharp drop in R (and thus incease in P_c) observed in Figure 5.12 when the free liquid surface becomes pinned by the discontinuity at the channel exit presents a large energy barrier for liquid exiting the chip. Consider the case of multiple channels coupled to a single inlet reservoir through a flow splitter, with a fixed overall flow rate imposed at the inlet. Due to slight variations in channel geometry, contact angle, and related factors, liquid will not reach the end of all channels simultaneously, but rather will first exit from the channel with the lowest hydraulic resistance.
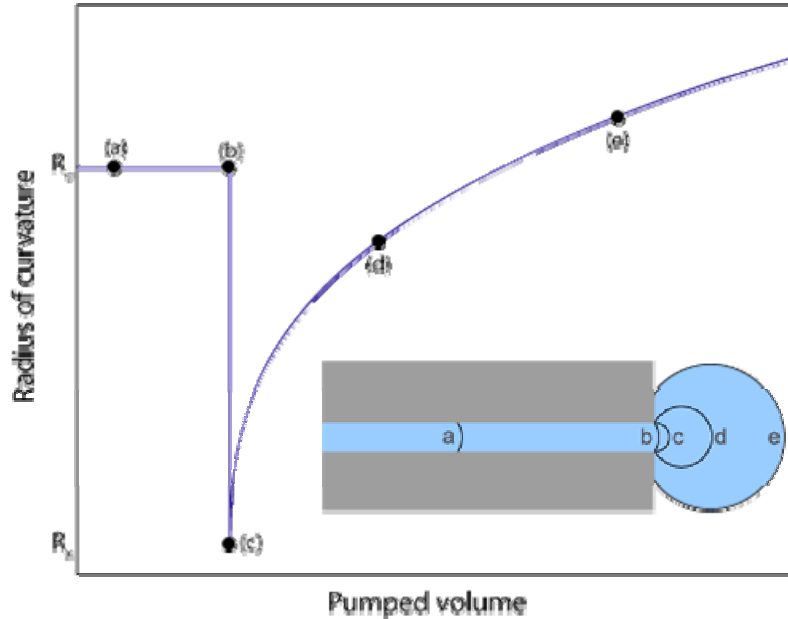
Figure 5.12: Qualitative evolution of interfacial radius of curvature as a function of total displaced volume within a single microchannel. Six distinct stages may be identified, namely (a) liquid/air interface entirely within the channel, (b) interface at the channel exit, (c) minimum R equal to the hydraulic radius of the channel, (d) maximum R before wetting of exit surface, and (e) continued droplet growth leading to values of R equal to, and eventually larger than, the initial curvature within the channel.

As liquid reaches the first channel exit, further flow is resisted by the large and sudden jump in capillary pressure to a maximum value of P_{cx}, corresponding to the capillary pressure when $R = R_x$. Initially, this pressure jump results in a larger portion of the flow being delivered to other channels in the array, reducing variations between the positions of liquid fronts among the channels. However, sufficient flow will eventually occur within the first channel to gradually increase the droplet radius and reduce the associated capillary pressure. As P_c drops, the applied pressure required to maintain the set flow rate is also reduced. In extreme cases, P_c can become small enough that the applied pressure required to pump all liquid through the first wetting channel is lower than the maximum capillary

pressure required for liquid to exit each of the remaining channels. In this event, a droplet is formed only at the first channel exit. This issue is more problematic as the overall flow rate is reduced. At low Q, the applied pressure required to generate the entire flow through a subset of channels within the array becomes relatively small. If the required pressure is less than the maximum capillary pressure, any channel which has not already overcome the energy barrier will never form a droplet and thus experiences dry-out conditions.

5.2.1 Analytic Droplet Formation Model

A simplified model of the process described in Figure 5.12 can be derived by applying Equation (1) to each individual channel, with the total flow rate given by the sum of individual flow rates, Q_i, within each channel, i.e.,

$$Q = \sum_{i=1}^{n} Q_i = \sum_{i=1}^{n} \frac{1}{Z_f} \left(P_h - P_{ci} \right) \tag{6}$$

In this expression, n is the total number of channels in the array, P_{ci} is the capillary pressure within the ith channel, and it is assumed that the hyrdaulic resistance for all channels is equal. Assuming that liquid has overcome the energy barrier within only m channels, each with an instantaneous capillary pressure equal to some nominal value P_{co}, while forward flow within the remaining n-m channels is prevented due to the maximum capillary pressure, P_{cx}, then Equation (6) can be solved for the hydrodynamic pressure P_h required to generate the total imposed flow Q as,

$$P_h = \frac{1}{n} \left(QZ_f + mP_{co} + (n-m)P_{cx} \right) \tag{7}$$

118

which can then be solved for *m*, providing an estimate for the number of channels which generate full droplets:

$$m = \frac{QZ_f}{P_{cx} - P_{co}} = \frac{nQ_dZ_f}{P_{cx} - P_{co}} \qquad (8)$$

In Equation (8), Q_d is the desired flow rate in each individual channel. The actual value of P_{co} depends on the volume of liquid which has exited the wetting channels, with possible values ranging between P_{cx} (just after reaching the minimum droplet radius) and zero (in the limit as an infinite volume is ejected from each wetting channel). In practice, variations in P_{co} occur due to different times of arrival of the liquid fronts at the channel exits during the initial filling of the channels. Differences can also arise from variations in the amount of liquid removed from the channels as droplets are transferred to another surface, for example in the case of contact spotting onto a secondary substrate.

While the actual value of P_{co} must be determined experimentally, behavior at the limits can be readily evaluated. The minimum required flow rate per channel to ensure that all channels develop full droplets ($m = n$) can be found from Equation (8):

$$Q_{d,min} = \frac{P_{cx} - P_{co}}{Z_f} \qquad (9)$$

When $P_{co} \rightarrow P_{cx}$, all channels are on the verge of overcoming the capillary pressure imposed by the reduction in droplet radius, and a vanishingly small flow

per channel ($Q_{d,min} \rightarrow 0$) is required to ensure full droplet generation from all channels in the array. The limit as $P_{co} \rightarrow 0$ defines the maximum flow rate needed to ensure droplet formation on all channels:

$$Q_{d,max} = \frac{P_{cx}}{Z_f} \tag{10}$$

As revealed by Equation (9), the required flow rate for intermediate values of P_{co} between zero and P_{cx} can be interpolated between zero and $Q_{d,max}$.

5.2.2 Iterative Numerical Droplet Formation Model

Equation (8) provides a prediction for the number of channels, m, which have overcome the energy barrier defined by the minimum radius of curvature for the emergent droplet. It was assumed that liquid exiting from all m channels possessed equal radii of curvature. This assumption ignores the likelihood that droplets will emerge at slightly different times from each channel, resulting in differences in R among the droplets. A more precise model which takes this variability into account can be developed from analytic expressions of the droplet volume and radius at each stage of the process depicted in Figure 5.12, with R derived as a function of volumetric liquid diplacement and local channel geometry. An iterative numerical simulation based on this approach was implemented in MatLab (MathWorks, Natick, MA) to determine the behavior of the process for an arbitrary number of microchannels connected symmetrically to a single flow source. At each time step, the local radius of curvature is determined for each channel, with the resulting capillary pressure from Equation (2) used to

find the instantaneous flow rate within each coupled channel using Equation (1). The flow rates are then employed during the next time step to determine the pumped volume within each channel, thereby defining the initial liquid positions and radii of curvature for the next time step.

(a)   (b)
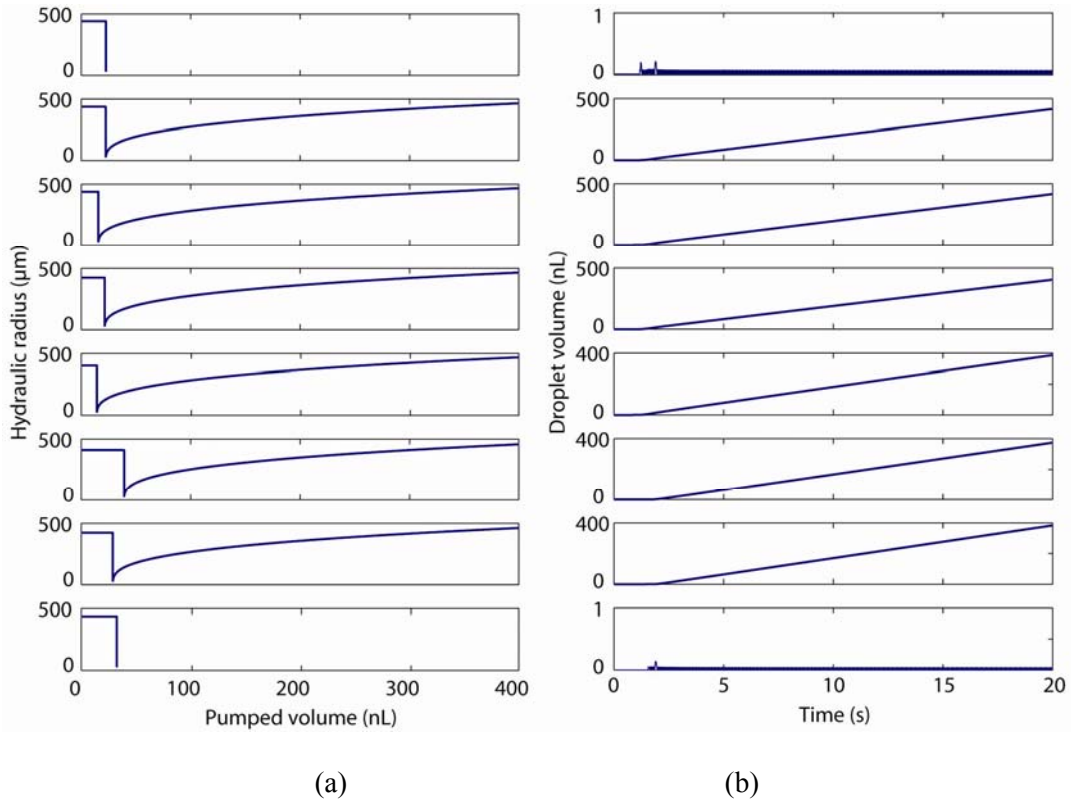
Figure 5.13: Flow simulation results for an 8-channel array fabricated in a COC chip showing (a) radius of curvature vs. pumped volume within each channel of the array, and (b) droplet volume vs. time. The microchannels have a nominal hydraulic radius of 30.6 μm and an effective length of 5 cm. All channels were connected to a common flow source delivering a fixed 8 μL/min total flow rate of water through the chip.

The developed code was applied to the 8-channel chip shown in Figure 5.7. Sessile water contact angles were determined for the bare COC surface and the Teflon AF coated exit surfaces using a goniometer (Cam Plus Micro; Tantec Inc.,

121

Schaumburg, IL,USA) to provide accurate measurements of surface tension for each surface. Experimental variations in liquid fronts during chip filling were found to occur with a Gaussian distribution, with a standard deviation of 3.99 mm. Random perterbations in the initial liquid positions were applied within the MatLab code to ensure that the simulation reflected these realistic initial conditions. Output from a typical simulation for the 8-channel chip design is provided in Figure 5.13, showing the interfacial liquid radius of curvature vs. pumped volume within each channel, and droplet volume vs. time. The simulation was run with a total applied flow rate of 8.0 μL/min, or a desired flow rate per channel of $Q_d = 1.0$ μL/min. In this particular run, the first and last channels were unable to form droplets.

A plot comparing the iterative model with experimental measurements from an 8-channel chip are shown in Figure 5.14. The experimental measurements were performed using a syringe pump (PHD2000; Harvard Apparatus, Holliston, MA) to deliver DI water through the flow splitter over a range of flow rates from 0.1 to 2.2 μL/min per channel. Error bars indicate standard deviations across 10 measurements for both experimental and simulated data at each applied flow rate. It can be seen that the iterative model provides a good prediction for the minimum flow rate which can be applied before incomplete droplet formation occurs. While there is some deviation in the predicted number of active channels at lower flow rates, the experimental results closely follow the modeled trends. The dashed line in the plot indicates the number of active channels, m, determined from Equation (8) when $P_{co} = 0$. This line represents the lower limit in the number of active

channels at each flow rate. Overall, the results reveal the iterative model as a useful predictive tool for evaluating the number of active channels for any given initial conditions, while the simpler analytic model provides a conservative estimate for acceptable flow rates to ensure that all channels within the array are operational.
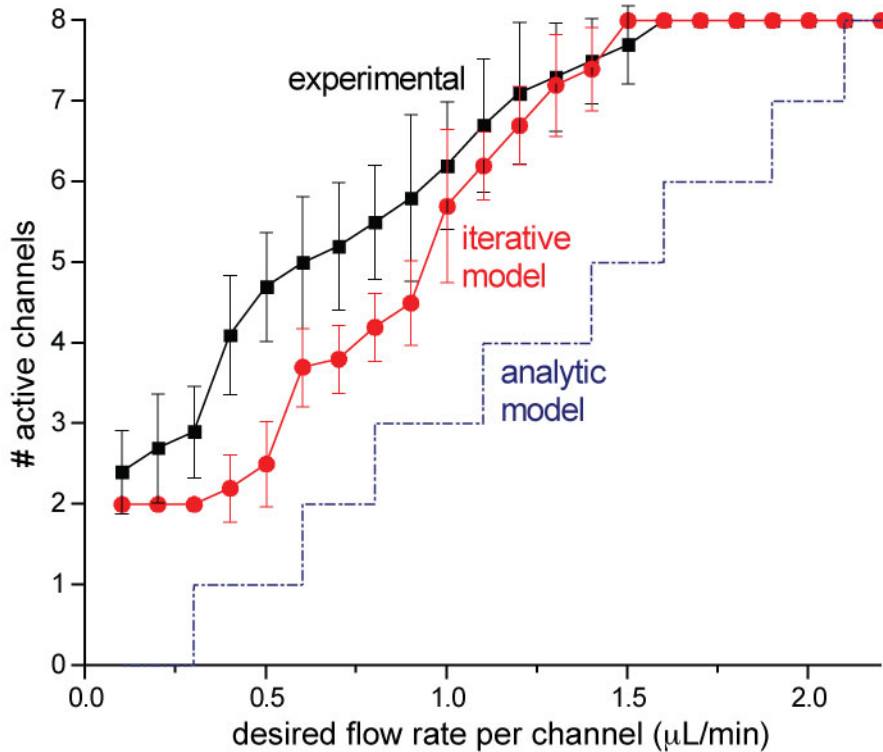
Figure 5.14: Number of channels forming full droplets as a function of desired flow rate per channel, based on numerical simulations and experimental measurements. Each data point represents an average over 10 simulations or measurements. The maximum required flow rate predicted by Eqn. 0 when P_{co} = 0 defines the lower limit.

5.2.3 Droplet Volume Uniformity

A total flow rate of 12 μL/min was imposed by a syringe pump, with a 6 sec interval between each spotting event resulting in a 150 nL theoretical droplet volume for each spot. In practice, due to variations in hydraulic resistance and surface hydrophobicity between each channel in the array, corresponding variations in spotted droplet volumes were observed. At the given flow rate, spotting droplet volumes varied by up to 112%, with an average RSD of 16% between spotting events from individual channels. The measured variability in droplet volumes was expected based on a previously-reported analytic and numerical model of the multichannel spotting process.[135] Tighter control of droplet volume repeatability can be obtained by using higher flow rates, or by increasing the hydraulic resistance of the channels.

Based on the spotting theory presented in section 5.2, one solution for ensuring droplet formation on each channel in a multiplexed array would be to use a defined pressure, rather than a set flow rate, to drive liquid through the channels. In this approach, time varying capillary forces within one channel would not affect flow within other coupled channels since the applied pressure is independent of these forces. However, there are several practical challenges for pressure-based control of multiplexed contact spotting. For many spotting applications, precise control over droplet volume is required. Under pressure control, errors in channel geometry and hydraulic resistance will directly result in errors in flow rate and droplet volume. These errors are not as significant for the case of flow rate control since the hydrodynamic barriers at the channels exits introduce a feedback mechanism which tends to reduce initial variations in liquid

fronts among the channels. In addition, dynamic control of fluid back-pressure can be more challenging than flow rate control due to the need for an integrated force sensor and attendant control electronics, and may be impractical for some applications.

Another approach for improving spotting uniformity is to increase the hydrodynamic flow resistance, Z_f, within each channel. As Z_f increases, the applied pressure required to drive the fluid at a desired flow rate must also increase, thereby reducing the relative impact of variations in the capillary pressure. Hydrodynamic flow resistance may be increased by lengthening the microchannels, or by reducing the channel cross-sectional dimensions. The latter approach is particularly effective, since a smaller effective channel radius produces a large increase in hydrodynamic resistance ($Z_f \propto r_h^{-4}$) with only a linear increase in maximum capillary pressure ($P_{cx} \propto r_h^{-1}$). Since the flow rate limit is proportional to P_{cx}/Z_f, from Equation (10), the limit scales with r_h^{-3}, resulting in a substantial net improvement in spotting uniformity as the hydraulic radius is reduced.

Rather than changing the microchannel dimensions, the hydraulic resistance may instead be increased by integrating a porous medium into the channels. For example, microchannels used for liquid chromatography (LC) typically employ a porous stationary phase consisting of silica beads with diameters on the order of 5-10 μm. When packed into a channel, flow resistance is substantially increased. As an alternative to silica beads, porous monolithic materials are gaining increasing interest as stationary phases in both capillary and planar microfludic LC systems. Following a

methacrylate monolith recipe reported by Frechet et al, [133] a chip was fabricated with a 6 mm long monolith within each of the spotting channels in an 8-channel COC chip.

The monolith was first tested in a single-channel chip, resulting in a measured permeabilty of $\kappa = 5.37 \times 10^{-15}$ m^2. From Darcy's Law,[136] the effective hydraulic resistance for a monolith-filled channel is given by,

$$Z_f = \frac{\mu L}{\kappa A} \tag{11}$$

Comparing Equations (4) and (11), together with Equation (1), the monolith-filled channels in the test chip require an applied pressure $>10^4$ times higher to generate flow rates equivalent to the unfilled channels. As a result, the microchannel arrays containing monoliths could be consistently operated at flow rates as low as 100 nL/min per channel (800 nL/min total flow rate), with droplet formation obeserved from all channels in the array. Lower flow rates were not measured, since evaporation of the exposed droplets limited the ability to collect reliable data.

To further demonstrate the effect of higher hydraulic resistance on droplet formation, a syringe pump was used to deliver water at a total flow rate of 12 µL/min through two chips, one with and one without the 6 mm long monoliths. A robotic system was used to generate a sequence of spotting events from each of the 8 channels onto a stainless steel plate, with a 6 second interval between events for an anticipated droplet volume of 150 nL. As revealed in Figure 5.15, the

average spotting volume between each of the 8 channels varied substantially for the chip without monoliths, with a coefficient of variation (CV) up to 34.7% for multiple droplets from a single channel, and up to 25.2% across all 8 channels. In contrast, droplet volumes from the monolith-filled channels exhibited maximum CVs of only 12.9% and 7.0% from a single channel and across all channels, respectively.
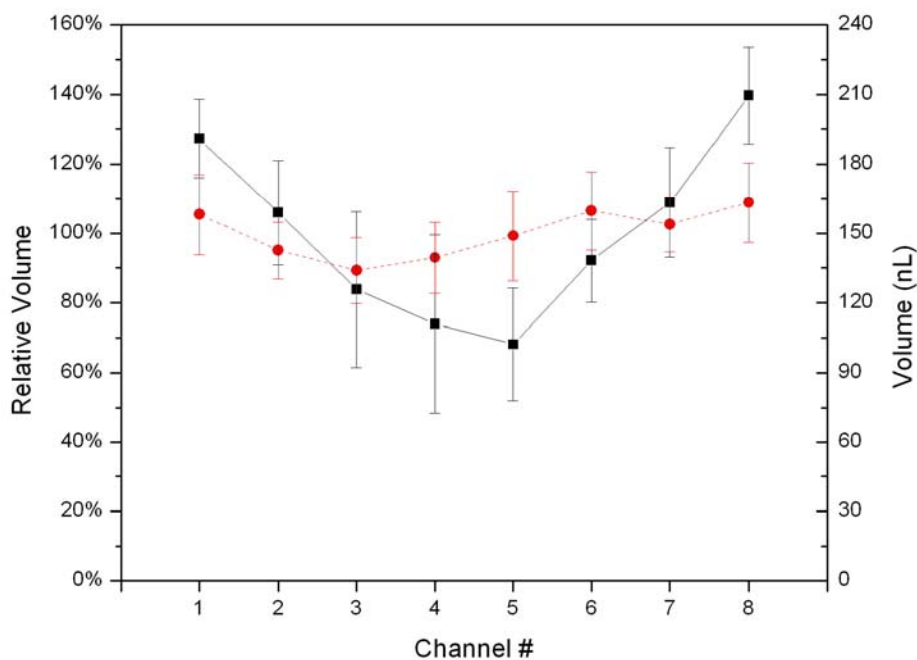
Figure 5.15: Deposited spot volumes across 7 sequential spotting events from 8 parallel channels with (dashed line) and without (solid line) monoliths. The monolith-filled channels exhibit improved droplet reproducibility due to the higher hydraulic resistance of the monolith.

5.2.4 MALDI-MS Uniformity

Sample preparation

Sampe preparation for MALDI-MS plays an important role in determining good mass spectral data quality. The matrix solution use in this reasech is 50 % of Acetonitrile (Fishser Scientifics, Pittsburgh, PA), 40 % of DI Water and 10 % acetic acid (J.T.Baker,Phillipsburg, NJ) mix with 10 μg/μL α-cyano-4-hydroxycinnamic acid (CHCA) (Sigma-Aldrich,St. Louis, MO). MassPREP peptide sample was purchased from Waters Corporation (Milford, MA) and the MassPREP Peptide Mixture contains 9 peptide samples with 1nmol of each peptide. (MW:1000.4938 - RASG-1, MW:898.4661 - Amgiotensin frag.1-7, MW:1045.5345 - Angiotensin II, MW:1059.5613 – Bradykinin, MW:1295.6775 - Angiotensin I, MW:1757.9253 - Renin Substrate, MW:1871.9604 - Enolase T35, MW:2827.2806- Enolase T37, MW:2845.7381- Melittin). The lyophilized powder peptide sample was resconstituted with 0.1% aquaous trifluoroacetic acid (TFA) solution (Acros Organics, Morris Plains, NJ) to have 1pmol/ul concentration. Then premix with matrix solution in ratio of 1:1 by volume as matrix solution.

Mass spectrometry measurment

MALDI-MS measurements were performed on a Kratos Amixa time-of-flight (TOF) mass spectrometer (Kratos Analytical, Manchester, UK). All MALDI-MS spectra were acquired in linear, positive ion mode using between 25 and 50 laser pulses from a 337 nm nitrogen laser with a 3 ns pulse width. Laser power of 130 μJ/plus was optimized based on signal-to-noise ratio using a test sample spot, and

held constant during all experiments. The resulting spectra showed good uniformity, with an average RSD of 44% across all peptides. This compares well with an RSD of 50% in MALDI signal intensities reported for multiple peptide spots deposited from a single capillary using an optimized matrix seed layer technique.[137] Further improvements in deposition volume uniformity were realized for an 8-channel chip containing a methacrylate monolith developed for reversed phase chromatography in the second separation dimension, with negligible variations at flow rates down to 100 nL/min per channel.

Except for the m/z value at,1000.5 (RASG-1) presents low signal intensity with signal-to-noise ratio (S/N) less than 3 for peptide identification, MALDI-MS spectra acquired from the 64 sample spots provided repeatable identification for 8 of the 9 model peptides for all spotting events. Figure 5.16 shows the mass spectra from all 8 channels during a single spotting event. Good MALDI-MS signal uniformity was observed across all 64 spots, with an average RSD of 44% across all 64 spots for all peptides. This compares favorably with an RSD of 50% in MALDI-MS signal intensities reported for multiple peptide spots generated by sequential depositions from a single capillary using an optimized matrix seed layer technique.[137]

With an approximate deposition volume of 100~210 nL per spot across 64 spot events, corresponding to sample amounts ranging from 50-105 fmol for each of 9 model peptides leaving on the gold anchor. Figure 5.16 shows the mass spectra of channel 1 to channel 8 in a signal spot raw which can indenty all nigh peptides from mass range 500-4000.
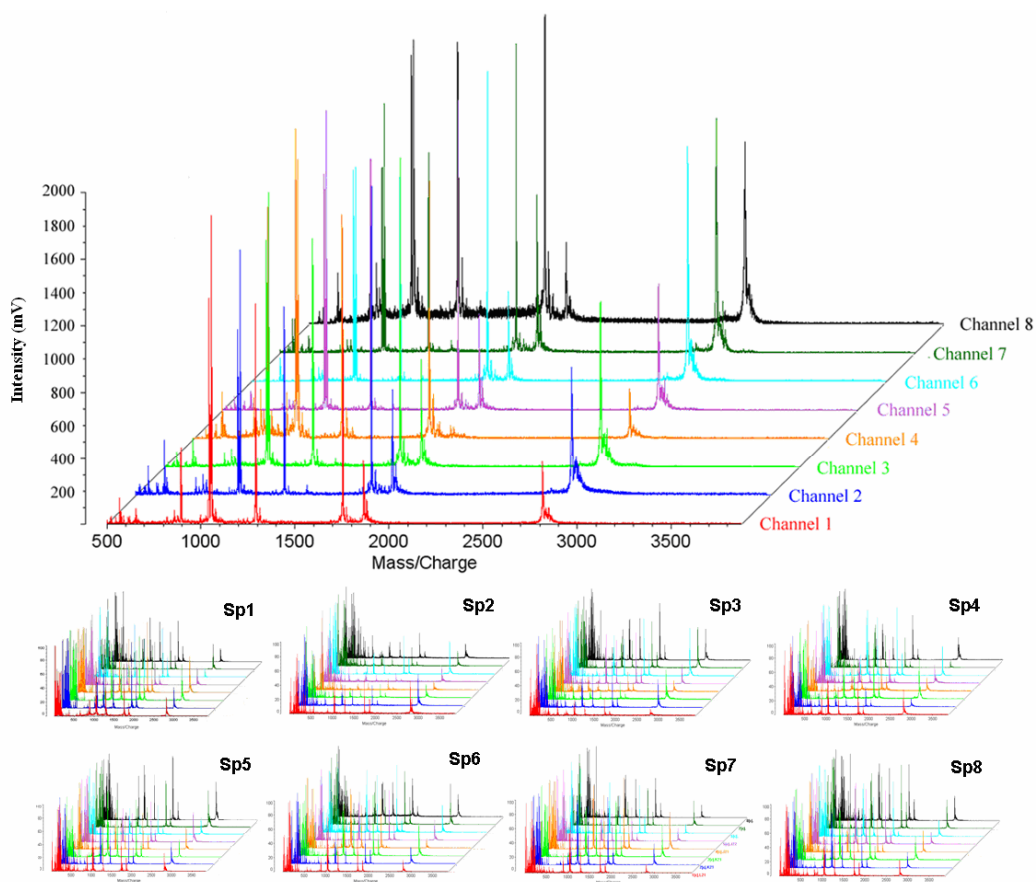
Figure 5.16: MALDI-MS spectra for sample deposited from all 8 channels during a single spotting event

Uniformity of deposited spot volume and MALDI-MS signal intensities evaluated. In Figure 5.17, the signal intensities are averaged over all peptides in both plots. In Figure 5.17(a), it shows the intensity between different spotting events averaged over all channels with maximum 58% relative standard deviation and Figure 5.17(b) represents between different channels averaged over all spotting events with maximum 52% relative standard deviation.
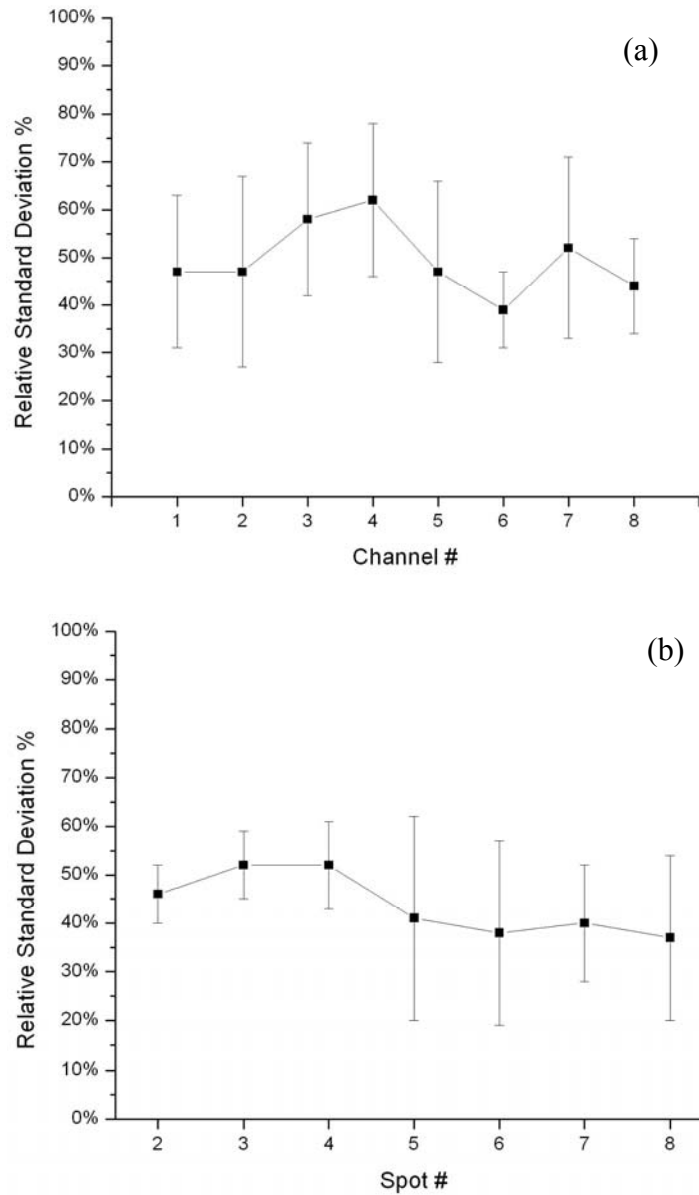
Figure 5.17: Uniformity of MALDI-MS signal (a) between different spotting events averaged over all channels, and (b) between different channels averaged over all spotting events.

5.3 Liquid Chromatography / nSi LDI-MS Interfacing

The key to achieving highly repeatable droplet generation from the 8-channel spotting chip was to integrated monoliths into the spotting channels, thereby reducing the effects of capillary forces on the relative flow rates among the channels within the array. This fact makes the spotting approach attractive for multiplexed RPLC separations, since monoliths can provide excellent stationary phases for a range of chromatographic separations, including RPLC. In this section, unlike the previous MALDI-MS characterization results which were generated using a traditional stainless steel MALDI target during deposition and analysis, the RPLC separations were interfaced with a nanofilament silicon (nSi) target which eliminates the need for organic matrix to be added to the sample.

5.3.1 LC/MS Microfluidic Chip Preparation

Materials and reagents

Butyl methacrylate (BMA, 99%), ethylene dimethacrylate (EDMA, 99%), ethylene diacrylate (EDA, 90%), methyl methacrylate (MMA, 99%), 1,4-butanediol (99%), 1-propanol ($\geq$ 99.5%), cyclohexane (99%), acetonitrile (ACN, reagent grade), 2,2'-dimethoxy-2-phenylacetophenone (DMPA, 99%), benzophenone (BP, 99%), DL-dithiothreitol (DTT, electrophoresis grade), fluorescein isothiocyanate isomer I (FITC, 98%), bovine serum albumin (BSA, 96%), neurotensin (98%), bradykinin acetate (98%), [leu[5]]-enkephalin (96%), and angiotensin II acetate were purchased from Sigma-Aldrich (St. Louis, MO). Trypsin Gold (mass spectrometry grade) was

ordered from Promega (Madison, WI). Methanol, HPLC water, and rhodamine B (RhB, 99+%) were obtained from Fisher Scientific (Pittsburg, PA). Urea, acetic acid, sodium carbonate, and sodium bicarbonate were ordered from J. T. Baker (Phillipsburg, NJ). Trimethylolpropane trimethacrylate (TMPTMA) was received as a free sample from Sartomer (Warrington, PA). Cyclic olefin copolymer (COC), Zeonor 1020R COC substrate was purchased from Zeon Chemicals. (Louisville, KY)

Chip fabrication

The LC/MS COC chip design used in this work was shown in Figure 5.19. The COC chip consists of two injection channels for different consistence buffer injection, and serpentine separation channel regulated with "double-T" cross-injector to control precise sample loading. Each channel was nominally 100 μm wide and 46 μm deep, with geometric variances of less than 1.5% measured across all channels prior to chip bonding. The overall microchannel network was 150 mm long from input port to spotting tips. Chip fabrication employed thermal embossing from a silicon master template and solvent bonding using procedures identical to previously-reported process. After solvent bonding, the chip was cut to expose the fluid exit points using a semiconductor wafer dicing saw (DAD321, Disco Hi-Tec America, Santa Clara, CA) using a Disco SDC320R11B dicing blade and insert a surgical stainless steel needle as high pressure-resistance, low dead-volume interconnections.

Preparation of reverse phase monolith in COC HPLC microchip

The COC channel surface was functionalized using a photografting method [133] to provide an anchoring layer for monolithic stationary phase. Briefly, the COC channel was first thoroughly rinsed with methanol, dried in the vacuum oven at room temperature, and filled with a reaction solution containing 49.5 wt% EDA, 49.5 wt% MMA, and 1.0 wt% BP, which has been sonicated for 30 min. The device was then exposed to UV generated from a PRX-1000 UV source (Tamarack Scientific, Corona, CA) with a radiation power of 24.0 mW/cm^2 for 630 s. Followed UV grafting, the channel was again rinsed with methanol and dried in the vacuum oven. The reversed-phase monolithic stationary phase was synthesized using a photolithography-like method. First, a reaction solution containing 24.5 wt% BMA, 14.5 wt% TMPTMA, 30.0 wt% 1-propanol, 30.0 wt% 1,4-butanediol, and 1.0 wt% DMPA was degassed using 30-min sonication and then introduced to the surface-treated COC channel. To selectively photopolymerize the solution in the separation channel, the entire channel except for the separation channel section was covered with a photomask. After 240s UV exposure using the PRX-1000 UV source, the resulting 15cm long monolith was rinsed with methanol at 1 µl/min for 12 h before use. The SEM image of BMA-TMPTMA monolith shown in Figure 5.18 reveals a porous structure of a typical BMA-containing RP polymethacrylate monolith. The BMA-TMPTMA monolith is consisted of numerous clusters of fused globules with diameters smaller than 1 µm, while the globular clusters pile up to form many large irregular through-pores. The magnified view of the SEM image also clearly indicates that the monolith is covalently bonded to the COC channel surface, which prevents the movement of the

whole section of monolith under high pressure, and leakage of analytes through the gap forming between the wall and the monolith.
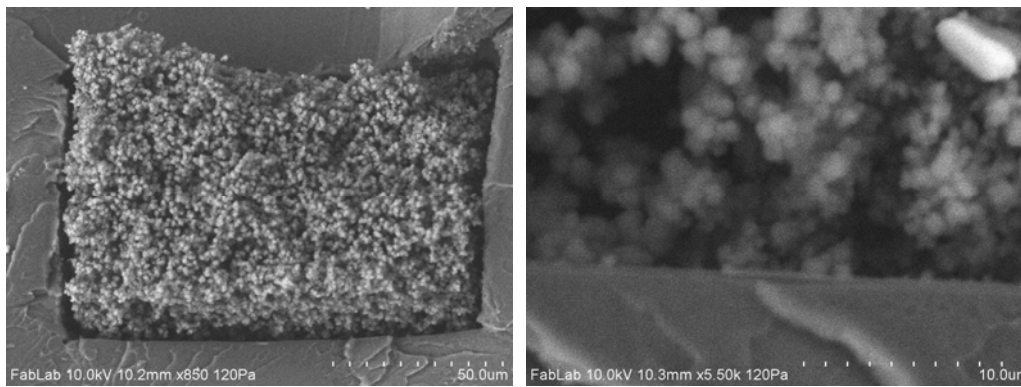
Figure 5.18: SEM images of TMPTMA monolith.

Preparation of FITC-labeled peptide samples

Each model peptide was dissolved in 10 mM sodium carbonate/bicarbonate buffer (pH 9.0) to a concentration of 2 mM, and then 200 μL of each 2 mM peptide solution was mixed with 50 μL 6 mM FITC acetone solution. FITC-labeled BSA tryptic digest was prepared by mixing 150 μL 6 mM FITC acetone solution with 600 μL BSA tryptic digest solution. The labeling reaction was allowed to proceed in dark for 24 h. The model peptide sample was prepared by mixing equal volume of labeled peptide solutions and then diluting 5 folds with HPLC water. FITC-labeled BSA tryptic digest sample was diluted 3 folds with HPLC water before being injected to the HPLC microchip.

5.3.2 Liquid Chromatography Separation and Mass Spectrometry Interfacing

An on-line double-T channel junction microchannel design was fabricated on the LC/MS chip. Compare with the off-line injection methods[126, 130, 138, 139], this on-chip injection design significantly reduces the dead volume and band broadening during sample injection process. The LC/MS chip design and experiment setup were shown in Figure 5.19. 360 µm outer diameter and 100 µm inner diameter silica capillary section was used to connect the microchip to external pumps and valves. A 50 cm long capillary was connected to the sample waste port as a splitter. The total length of connecting capillary sections extending from the sample injection port to waste A was also 50 cm, which served as the second splitter during separation.

During sample injection, the 6-way selection Upchurch valve was set at position 1 and sample was injected to the microchip at a flow rate of 4 µL/min using a PHD-2000 syringe pump (Harvard Apparatus, Holliston, MA). Water was simultaneously pumped to the microchip at a flow rate of 15 µL/min using a PU-2089 analytical LC pump (Jasco, Easton, MD). The sample was diverted to the head space of the separation channel and stacked at the front end of the porous monolith in the double-T microchannel. Immediately after the sample was injected, the selection valve was switched to position 3 and residual sample inside channels was flushed to waste containers, which prevented sample leaking from the side channels during separation. In separation procedure, a linear ACN gradient was delivered to the LC/MS chip from the LC pump to elute and separate the sample stacked at the head column. The master flow rate of LC pump was set at 1 to 2 mL/min and the flow rate in the monolithic

column was 200-500 nL/min. During separation, the double-T channels together with the connecting capillaries served as two passive splitters to shunt a specific portion of mobile phase to waste, thus maintaining the desired flow rate in the separation channel. Control of split ratios can be readily achieved by selecting different capillaries lengths and diameters.
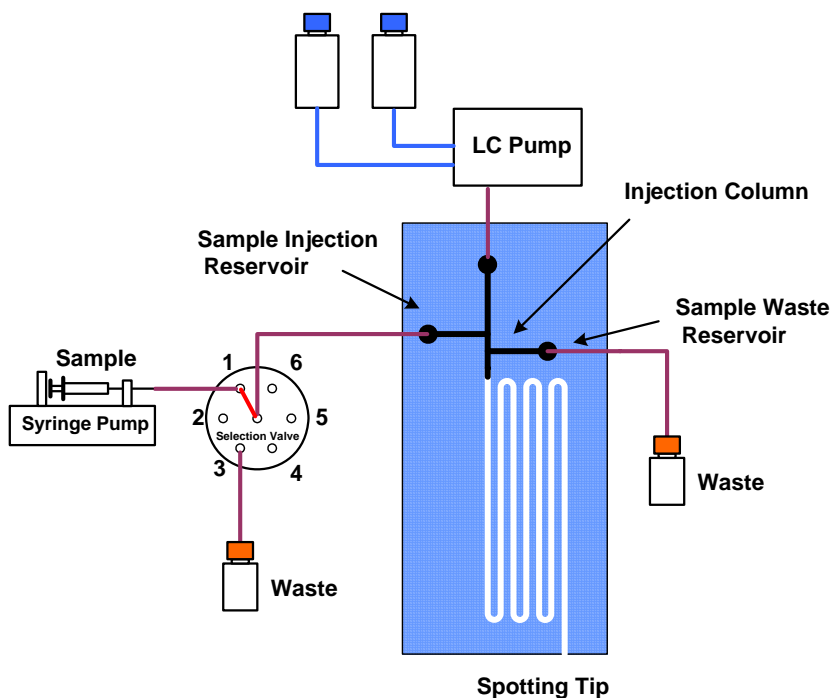
Figure 5.19: LC/MS chip design and experiment setup

H_2O

RPLC separation of peptide samples

The FITC-labeled bands are detected by TE-2000 S inverted epi-fluorescence microscope (Nikon, Melville, NY) and chromatograms were obtained using Nikon Element image analysis software. In the separation test, a mixture containing 4 FITC-labeled model peptides, [leu^5]-enkephalin, bradykinin, angiotensin II and neurotensin,

was injected to the HPLC microchip. The chromatogram was shown in Figure 5.20, complete separation of all the peptides on the 15cm long TMPTMA monolith was achieved using a solvent gradient with a rate of 1% ACN/min which identify of Peak identities: 1, FITC; 2, FITC labeled angiotensin II; 3, FITC labeled [leu[5]]-enkephalin; 4, FITC labeled neurotensin; and 5, FITC labeled bradykinin. ACN concentration was changed from 5% to 20% in 15 min, form 20% to 50% acetonitrile in 5 min and keeps 50% acetonitrile afterwards during separation. The master flow rate was 1.5 mL/min and injection time was 40s
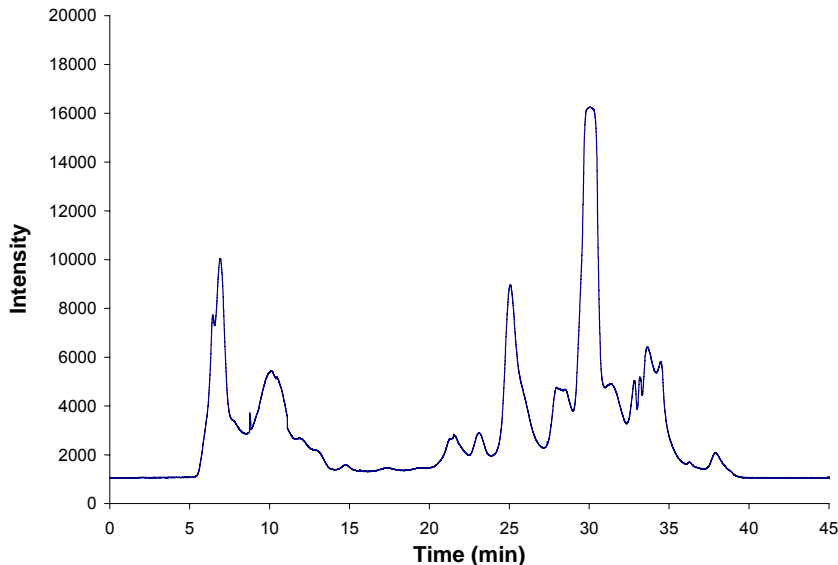
Figure 5.20: RPLC separation of a mixture of 4 FITC labeled model peptides on COC chip

Microfluidic chip LC/ nSi MS interfacing by robotic spotting

The mass spectrometry measurement of FITC-labeled peptide mixture prior to microfluidic chip separation was shown in Figure 5.21. It shows identification of [leu[5]]-enkephalin (MW:555.62), FITC labeled [leu[5]]-enkephalin (MW:945.0), angiotensin II (MW: 1046.18), bradykinin (MW: 1060.61), FITC labeled angiotensin

138

II(MW: 1435.56), FITC labeled bradykinin (MW: 1449.99), neurotensin (MW: 1672.92) , and FITC labeled neurotensin (MW: 2061.38) at 500~2300 m/z range.
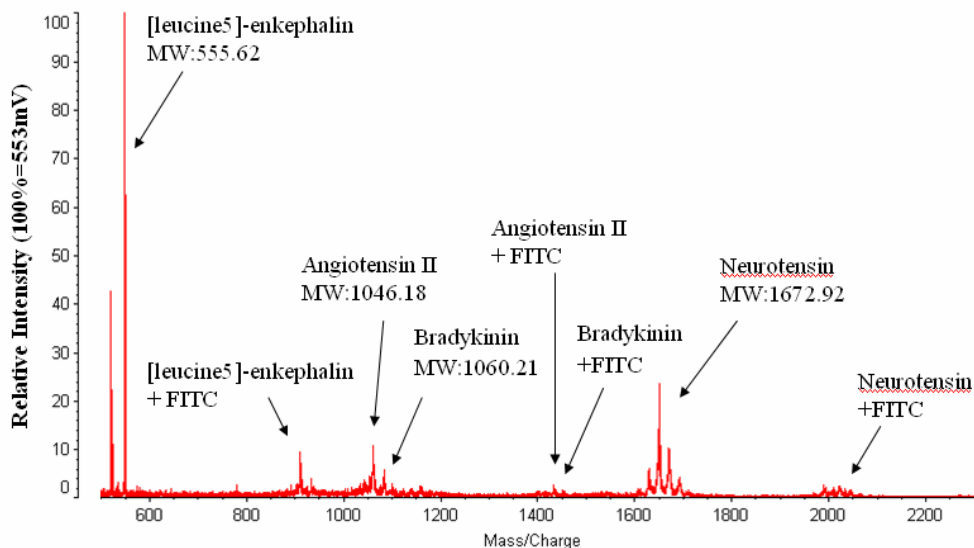
Figure 5.21: nSi LDI-MS spectra of FTIC labeled peptide mixtures

The RPLC separation microfluidic chip was interfacing with nSi LDI-MS by using automatic robotic spotting system to demonstrate microfluidic chip separation / high sensitivity matrix-free nSi LDI-MS interfacing capability. The LC microfluidic chip was setup in the robotic spotting system as described in chapter 5.1, automatic spotting was performed by moving the chip 200 μm from the target surface to transfer droplets to the nanofilament substrate, then returning to the initial 2 mm gap and indexing the stage for the next spot. The robotic spotting system transfer 20 ~500 μm diameter of eluting droplets from LC microfluidic chip onto the nSi substrate with 2 min spotting time interval at total 40min spotting time. The microfluidic chip separated droplets numbered #1 to #20 was transfer to Kratos Amixa time-of-flight (TOF) mass spectrometer (Kratos Analytical, Manchester, UK) for MS analysis. The

laser energy was adjusted for maximum S/N prior to each test to collected mass spectral data using Kompact software version 2.3.4 (Kratos Analytical). The resulting mass spectra measured from each of the 20 deposited spots were shown in Figure 5.22. Each of the sample peptides was observed in specific fractions deposited on the nSi surface, with [leu5]-enkephalin identified from spots #2 and #3, angiotensin II from spot #5 and bradykinin and neurotensin together from spot #10. The co-elution of [leu5]-enkephalin across two adjacent fractions indicates a relatively large bandwidth for this peptide, while the simultaneous elution of bradykinin and neurotensin within a single fraction suggests that more fractions should be sampled to fully resolve these components with similar hydrophobicity.
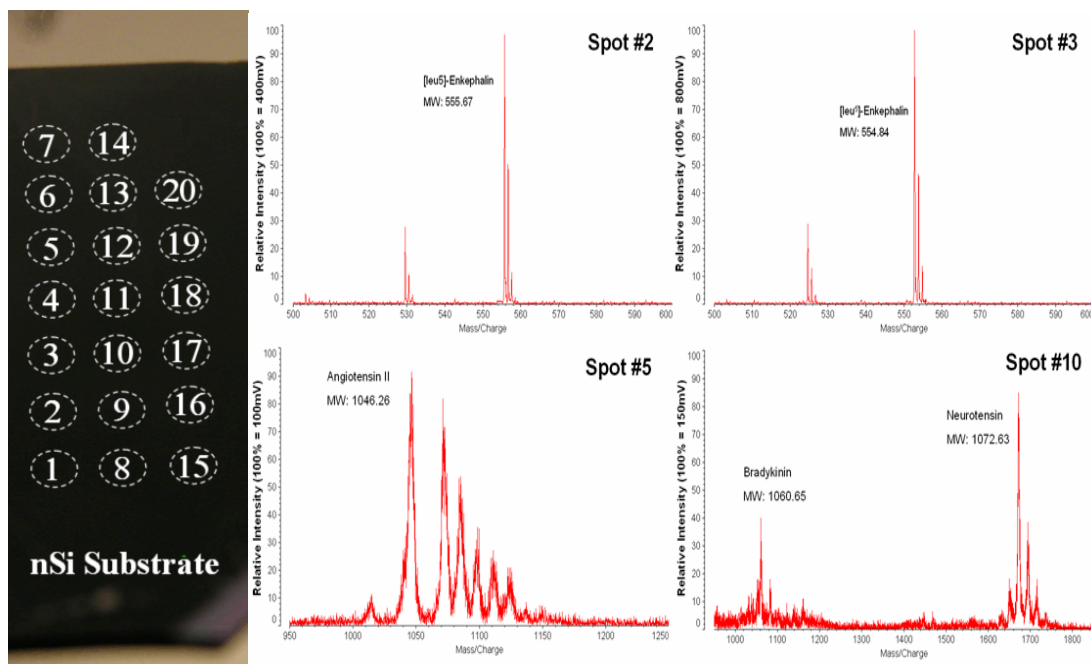
Figure 5.22: LC/MS interfacing using robotic system

5.4 Conclusion

Automated contact spotting is an exceptionally simple and robust approach for coupling microfluidic separations to off-line LDI-MS mass spectrometry. Spotting from multiplexed arrays of parallel microchannels revealed good uniformity in both droplet volume and MALDI-MS signal intensity across all channels and multiple spotting events, while spotting from a single separation channel onto an nSi LDI-MS target demonstrated that hydrodynamic contact spotting may be effectively coupled with microfluidic RPLC separations. Further work to demonstrate parallel RPLC interfaced to nSi LDI-MS as an approach to high-throughput bioanalysis leveraging the unique benefits of microfluidic technology is ongoing.

Chapter 6 Conclusions and Future Work

6.1 Conclusion

The main objective in this dissertation is to develop automatic, high throughput polymer microfluidic / mass spectrometry interfacing platform for bioanalysis. The research work in this dissertation involves (I) develop polymer microfabrication technique including polymer replica techniques and UV/Ozone bonding technique, (II) develop nano-scale filament silicon surface called nanofilament silicon (nSi) and its electrowetting behavior for high sensitivity matrix-free laser desorption/ionization mass spectrometry application and (III) develop microfluidic / mass spectrometry interfacing technique by contact spotting method. Each subject is summarized in the following:

6.1.1 UV/Ozone Bonding

The use of UV/ozone surface treatments for achieving low temperature bonds between PMMA and COC microfluidic substrates is evaluated. Low temperature bond strengths approaching those of native polymer substrates bonded above their glass transition temperatures are demonstrated for both thermoplastics. To evaluate the effects of the UV/O_3 surface treatment on the operation of bonded microfluidic devices, the relationship between UV/O_3 exposure and polymer hydrophilicity and surface chemistry are measured. Post-treatment surface chemistry is evaluated by XPS analysis, and the stability of the

treated surfaces following solvent exposure is reported. Electroosmotic flow within fabricated microchannels with modified wall surfaces is also characterized. Overall, UV/O$_3$ treatment is found to enable strong low temperature bonds between thermoplastic microfluidic substrates using a simple, low cost, and high throughput fabrication technology

6.1.2 Nanofilament Substrate (nSi) and Electrowetting on nSi

Dynamic electrowetting on nanostructured silicon surfaces is demonstrated as a effective method for improving detection sensitivity in matrix-free laser desorption/ionization mass spectrometry. Without electrowetting, silicon surfaces comprising dense fields of oriented nanofilaments are shown to provide efficient ion generation and high spectral peak intensities for deposited peptides bound to the nanofilaments through hydrophobic interactions. By applying an electrical bias to the silicon substrate, the surface energy of the oxidized nanofilaments can be dynamically controlled by electrowetting, thereby allowing aqueous buffer to penetrate deep into the nanofilament matrix. The use of electrowetting is shown to result in enhanced interactions between deposited peptides and the nanofilament silicon surface, with improved signal-to-noise ratio for detected spectral peaks. An essential feature contributing to the observed performance enhancement is the open-cell nature of the nanofilament surfaces, which prevents air from becoming trapped within the pores and limiting solvent penetration during electrowetting. The combination of nanofilament silicon and dynamic electrowetting is shown to provide routine detection limits on the order of several attomole for a panel of model peptides.

6.1.3 Mass Spectrometry Interfacing by Robotic Spotting System

Direct and automated spotting of analyte from multichannel microfluidic chips is demonstrated as a simple, robust, and high-throughput method for interfacing arrays of parallel microchannels with matrix-assisted laser desorption/ionization mass spectrometry (MALDI-MS). Using cyclic olefin copolymer (COC) chips containing 8 parallel 100 μm x 46 μm channels connected to a single input port, excellent spotting volume repeatability and MALDI-MS signal uniformity are achieved for a panel of sample peptides. Using the robotic spotting approach, chip-based reversed-phase liquid chromatography (RPLC) separations are interfaced with nanofilament silicon (nSi) LDI-MS, demonstrating the potential for this approach towards high-throughput on-chip bioanalysis coupled seamlessly with back-end mass spectrometry.

6.2 Significant Contributions

The research in the dissertation shows novel polymer microfluidic interfacing with nSi LDI-MS technology. The significant contributions from this dissertation are:

- Development of novel polymer microfluidic device fabrication technology
- Development of low temperature polymer bonding technique by using UV/Ozone treatment
- Development of novel matrix-free laser desorption/ionization on silicon substrate, nanofilament silicon (nSi), for high sensitivity mass spectrometry application

- Development of multiplexed microfluidics - mass spectrometry (MALDI-MS) interfacing technique using high throughput robotic spotting system

- Demonstrate of microfluidic liquid chromatography (RPLC) separation interfacing with nanofilament silicon (nSi) by robotic system

6.3 Recommendation of Future Works

Eliminate noise background below m/z 500 for small molecule detection

In this dissertation, LDI-MS on nSi surface was successfully demonstrated as a high-sensitivity matrix-free mass spectrometry analysis approach. The nSi surface shows great promise to eliminate the use of organic matrix for mass spectrometry analysis to analysis small molecules without matrix noise background. However, the mass spectrometry test result using Kratos Amixa time-of-flight (TOF) mass spectrometer (Kratos Analytical, Manchester, UK) observed high background noise below m/z 500 range. Possible noise background sources may come from the sample, nanofilament substrate and MADLI-TOF mass spectrometer. Rigorous organic solvent, weak acid rinse cleaning prior and post sample deposition to eliminate the possible contamination from nSi surface have been performed and the test results show no significant improvement to eliminate the backgrounds peaks below m/z 500. Another mass spectrometry test run using BRUKER Autoflex TOF/TOF mass spectrometer (Bruker BioSciences Corporation, Fremont, CA) at John Hopkins Apply Physics Lab (APL) was also performed. The resulting mass spectra presented in Figure 6.1 shows only four peaks below m/z 500 value without other background noise. The mass spectra provides identification of Sodium in MW 23, Potassium in

MW 39, a unknown peak in MW 74 and the dicrotophos sample + sodium ion in MW 263. Thus, the possible contamination source may come from the Kratos Amixa time-of-flight (TOF) mass spectrometer.
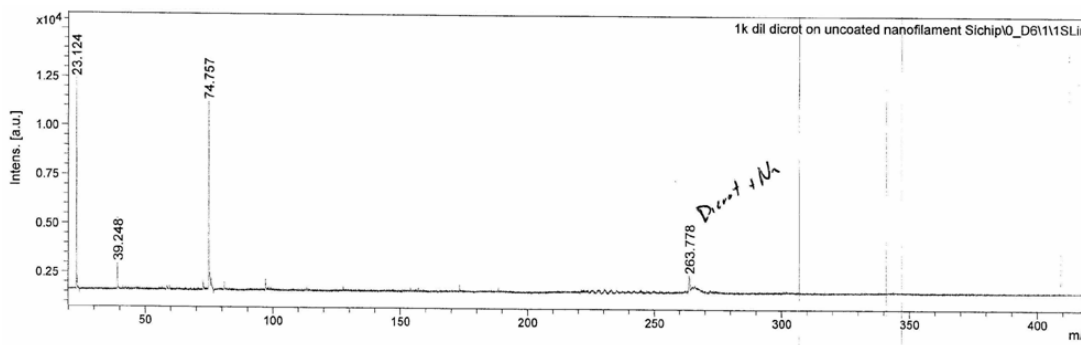
Figure 6.1: Mass spectrometry analysis result using BRUKER Autoflex TOF/TOF mass spectrometer in John Hopkins Apply Physics Lab

With elimination of noise background at low m/z value, the high sensitivity matrix-free nSi LDI-MS is ideal for various kind of application like explosive detection due to its advantages of no matrix background to detect small molecule sample and high sensitivity to detect at low sample loading. Research of using nanofilament silicon to detect the explosives components such as trinitrohexahydro-1,3,5-triazine (RDX), octahydro-1,3,5,7-tetranitro-1,3,5,7-tetrazocine (HMX), 2,4,6-trinitrotoluene (TNT) and Pentaerythritol tetranitrate (PETN) are in progress.

Hydrophobic coating on COC surface

Using Teflon AF coating to create hydrophobic exit surface encourages easier droplet transfer from COC microfluidics chip to the target substrate. And it have been successfully demonstrated complete transferring 8x8 150nL droplets from 8 channel multiplexed microfluidic chip to MALDI target plate as presented in chapter 5.

However, baking of Teflon AF at high temperature (> 165°C) are usually recommended [107] to give smoother coating and improved surface adhesion. In order to prevent heating COC chip about its Tg casing distortion of microchannels, low-temperature baked Teflon AF layer is used in this dissertation. The resulting life time of low-temperature baked Teflon AF layer have been tested for more than 200 spotting runs using DI water and more than 50 runs using acetonitrile solution. Researches of permanent hydrophobic coating on COC surface are encouraged to have long microfluidic chip lifetime for better and reliable droplet transfer to target plate.

Multidimensional microfluidic separation / mass spectrometry interfacing

This dissertation demonstrates microfluidic chip-based one dimension reverse phase liquid chromatography (RPLC) separation coupling with nanofilament silicon mass spectrometry. The microfluidic systems provide benefit for multidimensional separations in a single integrated system, which was demonstrated by Li et al [121] in year of 2004 from our group. The robotic system presented in this dissertation can further integrated with two dimension separation microfluidic chip. Assuming the separation techniques used in the two dimensions are orthogonal, the peak capacity of two-dimensional (2-D) separation is the product of the peak capacities of individual one-dimensional methods. By coupling with mass spectrometry, this approach can be employed for the analysis of complex mixtures.

An integrated 2-D separation polymer microfluidic device with isoelectric focusing (IEF) and SDS gel electrophoresis has been reported by Li *et al*.[121] This

2-D microfluidic chip provides a simple and high-throughput approach transferring focused bands into second separation dimension without significant sample and resolution loss during transferring by staggered configuration as shown in Figure 6.2(a) and a schematic of the chip design is shown in Figure 6.2(b). Instead of sequentially sampling protein analytes eluted from IEF, focused bands are transferred into an array of orthogonal microchannels and further resolved by SDS gel electrophoresis in parallel.

(a)

(b)
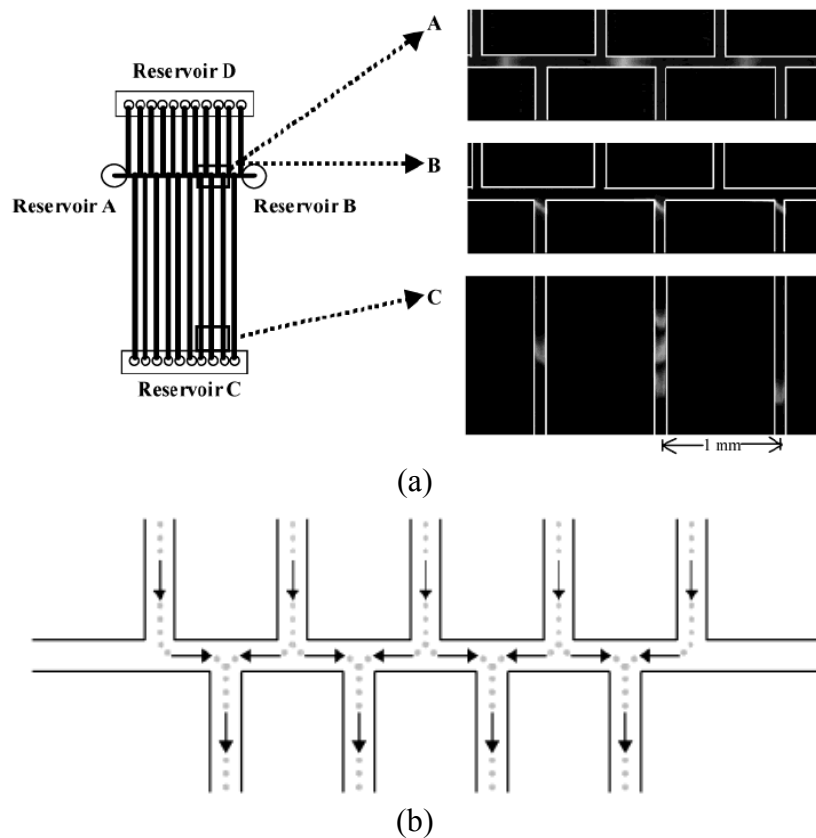
Figure 6.2: Schematic presentation of (a) 2D separation (IEF/CGE) microfluidic chip and (b) it showing flow paths during sample transfer between the 1st and 2nd dimensions [121]

The IEF/RPLC/MS design concept was shown in Figure 6.3, the protein samples are introduced into the single IEF channel and separated by isoelectric focusing (IEF) as first dimension separation. A commercially available LC pump is connected to the splitter network inlet to deliver equal flow rate and transfer the focused bands into the multiplexed RPLC channel. The RPLC separation will perform parallel as a high-through format. At the end of the RPLC channel, a RPLC/MS spotting interface was created to transfer separated bands to nanofilament silicon (nSi) or conventional MALDI target plate for off-line mass spectrometry analysis using robotic spotting system.
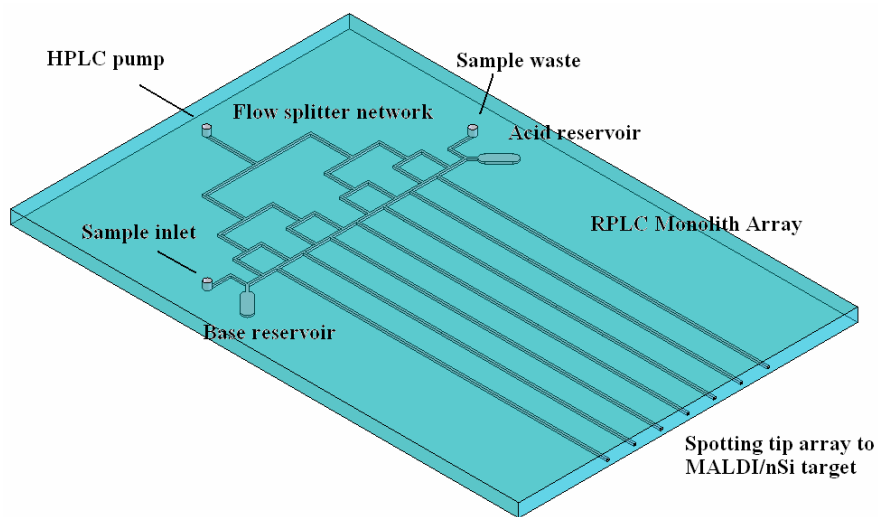
Figure 6.3: IEF/RPLC/MS microfluidic chip

Bibliography

1.   Manz, A., N. Graber, and H.M. Widmer, *Miniaturized Total Chemical-Analysis Systems - a Novel Concept for Chemical Sensing.* Sensors and Actuators B-Chemical, 1990. **1**(1-6): p. 244-248.

2.   Figeys, D. and D. Pinto, *Proteomics on a chip: Promising developments.* Electrophoresis, 2001. **22**(2): p. 208-216.

3.   Lion, N., et al., *Microfluidic systems in proteomics.* Electrophoresis, 2003. **24**(21): p. 3533-3562.

4.   Freire, S.L.S. and A.R. Wheeler, *Proteome-on-a-chip: Mirage, or on the horizon?* Lab on a Chip, 2006. **6**(11): p. 1415-1423.

5.   Xue, Q.F., et al., *Multichannel microchip electrospray mass spectrometry.* Analytical Chemistry, 1997. **69**(3): p. 426-430.

6.   Ramsey, R.S. and J.M. Ramsey, *Generating electrospray from microchip devices using electroosmotic pumping.* Analytical Chemistry, 1997. **69**(6): p. 1174-1178.

7.   Lazar, I.M., et al., *Subattomole-sensitivity microchip nanoelectrospray source with time-of-flight mass spectrometry detection.* Analytical Chemistry, 1999. **71**(17): p. 3627-3631.

8.   Chan, J.H., et al., *Microfabricated polymer devices for automated sample delivery of peptides for analysis by electrospray ionization tandem mass spectrometry.* Analytical Chemistry, 1999. **71**(20): p. 4437-4444.

9.   Pinto, D.M., Y.B. Ning, and D. Figeys, *An enhanced microfluidic chip coupled to an electrospray Qstar mass spectrometer for protein identification.* Electrophoresis, 2000. **21**(1): p. 181-190.

10.   Zhang, B.L., F. Foret, and B.L. Karger, *High-throughput microfabricated CE/ESI-MS: Automated sampling from a microwell plate.* Analytical Chemistry, 2001. **73**(11): p. 2675-2681.

11.   Wang, Y.X., et al., *Efficient electrospray ionization from polymer microchannels using integrated hydrophobic membranes.* Lab on a Chip, 2004. **4**(4): p. 363-367.

12.   Yin, N.F., et al., *Microfluidic chip for peptide analysis with an integrated HPLC column, sample enrichment column, and nanoelectrospray tip.* Analytical Chemistry, 2005. **77**(2): p. 527-533.

13.   Schilling, M., et al., *A new on-chip ESI nozzle for coupling of MS with microfluidic devices.* Lab on a Chip, 2004. **4**(3): p. 220-224.

14.   Dahlin, A.P., et al., *Capillary electrophoresis coupled to mass spectrometry from a polymer modified poly(dimethylsiloxane) microchip with an integrated graphite electrospray tip.* Analyst, 2005. **130**(2): p. 193-199.

15.   Musyimi, H.K., et al., *Direct coupling of polymer-based microchip electrophoresis to online MALDI-MS using a rotating ball inlet.* Electrophoresis, 2005. **26**(24): p. 4703-4710.

16. Brivio, M., et al., *A MALDI-chip integrated system with a monitoring window.* Lab on a Chip, 2005. **5**(4): p. 378-381.

17. Ekstrom, S., et al., *Signal amplification using "spot on-a-chip" technology for the identification of proteins via MALDI-TOF MS.* Analytical Chemistry, 2001. **73**(2): p. 214-219.

18. Laurell, T., J. Nilsson, and G. Marko-Varga, *Silicon microstructures for high-speed and high-sensitivity protein identifications.* Journal of Chromatography B-Analytical Technologies in the Biomedical and Life Sciences, 2001. **752**(2): p. 217-232.

19. Wang, Y.X., et al., *Electrospray interfacing of polymer microfluidics to MALDI-MS.* Electrophoresis, 2005. **26**(19): p. 3631-3640.

20. Wheeler, A.R., et al., *Digital microfluidics with in-line sample purification for proteomics analyses with MALDI-MS.* Analytical Chemistry, 2005. **77**(2): p. 534-540.

21. Moon, H., et al., *An integrated digital microfluidic chip for multiplexed proteomic sample preparation and analysis by MALDI-MS.* Lab on a Chip, 2006. **6**(9): p. 1213-1219.

22. Wheeler, A.R., et al., *Electrowetting-based microfluidics for analysis of peptides and proteins by matrix-assisted laser desorption/ionization mass spectrometry.* Analytical Chemistry, 2004. **76**(16): p. 4833-4838.

23. Gustafsson, M., et al., *Integrated sample preparation and MALDI mass spectrometry on a microfluidic compact disk.* Analytical Chemistry, 2004. **76**(2): p. 345-350.

24. Little, D.P., et al., *MALDI on a chip: Analysis of arrays of low femtomole to subfemtomole quantities of synthetic oligonucleotides and DNA diagnostic products dispensed by a piezoelectric pipet.* Analytical Chemistry, 1997. **69**(22): p. 4540-4546.

25. Ekstrom, S., et al., *Disposable polymeric high-density nanovial arrays for matrix assisted laser desorption/ionization-time of flight-mass spectrometry: II. Biological applications.* Electrophoresis, 2001. **22**(18): p. 3984-3992.

26. Hung, K.C., H. Ding, and B.C. Guo, *Use of poly(tetrafluoroethylene)s as a sample support for the MALDI-TOF analysis of DNA and proteins.* Analytical Chemistry, 1999. **71**(2): p. 518-521.

27. Xiong, S.X., et al., *A new method to improve sensitivity and resolution in matrix-assisted laser desorption/ionization time of flight mass spectrometry.* Proteomics, 2003. **3**(3): p. 265-272.

28. Schuerenbeg, M., et al., *Prestructured MALDI-MS sample supports.* Analytical Chemistry, 2000. **72**(15): p. 3436-3442.

29. Siuzdak, G., *The emergence of mass spectrometry in biochemical research.* Proc. Natl. Acad. Sci., 1994. **91**: p. 11290-11297.

30. Keller, B.O. and L. Li, *Nanoliter solvent extraction combined with microspot MALDI TOF mass spectrometry for the analysis of hydrophobic biomolecules.* Analytical Chemistry, 2001. **73**(13): p. 2929-2936.

31. Jonsson, G., et al., *Plasma Desorption Mass-Spectrometry Studies of Small Proteins Adsorbed to Nitrocellulose.* Journal De Physique, 1989. **50**(C-2): p. 59-61.

32. Fenn, J.B., et al., *Electrospray Ionization for Mass-Spectrometry of Large Biomolecules.* Science, 1989. **246**(4926): p. 64-71.

33. Fenn, J.B., et al., *Electrospray Ionization-Principles and Practice.* Mass Spectrometry Reviews, 1990. **9**(1): p. 37-70.

34. Karas, M. and F. Hillenkamp, *Laser Desorption Ionization of Proteins with Molecular Masses Exceeding 10000 Daltons.* Analytical Chemistry, 1988. **60**(20): p. 2299-2301.

35. Beavis, R.C. and B.T. Chait, *Matrix-assisted laser desorption ionization mass-spectrometry of proteins.* High Resolution Separation and Analysis of Biological Macromolecules, Pt A, 1996. **270**: p. 519-551.

36. Fenselau, C., *MALDI MS and strategies for protein analysis.* Analytical Chemistry, 1997. **69**(21): p. A661-a665.

37. Wei, J., J.M. Buriak, and G. Siuzdak, *Desorption-ionization mass spectrometry on porous silicon.* Nature, 1999. **399**(6733): p. 243-246.

38. http://www.waters.com, *MassPrep DIOS-Target.*

39. Trauger, S.A., et al., *High sensitivity and analyte capture with desorption/ionization mass spectrometry on silylated porous silicon.* Analytical Chemistry, 2004. **76**(15): p. 4484-4489.

40. Becker, H., K. Lowack, and A. Manz, *Planar quartz chips with submicron channels for two-dimensional capillary electrophoresis applications.* Journal of Micromechanics and Microengineering, 1998. **8**(1): p. 24-28.

41. Piruska, A., et al., *The autofluorescence of plastic materials and chips measured under laser irradiation.* Lab on a Chip, 2005. **5**(12): p. 1348-1354.

42. Becker, H. and C. Gartner, *Polymer microfabrication methods for microfluidic analytical applications.* Electrophoresis, 2000. **21**(1): p. 12-26.

43. Becker, H. and L.E. Locascio, *Polymer microfluidic devices.* Talanta, 2002. **56**(2): p. 267-287.

44. Becker, H. and C. Gartner, *Polymer microfabrication technologies for microfluidic systems.* Analytical and Bioanalytical Chemistry, 2008. **390**(1): p. 89-111.

45. PLASKOLITE, I., *Optix® Acrylic Sheet Properties.* 2005.

46. ZeonChemicals, *Typical properties of Zeonor.* 2004. **601ZR10080BP**.

47. Jikun Liu, S.Y., Cheng S. Lee, and Don L. DeVoe, *Polyacrylamide Gel Plugs Enabling 2-D Microfluidic Protein Separations via IEF and Multiplexed SDS Gel Electrophoresis.* Electrophoresis, In press, 2008.

48. Roberts, M.A., et al., *UV Laser Machined Polymer Substrates for the Development of Microdiagnostic Systems.* Anal. Chem., 1997. **69**(11): p. 2035-2042.

49. Martynova, L., et al., *Fabrication of Plastic Microfluid Channels by Imprinting Methods.* Anal. Chem., 1997. **69**(23): p. 4783-4789.

50. Xu, J., et al., *Room-Temperature Imprinting Method for Plastic Microchannel Fabrication.* Anal. Chem., 2000. **72**(8): p. 1930-1933.

51. McCormick, R.M., et al., *Microchannel Electrophoretic Separations of DNA in Injection-Molded Plastic Substrates.* Anal. Chem., 1997. **69**(14): p. 2626-2630.

52. Chou, S.Y., P.R. Krauss, and P.J. Renstrom, *Imprint of Sub-25 Nm Vias and Trenches in Polymers.* Applied Physics Letters, 1995. **67**(21): p. 3114-3116.

53. Abgrall, P., L.N. Low, and N.T. Nguyen, *Fabrication of planar nanofluidic channels in a thermoplastic by hot-embossing and thermal bonding.* Lab on a Chip, 2007. **7**(4): p. 520-522.

54. Sassi, A.P., et al., *Rapid, parallel separations of D1S80 alleles in a plastic microchannel chip.* Journal of Chromatography A, 2000. **894**(1-2): p. 203-217.

55. Mair, D.A., et al., *Injection molded microfluidic chips featuring integrated interconnects.* Lab on a Chip, 2006. **6**(10): p. 1346-1354.

56. http://www.battenfeld-imt.com, *Battenfeld Microsystem*.

57. Kricka, L.J., et al., *Fabrication of plastic microchips by hot embossing.* Lab on a Chip, 2002. **2**: p. 1-4.

58. Klank, H., J.P. Kutter, and O. Geschke, *CO2-Laser Micromachining and Back-end Processing for Rapid Production of PMMA-based Microfluidic Systems.* Lab on a Chip, 2002. **2**: p. 242-246.

59. Brown, L., et al., *Fabrication and characterization of poly(methylmethacrylate) microfluidic devices bonded using surface modifications and solvents.* Lab on a Chip, 2006. **6**: p. 66-73.

60. Sun, Y., Y.C. Kwok, and N.-T. Nguyen, *Low-pressure, high-temperature thermal bonding of polymeric microfluidic devices and their applications for electrophoretic separation.* J. Micromech. Microeng., 2006. **16**: p. 1681-1688.

61. Kelly, R.T. and A.T. Woolley, *Thermal Bonding of Polymeric Capillary Electrophoresis Microdevices in Water.* Anal. Chem., 2003. **75**(8): p. 1941-1945.

62. Lago, C.L.d., et al., *A dry process for production of microfluidic devices based on the lamination of laser-printed polyester films.* Anal. Chem., 2003. **75**(15): p. 3853-3858.

63. Lin, C.-H., et al. *Low Azeotropic Solvent Sealing of PMMA Microfluidic Devices.* in *Proc. 13th Int. Conf. Solid-State Sensors, Actuators, and Microsystems (Transducers 05)*. 2005. Seoul, Korea.

64. Truckenmuller, R., et al., *Bonding of polymer microstructures by UV irradiation and subsequent welding at low temperatures.* Microsystem technologies, 2004. **10**: p. 372-374.

65. Wu, S., *Polymer Interface and Adhesion.* 1982, New York: Marcel Dekker.

66. Uyama, Y., K. Kato, and Y. Ikada, *Surface modification of polymers by grafting.* Advances in Polymer Science, 1998. **137**: p. 1-39.

67. Hu, L.G., et al., *Matrix-assisted laser desorption/ionization time-of-flight mass spectrometry with a matrix of carbon nanotubes for the analysis of low-mass compounds in environmental samples.* Environmental Science & Technology, 2005. **39**(21): p. 8442-8447.

68. Kruse, A., et al., *Surface pretreatment of plastics for adhesive bonding* J. of Adhes. Sci. Technol., 1995. **9**: p. 1611-1621.

69. Collaud, M., et al., *Plasma treatment of polymers: the effect of the plasma parameters on the chemical, physical, and morphological states of the*

polymer surface and on the metal-polymer interface. J. of Adhes. Sci. Technol., 1994. **8**: p. 1143-1156.

70.   Shenton, M.J., M.C. Lovell-Hoare, and G.C. Stevens, *Adhesion enhancement of polymer surfaces by atmospheric plasma treatment.* J. Phys. D: Apply. Phys., 2001. **34**: p. 2754-2760.

71.   Lee, G.-B., et al., *On the surface modification of microchannels for capillary electrophoresis chips.* Electrophoresis, 2005. **26**: p. 4616-4624.

72.   Johansson, B.-L., et al., *Characterization of air plasma-treated polymer surfaces by ESCA and contact angle measurements for optimization of surface stability and cell growth.* J. Appl. Polymer Sci., 2002. **86**: p. 2618-2625.

73.   Puntambekar, A., et al. *Effect of surface modification on thermoplastic fusion bonding for 3-D microfluidics.* in *Proc. Micro Total Analysis Systems (microTAS).* 2002. Nara, Japan.

74.   Nikolova, D., et al., *Surface modification of cyclicolefinic copolymers for optimization of the adhesion to metals.* Surf. Interface Anal., 2004. **36**: p. 689-693.

75.   Wei, S., et al., *Photochemically Patterned Poly(methyl methacrylate) Surfaces Used in the Fabrication of Microanalytical Devices.* J. Phys. Chem. B, 2005. **109**: p. 16988-16996.

76.   Kettner, P., et al., *New results on plasma activated bonding of imprinted features for Bio MEMS applications.* J. Phys.: Conf. Series, 2006. **34**: p. 65-71.

77.   Bolon, D.A. and C.O. Kunz, Polymer Eng. Sci., 1972. **22**: p. 109.

78.   Sowell, R.R., et al., J. Vac. Sci. Technol., 1974. **11**: p. 474.

79.   Vig, J.R. and J.W. LeBus, *UV/ozone cleaning of surfaces.* IEEE Trans. Parts, Hybrid and Packaging, 1976. **PHP-12**: p. 365-370.

80.   Vig, J.R., *UV/ozone cleaning of surfaces.* J. Vac. Sci. Technol. A, 1985. **3**(3): p. 1027-1034.

81.   Peeling, J. and D.T. Clark, J. Polym. Sci.: Polym. Chem., 1983. **21**: p. 2047.

82.   Huang, X.H., M.J. Gordon, and R.N. Zare, *Current-monitoring method for measuring the electroosmotic flow-rate in capillary zone electrophoresis.* Anal. Chem., 1988. **60**(17): p. 1837-1838.

83.   Gaudioso, J. and H.G. Craighead, *Characterizing electroosmotic flow in microfluidic devices.* Journal of Chromatography A, 2002. **971**: p. 249-253.

84.   Raghavan, D., et al., *Characterization of Heterogeneous Regions in Polymer Systems Using Tapping Mode and Force Mode Atomic Force Microscopy.* Langmuir, 2000. **16**: p. 9448-9459.

85.   Doherty, E.A.S., et al., *Microchannel wall coatings for protein separations by capillary and chip electrophoresis.* Electrophoresis, 2003. **24**: p. 34-54.

86.   Gilges, M., M.H. Kleemiss, and G. Schomburg, *Capillary zone electrophoresis separations of basic and acidic proteins using poly(vinylalcohol) coatings in fused silica capillaries.* Anal. Chem., 1994. **66**: p. 2038-2046.

87.   Maszara, W.P., et al., *Bonding of silicon wafers for silicon-on-insulator.* J. Appl. Phys., 1988. **64**(10): p. 4943.

88.   Deng, J.P.Y., W. T.; Ranby, B., J. Appl. Polym. Sci., 2001. **80**: p. 1426-1433.

89.   Currie, E.P.N., W.; Cohen, M. A., *Tethered polymer chains: surface chemistry and their impact on colloidal and surface properties.* Adv. Colloid Interface Sci., 2003. **100-102**: p. 205-265.

90.   Shah, J.J., et al., *Surface modification of poly(methyl methacrylate) for improved adsorption of wall coating polymers for microchip electrophoresis.* Electrophoresis, 2006. **27**(19): p. 3788-3796.

91.   Seino, T., et al., *Laser desorption/ionization on porous silicon mass spectrometry for accurately determining the molecular weight distribution of polymers evaluated using a certified polystyrene standard.* Analytical Sciences, 2005. **21**(5): p. 485-490.

92.   Thomas, J.J., et al., *Desorption/ionization on silicon (DIOS): A diverse mass spectrometry platform for protein characterization.* Proceedings of the National Academy of Sciences of the United States of America, 2001. **98**(9): p. 4932-4937.

93.   Prenni, J.E., et al., *Protein characterization using Liquid Chromatography Desorption Ionization on Silicon Mass Spectrometry (LC-DIOS-MS).* Spectroscopy-an International Journal, 2003. **17**(4): p. 693-698.

94.   Hu, L.G., et al., *Preparation of a biochip on porous silicon and application for label-free detection of small molecule-protein interactions.* Rapid Communications in Mass Spectrometry, 2007. **21**(7): p. 1277-1281.

95.   Meng, J.C., G. Siuzdak, and M.G. Finn, *Affinity mass spectrometry from a tailored porous silicon surface.* Chemical Communications, 2004(18): p. 2108-2109.

96.   Go, E.P., et al., *Selective metabolite and peptide capture/mass detection using fluorous affinity tags.* Journal of Proteome Research, 2007. **6**(4): p. 1492-1499.

97.   Thomas, J.J., et al., *Desorption-ionization on silicon mass spectrometry: an application in forensics.* Analytica Chimica Acta, 2001. **442**(2): p. 183-190.

98.   Lewis, W.G., et al., *Desorption/ionization on silicon (DIOS) mass spectrometry: background and applications.* International Journal of Mass Spectrometry, 2003. **226**(1): p. 107-116.

99.   Peterson, D.S., *Matrix-free methods for laser desorption/ionization mass spectrometry.* Mass Spectrometry Reviews, 2007. **26**(1): p. 19-34.

100.   Shen, Z.X., et al., *Porous silicon as a versatile platform for laser desorption/ionization mass spectrometry.* Analytical Chemistry, 2001. **73**(3): p. 612-619.

101.   Bisi, O., S. Ossicini, and L. Pavesi, *Porous silicon: a quantum sponge structure for silicon based optoelectronics.* Surface Science Reports, 2000. **38**(1-3): p. 1-126.

102.   Nayak, R. and D.R. Knapp, *Effects of thin-film structural parameters on laser desorption/ionization from porous alumina.* Analytical Chemistry, 2007. **79**(13): p. 4950-4956.

103.   Li, X. and P.W. Bohn, *Metal-assisted chemical etching in HF/H2O2 produces porous silicon.* Applied Physics Letters, 2000. **77**(16): p. 2572-2574.

104. Kruse, R.A., et al., *Experimental factors controlling analyte ion generation in laser desorption/ionization mass spectrometry on porous silicon.* Analytical Chemistry, 2001. **73**(15): p. 3639-3645.

105. Lehmann, V. and U. Gosele, *Porous Silicon Formation - a Quantum Wire Effect.* Applied Physics Letters, 1991. **58**(8): p. 856-858.

106. Cassie, A.B.D. and S. Baxter, **Wettability of porous surfaces.** Trans. Faraday Soc. , 1944. **40**: p. 546-551.

107. DuPontFluoroproducts, *DuPont™ Teflon® AF: Processing and Use* 2006. **H-44015-6**.

108. Kruse, R., et al., *Experimental factors controlling analyte ion generation in laser desorption/ionization mass spectrometry on porous silicon.* Anal. Chem., 2001. **73**: p. 3639-3645.

109. Krupenkin, T., et al., *Electrically tunable superhydrophobic nanostructured surfaces.* Bell Labs Technical Journal, 2005. **10**(3): p. 161-170.

110. Krupenkin, T.N., et al., *From rolling ball to complete wetting: The dynamic tuning of liquids on nanostructured surfaces.* Langmuir, 2004. **20**(10): p. 3824-3827.

111. Krupenkin, T.N., et al., *Reversible wetting-dewetting transitions on electrically tunable superhydrophobic nanostructured surfaces.* Langmuir, 2007. **23**(18): p. 9128-9133.

112. Wenzel, R.N., *Resistance of solid surfaces to wetting by water.* Ind. Eng. Chem., 1936. **28**: p. 988-994.

113. Bormashenko, E., et al., *Cassie-Wenzel Wetting Transition in Vibrating Drops Deposited on Rough Surfaces: Is the Dynamic Cassie-Wenzel Wetting Transition a 2D or 1D Affair?* Langmuir, 2007. **23**: p. 6501-6503.

114. Go, E.P., et al., *Desorption/ionization on silicon nanowires.* Analytical Chemistry, 2005. **77**(6): p. 1641-1646.

115. Lafuma, A. and D. Quere, *Superhydrophobic states.* Nature Materials, 2003. **2**: p. 457-460.

116. Wang, Z.H., et al., *A label-free protein microfluidic array for parallel immunoassays.* Electrophoresis, 2006. **27**(20): p. 4078-4085.

117. Wang, J., et al., *Integrated Microfluidics for Parallel Screening of an In Situ Click Chemistry Library.* Angewandte Chemie International Edition, 2006. **45**(32): p. 5276-5281.

118. Su, J., et al., *Combining microfluidic networks and peptide arrays for multi-enzyme assays.* J. Am. Chem. Soc., 2005. **127**: p. 7280-7281.

119. Chen, X., et al., *A Prototype Two-Dimensional Capillary Electrophoresis System Fabricated in Poly(dimethylsiloxane).* Anal. Chem., 2002. **74**(8): p. 1772-1778.

120. Shen, Z., et al., *Parallel analysis of biomolecules on a microfabricated capillary array chip.* Electrophoresis, 2006. **27**(5-6): p. 1084-1092.

121. Li, Y., et al., *Integration of isoelectric focusing with parallel sodium dodecyl sulfate gel electrophoresis for multidimensional protein separations in a plastic microfludic network.* Anal. Chem., 2004. **76**(3): p. 742-748.

122. Medintz, I.L., B.M. Paegel, and R.A. Mathies, *Microfabricated capillary array electrophoresis DNA analysis systems.* Journal of Chromatography A, 2001. **924**(1-2): p. 265-270.

123. Buch, J.S., et al., *Denaturing gradient-based two-dimensional gene mutation scanning in a polymer microfluidic network.* Lab on a Chip, 2005. **5**(4): p. 392-400.

124. Cui, H., et al., *Multistage Isoelectric Focusing in Polymeric Microchips.* Anal. Chem., 2005. **77**: p. 7878-7886.

125. Tang, K.Q., et al., *Generation of multiple electrosprays using microfabricated emitter arrays for improved mass spectrometric sensitivity.* Analytical Chemistry, 2001. **73**(8): p. 1658-1663.

126. Le Gac, S., et al., *Two-dimensional microfabricated sources for nanoelectrospray.* Journal of Mass Spectrometry, 2003. **38**(12): p. 1259-1264.

127. Foret, F. and J. Preisler, *Liquid phase interfacing and miniaturization in matrix-assisted laser desorption/ionization mass spectrometry.* Proteomics, 2002. **2**(4): p. 360-372.

128. DeVoe, D.L. and C.S. Lee, *Microfluidic technologies for MALDI-MS in proteomics.* Electrophoresis, 2006. **27**(18): p. 3559-3568.

129. Ro, K.W., J. Liu, and D.R. Knapp, *Plastic microchip liquid chromatography-matrix-assisted laser desorption/ionization mass spectrometry using monolithic columns.* J. Chromatography A, 2006. **1111**: p. 40-47.

130. Ericson, C., et al., *An automated noncontact deposition interface for liquid chromatography matrix-assisted laser desorption/ionization mass spectrometry.* Analytical Chemistry, 2003. **75**(10): p. 2309-2315.

131. Lee, H., et al., *Development of a multiplexed microcapillary liquid chromatography system for high-throughput proteome analysis.* Analytical Chemistry, 2002. **74**(17): p. 4353-4360.

132. Liu, C.L. and X.M. Zhang, *Multidimensional capillary array liquid chromatography and matrix-assisted laser desorption/ionization tandem mass spectrometry for high-throughput proteomic analysis.* Journal of Chromatography A, 2007. **1139**(2): p. 191-198.

133. Stachowiak, T.B., et al., *Fabrication of porous polymer monoliths covalently attached to the walls of channels in plastic microdevices.* Electrophoresis, 2003. **24**(21): p. 3689-3693.

134. Nguyen, N.-T. and S.T. Wereley, *Fundamentals and applications of microfluidics.* 2002: Artech house Inc.

135. Tsao, C.W., J. Liu, and D.L. DeVoe, *Droplet Formation from Hydrodynamically-Coupled Microchannels.* Lab on a Chip, 2007. **In Process**.

136. Darcy, H., *Les Fontaines Publiques de la Ville de Dijon.* 1856: p. Dalmont, Paris.

137. Onnerfjord, P., et al., *Homogeneous sample preparation for automated high throughput analysis with matrix-assisted laser desorption/ionisation time-of-flight mass spectrometry.* Rapid Communications in Mass Spectrometry, 1999. **13**(5): p. 315-322.

138. Ro, K.W., H. Liu, and D.R. Knapp, *Plastic microchip liquid chromatography-matrix-assisted laser desorption/ionization mass spectrometry using monolithic columns.* Journal of Chromatography A, 2006. **1111**(1): p. 40-47.

139. Liu, J., et al., *Monolithic column plastic microfluidic device for peptide analysis using electrospray from a channel opening on the edge of the device.* International Journal of Mass Spectrometry, 2007. **259**(1-3): p. 65-72.